

Dissertation
submitted to the
Combined Faculties of the Natural Sciences and Mathematics
of the Ruperto-Carola University of Heidelberg, Germany
for the degree of
Doctor of Natural Sciences

Put forward by
Dipl. Phys. Torsten Mandel
born in Viernheim

Oral examination: 14th of May 2014

Quantum manipulation of (ultra-)cold atom systems for information processing

Referees: Prof. Dr. Jian-Wei Pan
Prof. Dr. Selim Jochim

Abstract

This work is split into two parts, in part one of this thesis we report on the improvement of the lifetime of a quantum memory based on neutral atoms while in part two we will focus on a new setup to perform experiments on neutral atoms within a 2D optical lattice. In the quantum memory experiment we used a blue-detuned optical dipole trap to confine the atoms in a minimum intensity region of the light beam, reducing dephasing due to differential light shift. We saw improvement in comparison to a previous experiment using red-detuned dipole traps. The anticipated lifetime could not be reached, however. We observed oscillations of the retrievability of our stored state which we explain by the evolution of the transversal component of the spinwave using Monte-Carlo simulations. In the second part we report on our new setup, built to investigate a broad range of experiments regarding 2D physics on optical lattices. This field is of special interest as it allows to simulate Hamiltonians of a wide range e.g. from solid state physics and opens possibilities regarding large-scale entanglement/one-way computing. In particular we discuss 2D Mott-insulators, 2D-Bloch oscillation induced transport phenomena and ring-exchange in a superlattice plaquette.

Zusammenfassung

Diese Arbeit besteht aus 2 Teilen, wobei wir im ersten Teil von einer verbesserten Speicherzeit in einem auf neutralen Atomen basierten Quantenspeicher berichten, während wir uns im zweiten Teil auf einen neuen Aufbau für Experimente mit neutralen Atomen in 2D optischen Gittern konzentrieren. Um die Speicherdauer der Spinwelle zu erhöhen benutzten wir eine blau verstimmte Dipolfalle, die die neutralen Atome im Minimum der Laserintensität gefangen hält und so die Dekohärenz durch den "differential lighshift" minimiert. In der Tat beobachten wir eine Verbesserung gegenüber einem vorhergehenden Experiment, das eine rot verstimmte optische Dipolfalle nutzte. Die erwartete Lebensdauer konnte jedoch leider nicht erreicht werden. Die dabei auftretende zeitliche Oszillation der Ausleseeffizienz konnte durch eine Monte-Carlo Simulation der Transversalkomponente der Spinwelle erklärt werden. Im zweiten Teil berichten wir über unseren neuen Experimentaufbau, der darauf ausgelegt ist ein breites Spektrum an Experimenten auf einem zweidimensionalen optischen Gitter durchführen zu können. Dieses Feld ist besonders interessant, da es erlaubt Hamiltonians aus einem breiten Spektrum zu simulieren, z.B. aus der Festkörperphysik und eröffnet Möglichkeiten für großskalierte Verschränkung und One-way Quantum Computing. Insbesondere konzentrieren wir uns auf den 2D-Mott Isolator, Transportphänomene induziert durch 2D-Bloch Oszillationen und den Ringaustausch in einer Supergitter-Plakette.

Contents

I. Transversal mode revival in a quantum memory of neutral atoms in a blue detuned dipole trap.	1
1. Introduction	2
2. Quantum memory theory	4
2.1. Motivation and DLCZ scheme	4
2.2. Light-ensemble interaction	5
2.2.1. writing	5
2.2.2. reading	7
2.3. $g^{(2)}$ -second order cross correlation function	8
3. Experimental setup and expected memory stability	10
3.1. MOT	10
3.2. The Dipole Trap	12
3.3. Complete setup	15
3.4. Dephasing mechanisms	15
4. Experiment	20
4.1. Procedures and lifetime observations	20
4.2. Transversal mode revival of the quantum memory spinwave	23
II. Experiments on a 2D optical lattice towards atom entanglement.	27
5. Motivation and theoretical backgrounds for experiments regarding 3D/2D ultracold atoms and optical lattices	28
5.1. Bose-Einstein condensation	28
5.2. The BKT-transition	31
5.3. Optical lattices	33
6. Our new setup	39
6.1. General design	39
6.2. Time sequence from MOT to BEC	41
6.3. Magnetic Transfer	42

6.4. Lasers	45
6.5. High resolution Imaging	48
6.5.1. Design with simulated abberations and compensations	48
6.5.2. Alignment procedure and performance	54
6.6. Experiment preparation	56
6.7. Mott Insulator transition	63
7. Transport on a lattice due to 2D Bloch oscillations	67
7.1. Motivation and theory	67
7.2. Magnetic fields and electro/magnetic stability	70
7.2.1. Side coils	70
7.2.2. Magnetic field stability and effects	73
7.3. Experiment	75
7.3.1. Preparation	75
7.3.2. First test in 2D, observation of 1D Bloch Oscillations	75
7.3.3. Revisiting the 2D case	80
8. Ring exchange Experiment	86
8.1. Theory	86
8.1.1. RVB states	86
8.1.2. Laughlin state	88
8.1.3. Ring exchange	88
8.2. Magnetic field stabilization	90
8.3. Gradient coils	95
8.3.1. Side coils revisited	95
8.3.2. MOSFET switch to change between one and two layered trap coil	98
9. Conclusion and outlook	102
A. AdWin two channel adder and lowpass filter	103
B. N170-1 current controller	104
C. New high resolution system mount	105
D. N368-E,F,G,N: FM, FO-locks and PID cards	107
E. Side-coils holding frame	114
F. Acknowledgements	122
Bibliography	124

Part I.

Transversal mode revival in a quantum memory of neutral atoms in a blue detuned dipole trap.

1. Introduction

Quantum information, computation and simulation are of great interest as they can exploit several quantum mechanical concepts which allow applications that are not possible using classical resources. Of great interest, but not limited to, are quantum key distribution [7, 21], quantum computation with its famous Shor[68] and Grover[29] algorithms and quantum simulations. Key concepts for quantum information include superposition and entanglement. Where a classical computer or classical digital channel only uses 0 and 1 as the logical states to process/transmit data, in quantum information science we can make use of any two-state system e.g. horizontal/vertical polarization of photons to create a superposition state of 0 and 1. This so called Qubit can take on any form of $\alpha|0\rangle + \beta|1\rangle$ with $\alpha^2 + \beta^2 = 1$, $\alpha, \beta \in \mathbb{C}$. As α and β are complex numbers one might assume that we could store infinite amounts of information already into one qubit by mapping a bijective association between small changes of the complex vector and arbitrary datasets. This however is not feasible, as upon measurement the quantum state will always be projected upon either $|0\rangle$ or $|1\rangle$ where α^2 and β^2 represent only the possibilities for either outcome. During computations however we can make full use of the large Hilbert space spanned by multiple Qubits in superposition. The Grover algorithm can be understood as a searching algorithm which operates on all possible inputs at the same time[29, 59]. The trick in quantum computation is mainly to find algorithms that map unto well defined states upon measurement, e.g. the Grover search maximizes the probability to measure the searched output state. The second key ingredient, entanglement is an important resource for e.g. quantum key distribution and in one-way quantum computing.

A typical setup could include two photons created by spontaneous parametric down conversion (SPDC) for quantum key distribution (e.g. for [21]): when obtained from the right position in such a setup, it is not possible to tell which one of the two photons was vertical or horizontal polarized and the state of the system can be written as: $|00\rangle + |11\rangle$. Even if we separate those two photons from each other we can immediately know the state of the other once we measure the state of one of them. This was cause for a long debate about if there were some hidden variables in quantum mechanics and the formulation of the EPR paradox in 1935 [20]. Only much later, in 1964, Bell suggested on how to test for hidden variables by the now famous Bell-inequality [6]. It was however only much later again until recent thorough tests showed indeed the violation of Bell's inequality which forces rejection of localism or realism. Those tests often included loopholes until a recent experiment which closes in principle all main loopholes using photons[25]. To avoid digressing too far we can summarize that with such an entangled state one already has a powerful resource which enables quantum

key distribution whereas more complicated cluster-states of high entanglement would be interesting for one-way computing[64].

In our application we research a quantum memory based on neutral atoms which is a key ingredient for long-range quantum key distribution. Quantum memories are required for the quantum repeater nodes which swap and purify entanglement along the communication line. Without quantum repeater nodes the maximally reachable distance of quantum key distribution is limited to roughly 200km. Finally we would like to mention the fields of quantum simulation and entanglement; both open up interesting possibilities. Using e.g. neutral atoms on optical lattices to simulate a Hamiltonian one often has in comparison to solid state physics much more control and accessibility to the system parameters. For example Bloch Oscillations[8] are hard to observe directly, in solid state physics they are observable indirectly via THz radiation [13], and normally suffer from fast decay due to imperfections in normal crystals whereas in an optical lattice the involved timescales are much slower and their effects can be seen directly and the systems are tunable[33, 54]. Further applications in optical lattices would be large-scale entanglement using plaquettes in super-lattices. We discuss an experiment suggested by Paredes and Bloch [61] which should produce a four-particle GHZ state. We outline the experimental requirements to the setup and present the steps which have been undertaken so far to reach this goal. Entanglement on even larger scale would open up the possibility of one-way quantum computing on optical lattices using neutral atoms. Now what we have to keep in mind is that we are talking here about quantum systems and as such they are all vulnerable to undesired interactions with the environment or even just their own constituents, generally leading to dephasing. In the first part of this work we will focus on a quantum memory based on neutral atoms trapped in a blue detuned optical trap and explore the various dephasing mechanisms present. In the second part we present our new setup for 2D quantum simulations and the various experiments which were/are open to perform on it.

2. Quantum memory theory

2.1. Motivation and DLCZ scheme

Quantum memories are a key ingredient if one wants to implement a long range quantum key distribution. Quantum key distribution provides the possibility to securely exchange one-time pads for a Vernam cipher[76]. If implemented correctly any attempt to eavesdrop on the key exchange should be detectable above a set security threshold. For long distances however arises the problem that the resources, in general single photons, decohere and the quantum key distribution (qkd) fails. We decided to implement a quantum memory which could be used in a Duan-Lukin-Cirac-Zoller (DLCZ) based quantum repeater [16] using neutral atoms in a blue detuned optical trap. To understand these decisions we will start out with a description of the DLCZ scheme and explain the further necessary steps to realize a long-lifetime quantum memory. Basically the quantum repeater links adjacent elements by entanglement to finally create an entangled channel between its two ends, we can explain this by looking at one such element: Two individual atomic ensembles possessing a Λ -structure¹ are being shone on with a “write”-laser/photon and the output Stokes-photon(s) are being overlapped on a beamsplitter. If one measures only one photon from the beamsplitter coincidence the ensembles have been successfully entangled as it is not possible to tell which ensemble was transferred to the excited state:

$$|\psi\rangle = \frac{1}{\sqrt{2}} \left(|S_1 G_2\rangle + e^{i\phi} |G_1 S_2\rangle \right) \quad (2.1)$$

where G and S are the collective groundstates of the ensembles e.g. we can write S as:

$$|S\rangle = \frac{1}{\sqrt{N}} \sum_{i=1}^N e^{i\phi_i} |g_1 \dots s_i \dots g_N\rangle \quad (2.2)$$

By linking multiple elements together we can swap on entanglement down such a repeater chain to the desired target. But as entanglement will not always succeed the individual photons might have to be stored for longer times in the respective ensembles.

¹See fig. 2.1

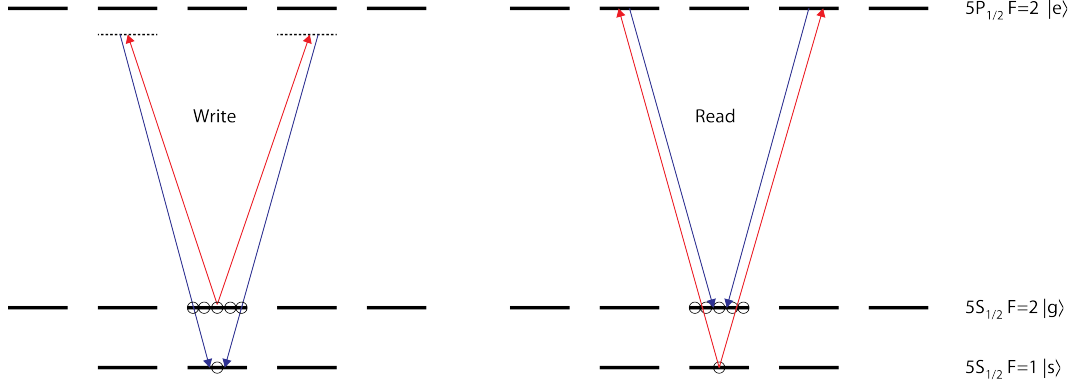


Figure 2.1.: The Lambda structure which we used for our experiment: the magnetically insensitive $|g\rangle = |5^2S_{1/2}F=2\rangle$ and $|s\rangle = |5^2S_{1/2}F=1\rangle$ of ^{87}Rb are being used as the memory states with $|e\rangle = |5^2P_{1/2}F=2\rangle$ being the immediate state for the raman transfer.

2.2. Light-ensemble interaction

2.2.1. writing

In this section we represent a brief summary of the light-ensemble interaction as in [53, 58, 51] which in terms are based mainly on [82, 16]. To excite an atom of an ensemble in the $|G\rangle$ state we shine on an off-resonant write pulse to the atom cloud:

$$E_W(\mathbf{r}, t) = \epsilon_W E_W(\mathbf{r}, t) e^{i\mathbf{k}_W \mathbf{r} - i\omega_W t} + H.c. \quad (2.3)$$

with ϵ_W being the polarization vector and ω_W the write light frequency with according \mathbf{k}_W vector. A successful write operation will lead to emittance of an Anti-stokes photon of frequency $\omega_{AS} = \Delta E_{AS}/\hbar + \Delta_W$ [58] and couple the $|e\rangle$ and $|s\rangle$ state by:

$$\mathbf{E}_{AS}(\mathbf{r}, t) = \sum_{\mathbf{k}} \epsilon_{\mathbf{k}} E_{\mathbf{k}} \hat{a}_{\mathbf{k}} e^{i\mathbf{k}_{AS} \cdot \mathbf{r} - i\omega_{AS} t} + H.c. \quad (2.4)$$

with $\epsilon_{\mathbf{k}} = \sqrt{\frac{\hbar\omega_{\mathbf{k}}}{2\epsilon_0 V}}$ being the normalization factor whereof V is the quantization volume, furthermore $\hat{a}_{\mathbf{k}}$ being the annihilation operator of mode \mathbf{k} . We can give the full hamiltonian by assuming fixed atom positions during the interaction² in the rotating wave approximation by:

$$H = \sum_i^N \left[\hbar\Delta\sigma_{ee}^i + \left(-\hbar\Omega_W(\mathbf{r}_i, t) e^{i\mathbf{k}_W \cdot \mathbf{r}_i} \sigma_{eg}^i + \sum_{\mathbf{k}} \hbar g_{\mathbf{k}} a_{\mathbf{k}} e^{i\mathbf{k} \cdot \mathbf{r}_i - i\Delta\omega_{\mathbf{k}} t} \sigma_{es}^i + h.c. \right) \right] \quad (2.5)$$

²Which is valid because we deal with short pulses and very cold atoms.

with $\Delta = \omega_{eg} - \omega_W$ and $\Delta\omega_{\mathbf{k}} = \omega_{\mathbf{k}} - \omega_W - \omega_{sg}$ being the detunings, $\omega_{eg} = \omega_e - \omega_g$ and $\omega_{sg} = \omega_s - \omega_g$ the transition frequencies between the ground states and the excited state, $\sigma_{lm}^i = |l\rangle_i \langle m|_i$, ($l, m = e, g, s$) the corresponding transition operators, $\Omega_W(\mathbf{r}, t) = \mathbf{d}_{eg} \cdot \hat{\mathbf{e}}_W E_W(\mathbf{r}, t)/\hbar$ the Rabi-frequency of the write light and $g_{\mathbf{k}} = -\mathbf{d}_{es} \cdot \hat{\mathbf{e}}_{\mathbf{k}} \varepsilon_{\mathbf{k}}/\hbar$ being the coupling coefficients of each mode of the Stokes light[53, 82]. By adiabatic elimination of the excited state and neglecting AC-Stark shift due to the write light we can simplify this Hamiltonian to:

$$H = \sum_i^N \left(\sigma_{sg}^i \frac{\Omega_W(\mathbf{r}, t) e^{i\mathbf{k}_W \cdot \mathbf{r}_i}}{\Delta} \sum_{\mathbf{k}} \hbar g_{\mathbf{k}} a_{\mathbf{k}}^\dagger e^{-(i\mathbf{k} \cdot \mathbf{r}_i - i\Delta\omega_{\mathbf{k}} t)} + H.c. \right) \quad (2.6)$$

which describes the spontaneous emission of N atoms when decaying from the $|s\rangle$ to $|g\rangle$ state. The linewidth is given by $\Gamma' = \frac{\Omega_W^2}{\Delta^2} \Gamma$ with Γ being the decay rate from $|e\rangle$ to $|s\rangle$. After $\frac{1}{\Gamma'}$ the Stokes-light will no longer be emitted isotropically but enter the superradiance regime. To stay in the spontaneous emission regime we have to keep our pulse time T shorter than Γ' which will allow to solve the Schrödinger equation in 1st order perturbation theory:

$$|\psi\rangle = \left(1 - i \int_0^T H(\tau) d\tau \right) |vac\rangle + o(p) \quad (2.7)$$

where $|vac\rangle = |0\rangle_a |0\rangle_p$ with $|0\rangle_a = \otimes_i |g\rangle_i$ denoting the atomic and $|0\rangle_p$ denoting the light vacuum state. This integrates to:

$$|\psi\rangle = |0\rangle_a |0\rangle_p + \sum_i^N \frac{\Omega_W(\mathbf{r}_i) e^{i\mathbf{k}_W \cdot \mathbf{r}_i}}{\Delta} |g \dots s_i \dots g\rangle |\gamma\rangle_i \quad (2.8)$$

where

$$|\gamma\rangle_i = -i \int_0^T \sum_{\mathbf{k}} g_{\mathbf{k}} a_{\mathbf{k}}^\dagger e^{-(i\mathbf{k} \cdot \mathbf{r}_i - i\Delta\omega_{\mathbf{k}} t)} |0\rangle_p \quad (2.9)$$

is the spontaneous emitted Stokes-light of the i th atom under the assumption that the Rabi frequency is time independent. Under the paraxial approximation one can, as long as the detection angle is small compared to the diffraction angles, defined by the ensemble waist and length[82], neglect the phase factors arising from the different positions of the individual atoms. This simplifies eq. (2.9) to a single mode:

$$|\gamma\rangle_i = \sqrt{p} a_S^\dagger e^{i\mathbf{k}_S \cdot \mathbf{r}_i} |0\rangle_p \quad (2.10)$$

with a_S^\dagger being the single mode creation operator and $p = \Gamma T \frac{\Omega_W^2}{\Delta^2} d\Omega$ being the chance to scatter the Stokes photon into the detection angle $d\Omega$ which modifies eq. (2.8) to:

$$|\psi\rangle = \left[1 + \sqrt{p} \left(\sum_i^N e^{i\Delta\mathbf{k} \cdot \mathbf{r}_i} \sigma_{sg}^i \right) a_S^\dagger \right] |vac\rangle \quad (2.11)$$

where $\Delta \mathbf{k} = \mathbf{k}_W - \mathbf{k}_S$ is the difference of the \mathbf{k} -vector of the write light and its associated Stokes photon. Furthermore we assume that we have a constant Rabi-frequency over the atomic ensemble. By defining a collective state operator S ,

$$S^\dagger = \frac{1}{\sqrt{N}} \sum_i^N e^{i\Delta \mathbf{k} \cdot \mathbf{r}_i} \sigma_{sg}^i \quad (2.12)$$

obeying $[S, S^\dagger] \simeq 1$, we can write

$$|\psi\rangle = \left(1 + \sqrt{\chi} S^\dagger a_S^\dagger\right) |vac\rangle \quad (2.13)$$

where $\chi = Np$ is the probability to detect one Stokes photon during one write process. If such a photon is being detected a spinwave is imprinted unto the atomic ensemble and the ensemble is being transferred from the collective ground state to the collective excited state as already depicted by eq. (2.2). To obtain a single spatial mode for storage in the ensemble it is important to have a low Fresnel number:

$$F = \frac{A}{\lambda L} \quad (2.14)$$

where $A = \pi^2 \omega^2$ with ω being the waist of the atomic ensemble. If the diffraction angle in axial and longitudinal direction of the ensemble are being assumed to be the same one can approximate $d\Omega \approx \lambda^2/A$ which yields a total excitation probability $\chi = Np = N\Gamma T \frac{\Omega_W^2 \lambda^2}{\Delta_W^2 A} \sim d_0 \gamma_S T$ with $d_0 \sim N\sigma_0/A$ being the optical depth, $\sigma_0 = \frac{\lambda^2}{2\pi}$ the scattering cross section and $\gamma_S \sim \Gamma \frac{\Omega_W^2}{\Delta_W^2}$. To finally achieve spontaneous Raman scattering it is sufficient to keep the excitation probability $\chi \ll 1$ by using weak laser beams.

2.2.2. reading

We now follow with the reading mechanism of the quantum memory, as the previous subsection we follow the descriptions given by [53, 58, 51] which in terms are based mainly on [82, 16]. To convert the stored spinwave back to a photon it is sufficient to couple a strong read laser pulse to the transition $|s\rangle \rightarrow |e\rangle$ which will yield a Stokes photon. Unlike the write process the atoms will collectively interfere and if the Anti-Stokes field is mode-matched with the detection mode one can retrieve the photon with high efficiency. Besides exchanging indices from (W)rite to (R)ead with according frequency changes we end up with the same description for the light as in eq. (2.3). The decay of the $|S\rangle \rightarrow |G\rangle$ state can be expanded as:

$$|S\rangle \rightarrow \otimes_i |g\rangle_i E(\mathbf{r}') \quad (2.15)$$

where the Stokes field at position \mathbf{r}' is given by:

$$E(\mathbf{r}') = \frac{1}{\sqrt{N}} \sum_i^N e^{i\Delta \mathbf{k} \cdot \mathbf{r}_i + i\mathbf{k}_R \cdot \mathbf{r}_i} \frac{\varepsilon_0}{\Delta r'_i} e^{i\mathbf{k}_S \Delta r'_i} \quad (2.16)$$

with $\Delta r'_i = |\mathbf{r}' - \mathbf{r}_i|$ where \mathbf{r}_i are the positions of the individual atoms. Assuming again the paraxial approximation and mode matching ($\mathbf{k}_W - \mathbf{k}_{AS} + \mathbf{k}_R - \mathbf{k}_S = 0$) we can observe constructive interference on the detection surface and the anti-Stokes field will be:

$$E(\mathbf{r}') = \frac{1}{\sqrt{N}} \sum_i^N \frac{\varepsilon_0}{|z' - z_i|} \exp \left[i\mathbf{k}_S \left(|z'| + \frac{x_i^2 + y_i^2}{2|z' - z_i|} + \frac{x'^2 + y'^2}{2|z' - z_i|} \right) - i\mathbf{k}_S \frac{x_i x' + y_i y'}{|z - z_i|} \right] \quad (2.17)$$

$$\simeq \sqrt{N} \int d\mathbf{r}'' n(\mathbf{r}'') \frac{\varepsilon_0}{z'} \exp \left[-i\mathbf{k}_S \left(z' + \frac{x'^2 + y'^2}{2z'} \right) \right] = \sqrt{N} \zeta_S(\mathbf{r}') \quad (2.18)$$

here $\zeta_S(\mathbf{r}') = \frac{\varepsilon_0}{z'} \exp[-i\mathbf{k}_S(z' + \frac{x'^2 + y'^2}{2z'})]$, $n(\mathbf{r})$ is the density distribution and we assumed a small detection angle. This, combined with the imprinted transversal mode (which is also gaussian for our case) will play a role later on for the transversal mode revival which we observed when studying our memory coherence time. Finally we give the retrieve efficiency η_{ret} by:

$$\eta_{ret} = \frac{\gamma N d\Omega}{\gamma N d\Omega + \gamma} = \frac{N d\Omega}{N d\Omega + 1} \quad (2.19)$$

where γ is the decay rate of the excited state and $\gamma N d\Omega$ gives us the probability to scatter a photon into the detection mode. Following the already assumed $d\Omega \sim \frac{\lambda^2}{A}$ one can show that $\eta_{ret} \sim 1 - 1/d_0$ - with the error of retrieval scaling by $1/\sqrt{d_0}$, taking into account the narrow EIT window. EIT will also ensure that the photon will not be absorbed by the atoms during the read process while requiring a long enough read pulse to permit the slower Stokes photon to leave the ensemble. The combined state is thus:

$$|\psi\rangle = (1 + \sqrt{\chi} a_S^\dagger a_{AS}^\dagger) |vac\rangle \quad (2.20)$$

which means that if we detect an Anti-Stokes photon (probability χ) then we will definitely get a Stokes-photon as well which is a nonclassical correlation.

2.3. $g^{(2)}$ -second order cross correlation function

This brief section is also based on [53, 58, 51, 82, 16] and considers higher orders of excitation in the atomic ensemble e.g. two Anti-Stokes photon have a possibility of χ^2 to occur during one measurement. We can evaluate the cross correlation function by calculation of a combined Anti-Stokes and Stokes state which is still valid even though they don't exist at the same time. For second order excitation we get:

$$|\psi\rangle = \left(1 + \sqrt{\chi} a_S^\dagger a_{AS}^\dagger + \chi a_S^{\dagger 2} a_{AS}^{\dagger 2} / 2 \right) |vac\rangle \quad (2.21)$$

$$= |0_{AS} 0_S\rangle + \sqrt{\chi} |1_{AS} 1_S\rangle + \chi |2_{AS} 2_S\rangle \quad (2.22)$$

which is a multi-mode Fock state. By comparing the second order cross correlation with its second order self correlation in the Cauchy-Schwarz inequality we can determine if

we deal with classical or nonclassical light.

$$g_{AS,S}^{(2)} = \frac{\langle a_{AS} a_S a_{AS}^\dagger a_S^\dagger \rangle}{\langle a_{AS} a_{AS}^\dagger \rangle \langle a_S a_S^\dagger \rangle} \quad (2.23)$$

$$g_{AS}^{(2)} = \frac{\langle a_{AS}^2 a_{AS}^{\dagger 2} \rangle}{\langle a_{AS} a_{AS}^\dagger \rangle^2} \quad (2.24)$$

$$g_S^{(2)} = \frac{\langle a_S^2 a_S^{\dagger 2} \rangle}{\langle a_S a_S^\dagger \rangle^2} \quad (2.25)$$

$$[g_{AS,S}^{(2)}]^2 \leq g_{AS}^{(2)} g_S^{(2)} \quad (2.26)$$

Whenever the CS-inequality (eq. (2.26)) is violated we deal with nonclassical light. In our case $g_{AS,S}^{(2)} = 1/\chi$ whereas the self-correlation $g_S^2 = g_{AS}^2 = 2$, as already mentioned we will keep the excitation probability $\chi \ll 1$ which will lead to the violation of the Cauchy-Schwarz inequality and nonclassically correlated photons. This type of quantum memory can then also be exploited as a deterministic single photon source.

3. Experimental setup and expected memory stability

3.1. MOT

When we set out to implement our quantum memory we decided upon an atomic ensemble trapped in a blue detuned dipole trap with a compensation beam for the differential light shift. Besides having a long fancy name there are good reasons for those decisions as we will see in section 3.4. One could jump between the individual techniques and their respective decoherence problems, we however choose to first give a summary of the basic techniques which will finally lead us to the aforementioned trapped ensemble and then give an explanation which decoherence mechanisms one has to consider and how we beat them. We will therefore start out with a description of the Dark-MOT (DMOT, also known as dark spontaneous force optical trap[44]) which is used as the starting point to load the hollow beam dipole trap later on. The DMOT is produced in a glass cell from Japan Cell in a vacuum on the order of $5 \cdot 10^{-9}$ mbar when the Rubidium dispenser is switched on[51]. A standard MOT consists of an Anti-Helmholtz coil pair and 6 σ -polarized cooling beams (typically it is sufficient to retroreflect 3 beams and include $\lambda/4$ waveplates to tune the polarization of the reflected beam but we chose the former). The theoretical background for a normal MOT can be found in standard course textbooks[14] and will not be discussed in detail here.

The term Dark-MOT originates by a dark spot in the center of the repumper beam which makes cold atoms at the center stay in the dark $F=1$ state which reduces collisions and radiative trapping, yielding higher densities[58, 44]. Our main laser (Toptica DLX 110) is locked to the D2 $F = 2 \rightarrow F' = 3$ transition¹ using Doppler free saturation spectroscopy[14] by a FM-lock circuit with a detuning of 192MHz from a double pass AOM.

From the main laser we derive in a second double pass AOM cooling light by detuning it by 2×-105 MHz yielding an effective -18 MHz detuning. For repumping we use a second laser (Toptica DL 100) locked to the D2 $F = 1 \rightarrow F' = 1 - 2$ crossover transition. By using an AOM at 78.47MHz we create the $F = 1 \rightarrow F' = 2$ repumping light, which we use once for a normal repumping beam and second for the “dark spot” repumper which is required for the DMOT. The DMOT helps beating the problems of radiation trapping and radiative escape, by removing the repumping light in the center area (where the already cold atoms sit anyway) we can remove the atoms from the cooling cycle (as

¹See fig. 3.1 for transition namings and frequencies.

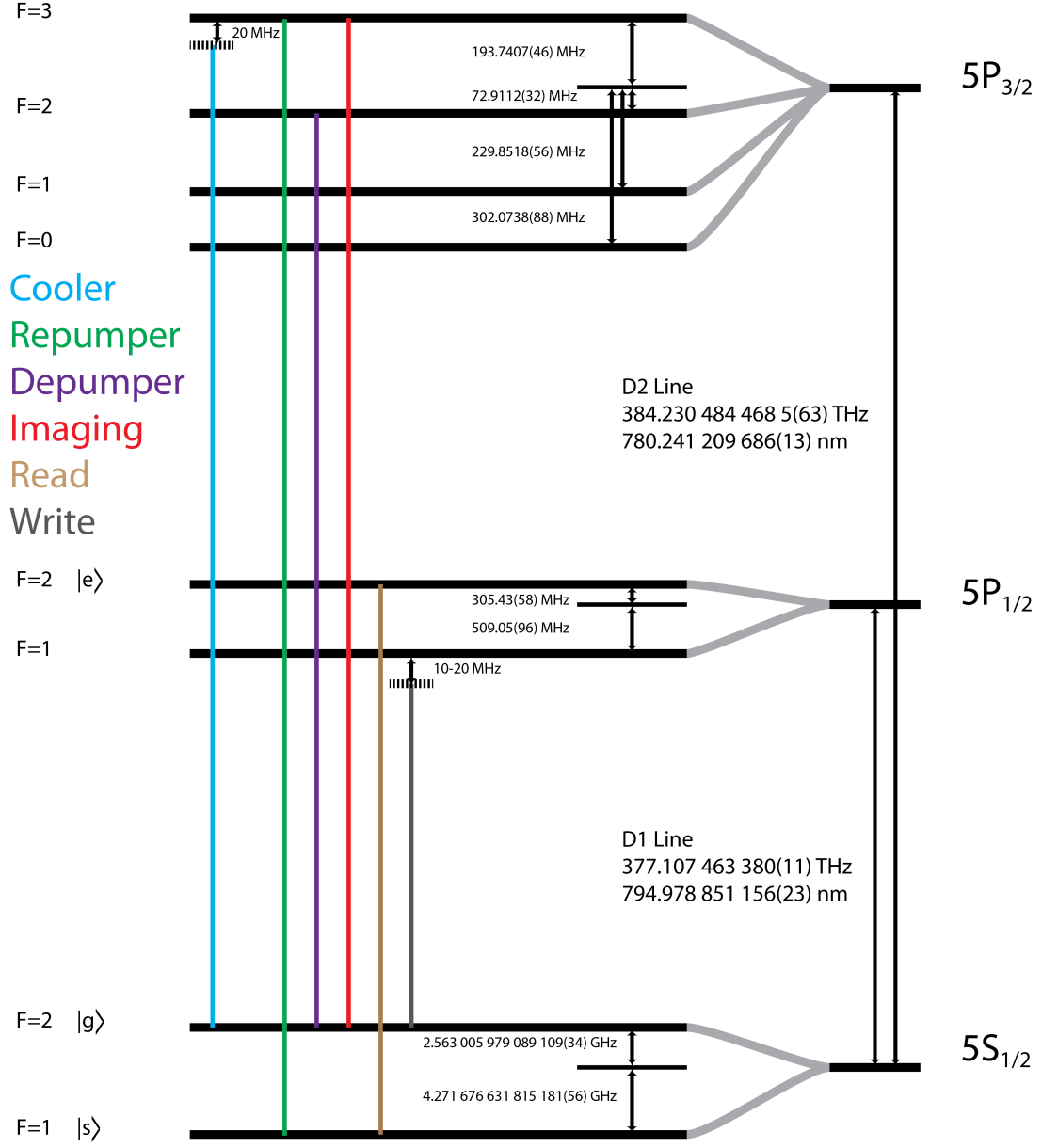


Figure 3.1.: Energy levels of ^{87}Rb and indicators for the transitions used in our experiment, frequency/wavelength data taken from [69].

they will finally fall into the no longer interacting $F = 1$ state). This will finally increase the atom density in the dark center of the trap. The normal repumping beam is used whenever we need to illuminate the whole sample e.g. state preparation. A further method to increase the atomic density was the introduction of a depumping laser which is taken from the cooler laser but set to the $F = 2 \rightarrow F' = 2$ transition.

3.2. The Dipole Trap

By applying a strong laser field one can exploit the AC-stark shift to trap atoms solely in an optical potential[28]:

$$U(r, z) = -\frac{\alpha(\omega)}{2c\epsilon_0}I(r, z) \quad (3.1)$$

where I is the laser intensity and α is the scalar polarizability of the used atoms and can be calculated using[28]:

$$\alpha = -\frac{\pi c^3 \epsilon_0}{2} \left(\frac{2\Gamma_{D1}}{\omega_{D1}\Delta_{D1}} + \frac{2\Gamma_{D2}}{\omega_{D2}\Delta_{D2}} \right) \quad (3.2)$$

where the indices indicate which of the p-transitions we use (D1 and D2 line)². As we can see from eq. (3.2): depending on the sign of the detuning we will either end up with an attractive or a repulsive potential. In a previous experiment of our group [70] a quantum memory using a red detuned dipole trap could achieve a storage time on the order of 1ms. A main limitation there was the differential light shift exerted on the atoms by the red detuned dipole trap. As the differential light shift is directly connected to intensity a blue detuned trap should provide a better lifetime over such a red detuned one as a blue detuned trap actually traps the atoms in the dark zone. We will discuss this deeper in section 3.4.

To actually trap atoms in a dark zone surrounded by light without resorting to 6 individual light sheets it is possible to create a main hollow beam and plug it with two light-sheets which can be generated using cylindrical lenses. As for the hollow beam we decided on a method described in [5]: A normal focal lens and axicon (conical lens) doublet to create a ring beam. Their paper also gives a fast way to approximate the potential around the focus but especially later for decoherence calculations it is better to rely on Kirchhoff-Fresnel diffractive theory. Either way, the systems parameters are fixed by [53]:

$$R_0 = (n - 1)\alpha F \quad (3.3)$$

where we have $R_0 \sim 167\mu m$ as the ring's radius, $n=1.525$ (Zeonex 480R refractive index), $F=25cm$, and $\alpha=0.07276^\circ \pm 5\%$. We can calculate the exact potential using eq. (3.1) and the lens-axicon generated field (for derivation see:[53]):

$$U(r, z) = \frac{2\pi}{\lambda} \frac{\sqrt{\frac{2P}{\pi\omega^2}}}{z} \int_0^{Ap} e^{-i\frac{2\pi}{\lambda} \left(\frac{\rho^2}{2} (1/q(z)+1/z-1/f) - \frac{R\rho}{f} \right)} B_J \left(0, \frac{2\pi}{\lambda} r\rho z \right) \rho d\rho \quad (3.4)$$

²We also once included higher order polarizability in order to study decoherence effects which we observed, but they proved to be negligible

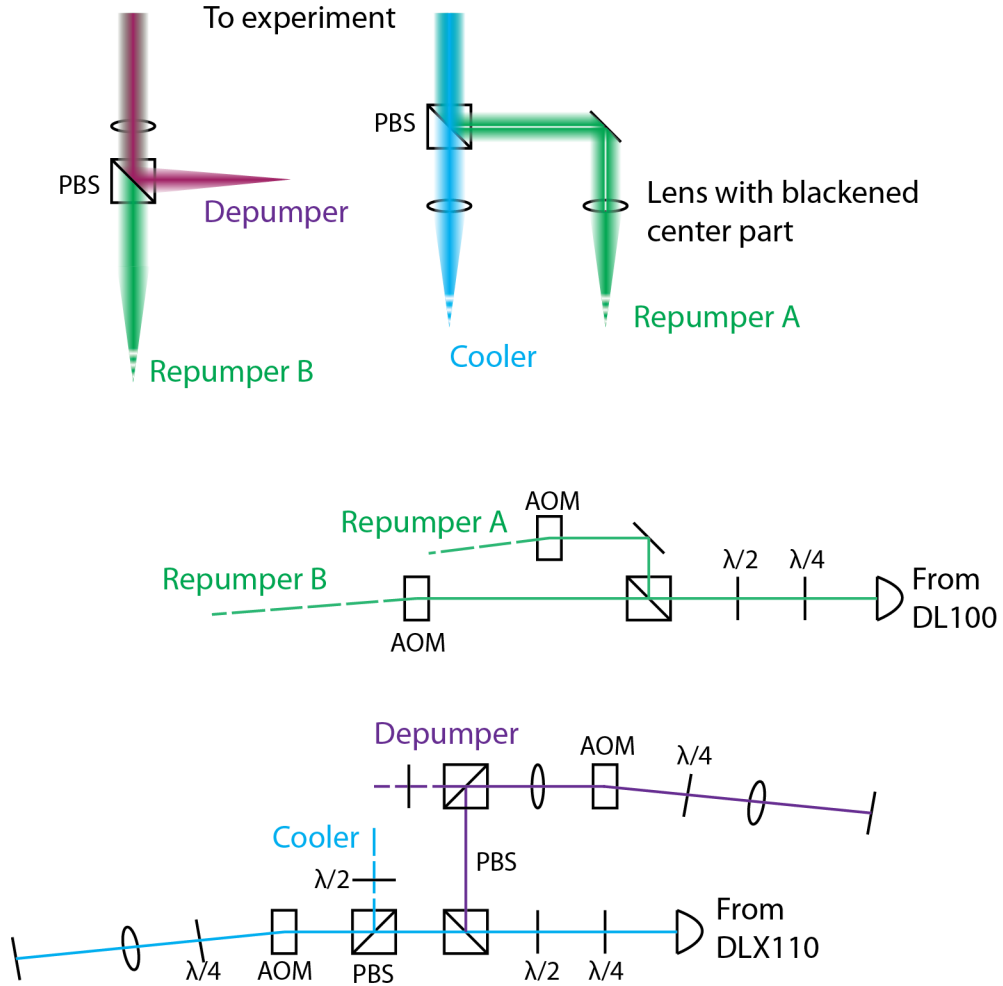


Figure 3.2.: Drawing of the beam setup used for the MOT, the DLX110 and DL100 are being locked using a FM-locking card which gets its signal from a fast photodiode not shown in this picture. The setup for the locking is essentially the same as the double pass AOMs shown here but furthermore includes a spectroscopy gas cell and mentioned fast photodiode.

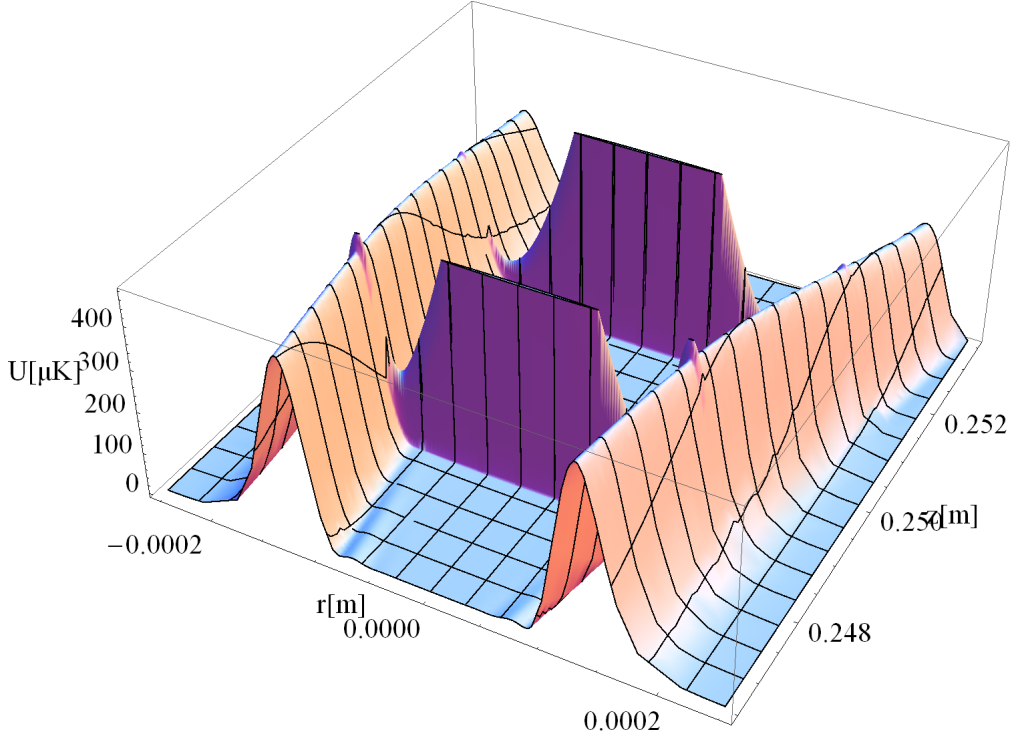


Figure 3.3.: Potential of the lens-axicon combination with lightsheets generated by cylindrical lenses.

where ω is the beam waist at the lens-axicon position, A_p the aperture size, $q(z)$ the complex curvature of the gaussian beam, R the target ring radius, and B_J the BesselJ function. Shown in fig. 3.3 is the potential of the described system including the light-sheet plugs symmetrically separated from the focal point of the ring potential. By adding two more light sheets generated by squeezing a gaussian beam using cylindrical lenses we can add two steep plug walls to close the hollow beam. We estimated a required power of about 3W at 775nm wavelength to reach a trap depth of $330\mu\text{K}$ at the peak and $180\mu\text{K}$ around 1mm after the focal ring. Along with the dipole trap we have to shine in our compensation beam which will suppress the differential light shift. As it should spatially match the trap potential as good as possible we overlap it with the trapping beam before both are being fed into the PM-fiber which is fed to the coupler targeting the lens-axicon doublet. There will only be a small deviation in beam profile according to chromatic aberration which we cannot compensate for in our system. The actual compensation beam is being derived from the repumper laser via FO lock and centered between the groundstates ($[5S_{1/2} |F=1\rangle + 3.417\text{GHz}] \rightarrow 5P_{3/2} = [5S_{1/2} |F=2\rangle - 3.417\text{GHz}] \rightarrow 5P_{3/2}$) [51, 79].

3.3. Complete setup

In fig. 3.4 we can see conceptual drawings of the complete optical setup regarding the experiment. The dipole trap beam is generated by a modified Sirah Matisse TX Light Ti:Saph laser with external reference cavity. It offers a broad range of selectable frequencies together with low frequency noise which is normally $\leq 50\text{kHz}$ rms linewidth when stabilized and a slow drift of $1\text{--}100\text{MHz/h}$. For the BEC lattice experiments we later removed this slow drift by locking the external cavity to another reference laser. During the experiment of the quantum memory we were not aware of this slow drift but it should also not have had any effect on the performance. The Ti:Saph itself is being pumped from a Spectra-physics Millennia Pro which can deliver up to 15W which under optimized conditions yields about 4.2W in the range $770\text{--}780\text{nm}$ [58]. As already briefly mentioned/depicted in figs. 2.1 and 3.1 we use the magnetically insensitive states $|g\rangle = |5^2S_{1/2}F=2\rangle$ and $|s\rangle = |5^2S_{1/2}F=1\rangle$ and $|e\rangle = |5^2P_{1/2}F=2\rangle$ being the intermediate excited state, although being detuned from that exact transition for the write pulse by about $10\text{--}15\text{MHz}$. The read and write lasers are homebuilt Littrow-grating stabilized diode lasers where the read laser serves as a master to lock the write laser via FO-locking [58]. The read master laser itself is being locked using an FM lock by doppler-free saturation spectroscopy reference, like the cooling and repumping lasers. Together with the MOT lasers from section 3.1 we now have all beams which are needed to perform the experiment. The atoms will be loaded to the trap inside a glass cell made by Japan cell out of Tempax glass with an AR coating on the outside. Using an ion pressure gauge and a Varian Starcell ion getter pump we can reach a pressure of $1.5 \cdot 10^{-9}\text{mBar}$ when the dispenser is switched off and $2\text{--}3 \cdot 10^{-9}\text{mBar}$ when on[51]. To define the quantization axis of the atomic ensemble we supply a magnetic field of 340mG along the axial direction of the trap.

3.4. Dephasing mechanisms

Now we would like to clarify some of our previous choices in light of the various decoherence mechanisms one faces when setting up a quantum memory like the one presented herein. We can evaluate the evolution of the stored spinwave by[79]:

$$|\psi\rangle = \frac{1}{\sqrt{N}} \sum_j^N e^{i\omega_j t} e^{i\Delta\mathbf{k}\mathbf{r}_j} |g \dots s_j \dots g\rangle \quad (3.5)$$

Where N is the number of atoms, ω_j is the hyperfine split of the j -th atom, $\Delta\mathbf{k}$ the momentum transfer from photons to atoms and \mathbf{r}_j the j -th's atom position[79]. Obviously one should maintain the number of atoms constant as good as possible during our storage, but for this one also has to consider that a normal cold atom cloud would diffuse and could in principle leave the read-out area of our beams. It has thus to be understood that the atoms should actually be confined to a space which is smaller or maximally of same size as the readout beam which we ensure in our setup by the blue dipole trap. Strongly

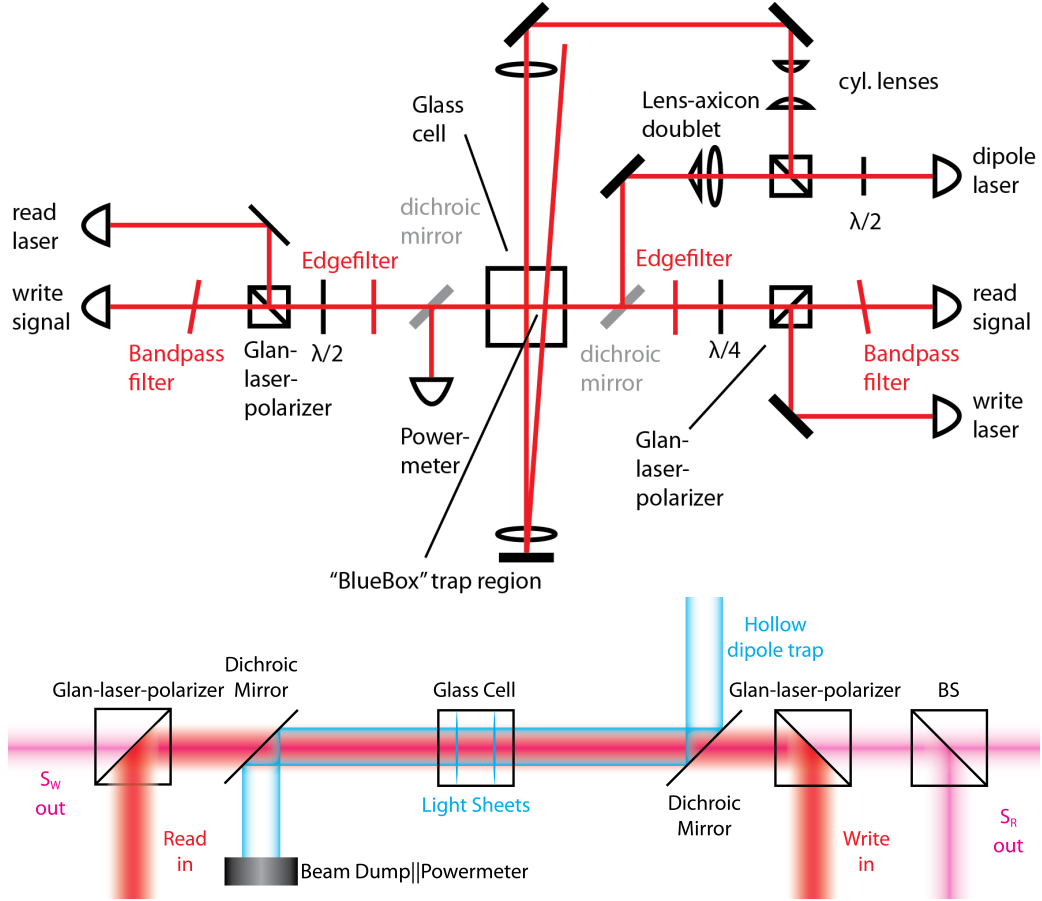


Figure 3.4.: Drawings showing the optical setup of the experiment, drawing 1 shows more elements pertaining the immediate surrounding of the trap whereas drawing 2 highlights the different beam paths and their individual usage only at the central region surrounding the glass cell, omitting filters and waveplates. The beamsplitter in the lower drawing actually comes much later in the real experiment, in the upper drawing we see the read port fiber coupler which leads the read-photons to an etalon after which the beamsplitter and accompanying single photon detectors are placed.

associated to our trap shape come the restrictions on the effect of the $\Delta\mathbf{k}$ momentum transfer: even in a trap the atoms will move freely within the confined walls, by doing so they will change the shape of the imprinted spinwave. Without a trap they would unrestrictedly dissipate with velocities given by the Boltzmann distribution:

$$p(v) = \left(\frac{m}{2\pi k_B T} \right)^{3/2} e^{-\frac{mv^2}{2k_B T}} \quad (3.6)$$

and we can evaluate the position change in eq. (3.5) as being $r(t) = \sqrt{\frac{k_B T}{m}} t$. In a previous experiment[83] it was shown that the angle between write and read-out beam plays a crucial role in determining the spinwave wavelength and that by choosing a small angle the wavelength can be extended up to about 4.4cm [70] ⁽³⁾ which is by far larger than the trapped ensemble. At such a length the atomic movement will not affect the evolution of the spinwave along the longitudinal mode⁴, another method is to confine the atoms within a lattice as described in [84].

We use the so called clock-states for our memory as they are unsensitive to magnetic fields to the first order, theoretically they should be stable enough to be used as memory states for seconds. An extensive analysis on the effects of magnetic fields in combination with clock-states can be found in [70]. Another major improvement in our setup was the compensation of the differential light shift of our dipole trap as already mentioned in section 3.2. To explain this we first have a look again at eqs. (3.1) and (3.2), if we incorporate a more detailed picture by calculating the transition strengths by including the Clebsch-Gordon coefficients in eq. (3.2) we see that the energy difference between the two ground states ($|g\rangle, |s\rangle$) is actually dependent on the position in the potential. This change in energy between the two states can be interpreted again as an oscillatory phase (ω_j in eq. (3.5)) which leads to dephasing. To better estimate the strength of this effect we weighted the energy difference with the estimated atomic density in the atomic trap which we could approximate by a formula given in [4]:

$$n(\mathbf{r}) = \frac{1}{\Lambda^3} \sum_{j=1}^{\infty} j^{-3/2} e^{j(\mu - U(\mathbf{r})) / (k_B T)} \quad (3.7)$$

³In the case of 0° we can take $\lambda = \frac{2\pi}{\Delta k}$ where Δk will be determined from the transition frequency between $|g\rangle$ and $|s\rangle$, in our case also about 4.4cm from the 6.8GHz difference of $|g\rangle = |5^2 S_{1/2} F = 2\rangle$ and $|s\rangle = |5^2 S_{1/2} F = 1\rangle$.

⁴The transversal mode will be affected, however.

where $U(\mathbf{r})$ needs to be approximated by a power-law potential and μ can be solved from [53, 4]:

$$U(\mathbf{r}) = \varepsilon_1 |x|^p + \varepsilon_2 |y|^l + \varepsilon_3 |z|^q \quad (3.8)$$

$$\rho(\varepsilon) = \frac{2\pi(2M)^{3/2}}{h^3} \frac{1}{\varepsilon_1^{1/p} \varepsilon_2^{1/l} \varepsilon_3^{1/q}} \varepsilon^\eta F(p, l, q) \quad (3.9)$$

$$\eta = \frac{1}{p} + \frac{1}{l} + \frac{1}{q} + \frac{1}{2} \quad (3.10)$$

$$F = \int_{-1}^1 (1 - |X|^p)^{1/2+1/q+1/l} dX \int_{-1}^1 (1 - |X|^p)^{1/q+1/2} dX \int_{-1}^1 (1 - |X|^q)^{1/2} dX \quad (3.11)$$

$$n_\varepsilon = e^{-(\varepsilon - \mu)/(k_B T)} \quad (3.12)$$

$$N = \int_0^\infty n_\varepsilon \rho(\varepsilon) d\varepsilon \quad (3.13)$$

by integrating over the weighted potential we can calculate the mean fluctuation of energy difference μ and the associated σ . Finally the estimated dephasing time can be estimated as [53]:

$$\tau = \frac{h}{k_B \sigma} \quad (3.14)$$

If we now introduce a beam which is locked to the frequency centered between our memory states we can compensate the differential light shift by tuning the beam intensity to the appropriate strength. Under ideal conditions (perfect mode matching, no chromatic aberrations in the optics) one would negate the differential light shift when:

$$\tilde{\omega}_{HF}(\mathbf{r}) - \omega_{HF} = \frac{\pi c^2 \Gamma \omega_{HF}}{\omega_0^3} \left(\frac{I(\mathbf{r})}{\Delta_{eff} - \left(\frac{\omega_{HF}}{2}\right)^2} - \frac{I'(\mathbf{r})}{\left(\frac{\omega_{HF}}{2}\right)^2} \right) = 0 \quad (3.15)$$

with $\Delta_{eff} = (\Delta_{2,F=1} + \Delta_{2,F=2})/2$ being the effective detuning from the centered frequency between the ground states. The required intensity to compensate the differential light shift can be calculated as:

$$I'(\mathbf{r}) \simeq \left(\frac{\omega_{HF}}{2\delta} \right)^2 I(\mathbf{r}) \quad (3.16)$$

In figure fig. 3.5 we can see how different values larger or smaller than the ideal value leave a residual potential which leads to oscillation in the spinwave. The effect is strongest at the border of the trap as the light is stronger here and it is important to mark that it stays at a small value at the centered parts of the trap. From our calculations including such a compensation beam we estimated a lifetime up to 300ms.

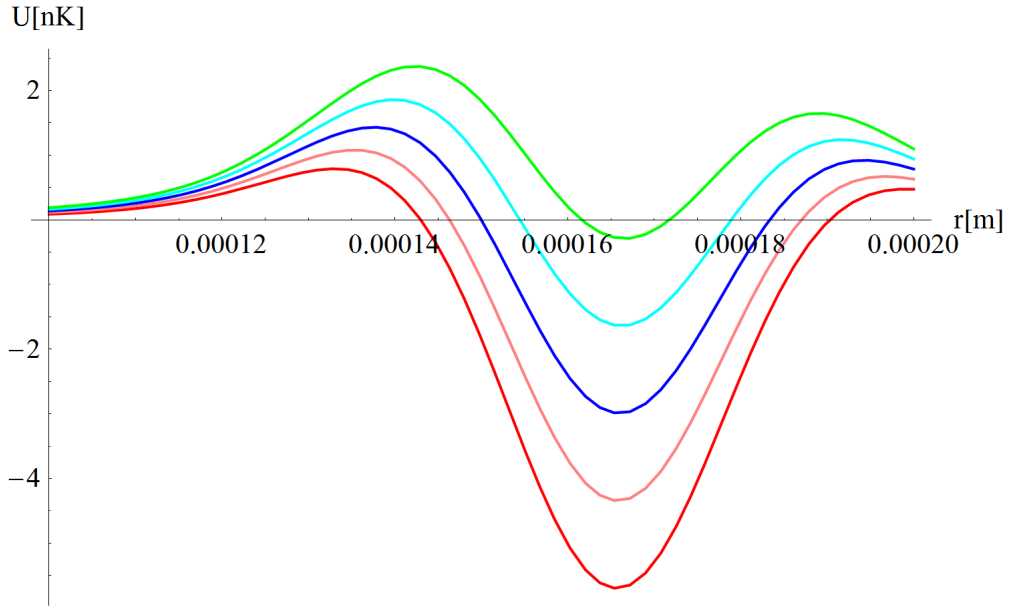


Figure 3.5.: Differential light shift for different powers of the compensation beam: blue is the ideal case of $\sim 4.5\mu\text{W}$, red, pink together with green and cyan differ in strength by $\pm 0.5; 0.25\%$ from nominal power. The calculation is carried out for a 1.75W , 776nm hollow dipole trap at the focal ring and the optimal power has been derived by iteratively minimizing the residual absolute light shift at this position.

4. Experiment

4.1. Procedures and lifetime observations

The experimental sequence was controlled by a “Logic Box” developed from the Elektronische Werkstatt des Physikalischen Instituts which is basically an FPGA which can be conveniently programmed by a Labview interface. The Logic Box provides a fixed, numbered amount of gate-generators and/or sequencers, in addition there are basic (also limited and numbered) logic elements like AND/OR/XOR, Flip Flops and so on depending on the firmware of the FPGA. Those logic elements can be freely rewired to several clocks, in- and outputs to either detect or provide TTL signals. As the Labview interface only has to modify the Bootloader of the FPGA it saves the huge amount of time VHDL would take to program the FPGA while on the other hand the user is quite limited in the available elements. This is due to the fact that each Labview represented element, e.g. AND operand’s in and outputs have to be selectably multiplexed with each other possibly placeable element in the actual firmware which scales with $O(n^2)$ of the sum of the possible in/outputs. The Box itself supports, depending on model, 20 in/out or only dedicated outputs using Lemo connectors and TTL signal standard. The speed of the FPGA is 100MHz and thus allows us to program sequences with an accuracy of 10ns.

For the experiment we loaded 3×10^6 atoms at a temperature of $15\mu K$ after first being cooled for 150ms in the Dark-MOT and additional 6ms sub-Doppler Molasses cooling. The atoms are directly loaded into the hollow-beam trap by keeping it on all the time during the cooling processes. Once we have loaded the dipole trap with enough cold atoms we let the remaining ones outside fall away and turn on a magnetic field of 340mG to define the magnetization axis along the axial direction[79]. After preparing the atoms in the $|G\rangle$ state by optical pumping we can start out with the main experimental sequence.

We used two ways to measure the efficiency of our quantum memory which we will present here now and discuss their differences: In the “normal mode” we continuously load the atoms for a short time (5-200ms) and have experiment cycles of about 20ms length during which time we probe the system using off-resonance Raman scattering. We always shine a short write pulse to the atoms, detect the confirming “write photon”¹ with a Single Photon Detector D_W (Perkin Elmer SPCM-AQR-13), wait the desired storage time, shine the read pulse and observe the correlation on D_2 and D_3 . In between such a read-write trial we always repump the atoms back to the ground state using the de- and repumper B.

¹This is not guaranteed.

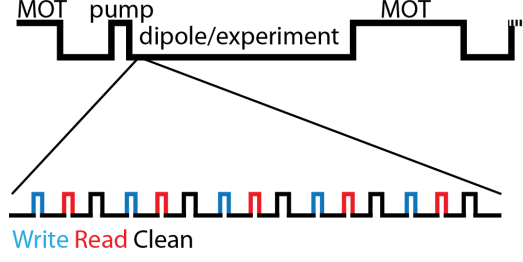


Figure 4.1.: Timeline sketch of the “normal mode” quantum memory measurement.

The detection hits are recorded and stored with a fast P7888 card and evaluated afterwards. To calculate the coincidence we use the stored hits as:

$$\chi = \frac{N_W}{N_{cyc}} \quad (4.1)$$

$$\eta = \frac{c_{W2} + c_{W3}}{N_W} \quad (4.2)$$

where χ is the write efficiency, N_W the number of registered successful write attempts, N_{cyc} the total number of cycles, η the retrieve efficiency and c_{ii} marks the coincidence between indicated detectors. The cross-correlations are calculated as:

$$g_{W2}^{(2)} = \frac{p_{W,2}}{p_W p_2} = \frac{c_{W2}/N_{cyc}}{N_W/N_{cyc} N_2/N_{cyc}} \quad (4.3)$$

$$g_{W3}^{(2)} = \frac{p_{W,3}}{p_W p_3} = \frac{c_{W3}/N_{cyc}}{N_W/N_{cyc} N_3/N_{cyc}} \quad (4.4)$$

and the auto-correlation is given by:

$$\alpha = \frac{p_{W,2,3}}{p_{W,2} p_{W,3}} = \frac{c_{W23}/N_{cyc}}{\frac{c_{W2} + c_{W3}}{N_{cyc}}} \quad (4.5)$$

which allows a measure of the total noise in the system as the coincidence between detector 2 and 3 could also be attributed to environmental noise.

Another mode of operation which we call “triggered mode” where we use EIT and send control pulses of $200\mu W$ to the atomic ensemble from the original read port and probe pulses of single-photons along the original write port. We continuously write and clean the ensemble until a confirming “write photon” is being detected. Only if such a write photon is being detected we increase the successful write count and the clean cycle will be suspended while we wait for the preset memory time (in general longer than in normal mode) after which we will shine a strong read pulse and again detect the read out photon in detector 2 or 3.

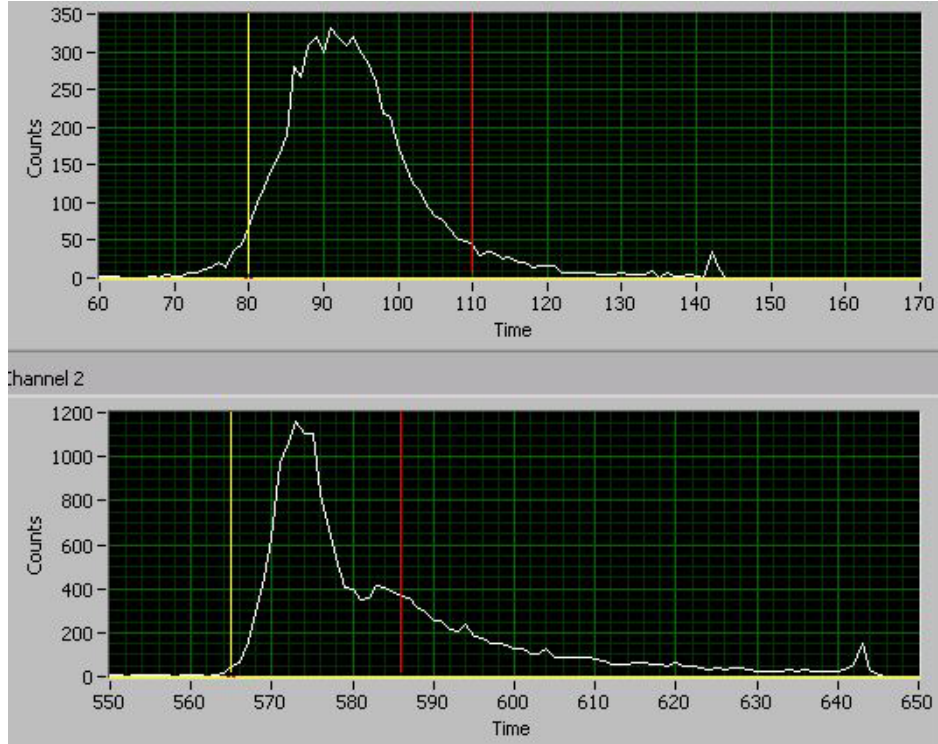


Figure 4.2.: Detector signals obtained during a “normal mode” type measurement, showing the initial sharp rise and slow decay of single photon arrival probabilities on D_2 and D_3 . Picture taken from [51].

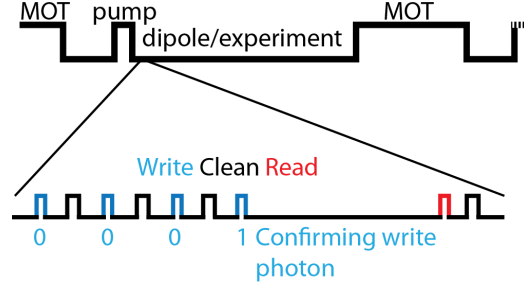


Figure 4.3.: Timeline sketch of the “triggered mode” quantum memory measurement.

In this mode we only have the amount of successful writes as we discarded the unsuccessful cycles directly by the hardware control.

$$\chi = \frac{N_{SW}}{N_{cyc}} \quad (4.6)$$

$$\eta = \frac{N_2 + N_3}{N_{SW}} \quad (4.7)$$

From this measurement we can characterize the retrieve efficiency for long storage times of the memory. We obtained retrieve efficiencies of 7% using Raman scattering, which can be recalculated for mode matching, transmittance loss and detection efficiency to be initially 30% whereas EIT has an intrinsic 22% retrieve efficiency which is comparable to the Raman scattering[79]. The storage time however is $0.67 \pm 0.03\text{ms}$ for the uncompensated case which matches well the prediction but only $1.44 \pm 0.09\text{ms}$ in the compensated case which is far off from our initial estimate of 300ms. A deeper analysis showed that there are oscillatory revivals and decays of the retrieve efficiency on longer time scales and that we can fit an exponential decay to that retrieve efficiency with a decay constant of $28 \pm 2.5\text{ms}$.

4.2. Transversal mode revival of the quantum memory spinwave

To explain the sudden decay with later revival of our memory lifetime we analysed the transversal mode matching of our spinwave using a Monte-Carlo simulation. The simulation was programmed in C++, using OpenGL for the visualization of the temporal evolution of the spinwave. Using a 2D ring potential with the same radius as at the focal point of our blue detuned semi-cone we imprint a gaussian spinwave to the atoms and let them evolve under gravity and collisions with the potential. Because of the short timescales and very diluteness we can ignore inter-atom collisions in our model. Regarding the potential walls we implemented a first order, hard-core collision detection. To obtain the retrieve efficiency in this model we only need to overlap the spinwaves

resulting from the initial imprint and the evolved atom positions by:

$$R(T) = \left| \int \sqrt{U(x, y, 0)} \sqrt{U(x, y, T)} \right|^2 \quad (4.8)$$

where $U(x, y, 0)$ is the originally imprinted gaussian spinwave and $U(x, y, T)$ the evolved spinwave at time T . In our simulation we use a grid of 81×81 cells which represent the actual spinwave and seed an area of size equal to our potential circle at the focal point with particles ranging up to $N = 10^7$, randomly assign speeds according to the Boltzmann distribution for atoms at $T = 15\mu K$ and imprint them with a normalized value which corresponds to their initial placing according to a gaussian shape of the write mode.

This includes the assumption that the atomic ensemble has a Fresnel number of order 1, otherwise higher modes could be excited in the ensemble as well[65] and the mode matching would not be as good. We then transfer the individual imprints of each atom to the responsible cell it resides in and normalize the total cell-spinwave to 1. We let the atoms evolve as mentioned and finally retrieve the final overlap of the spinwaves given by eq. (4.8). Evolution stages of the spinwave can be seen in fig. 4.4, and a comparison of retrieve efficiencies shown in fig. 4.5. With the help of the MC simulation we can now explain the oscillatory revivals of the spinwave, in fig. 4.5 a) we see key points 1-5 marked throughout 0-8.2 ms which show how the initially gaussian spinwave deforms and temporarily aggregates anew at the bottom of the trap before bouncing back to the center and reforming there a similar shape to the original. Of course the waveform which is formed by the atoms which bounce back from the bottom is not exactly the same and will thus only produce a partial amount of retrieve efficiency compared to the initial one. With increasing time the movement of the atoms becomes more random and the spinwave distribution flattens out preventing further revivals.

The effect of revival and decay is even more pronounced if the imprint beam is spatially mismatching from the center of the trap which we verified by moving the beam approximately $60\mu m$ upwards. A further effect which we considered and can be directly included in the model is atom loss where we can just multiply the normalized curve with the expected decay at a given time.

The remaining discrepancies between this model and the experimental data can be attributed to trap inhomogeneity and limits from a 2D model compared to the 3D trap, especially as the real trap is not cylindrical but slightly conical. Furthermore a too high Fresnel number would allow for loading into higher excited modes as explained in [65] which would further complicate to find a matching outgoing mode. From the dimensions of our ensemble it has a Fresnel number > 20 but by adapting the corresponding waist and opening angle from the couplers the effective Fresnel number can be fixed and reduced again[70]. There might still be a slight mismatch though which could also account for bad performance.



Figure 4.4.: Snapshots of the transversal mode of the quantum memory. The simulation had $10 \cdot 10^6$ particles, the imprinted gaussian estimated as having $130\mu m$, the trap $160\mu m$, a vertical displacement of $60\mu m$, $15\mu K$ Temperature, a 81×81 discretization grid and $20ms$ total evolution time ($200\mu s$ per picture) whereas the simulation runs at $20\mu s$ resolution).

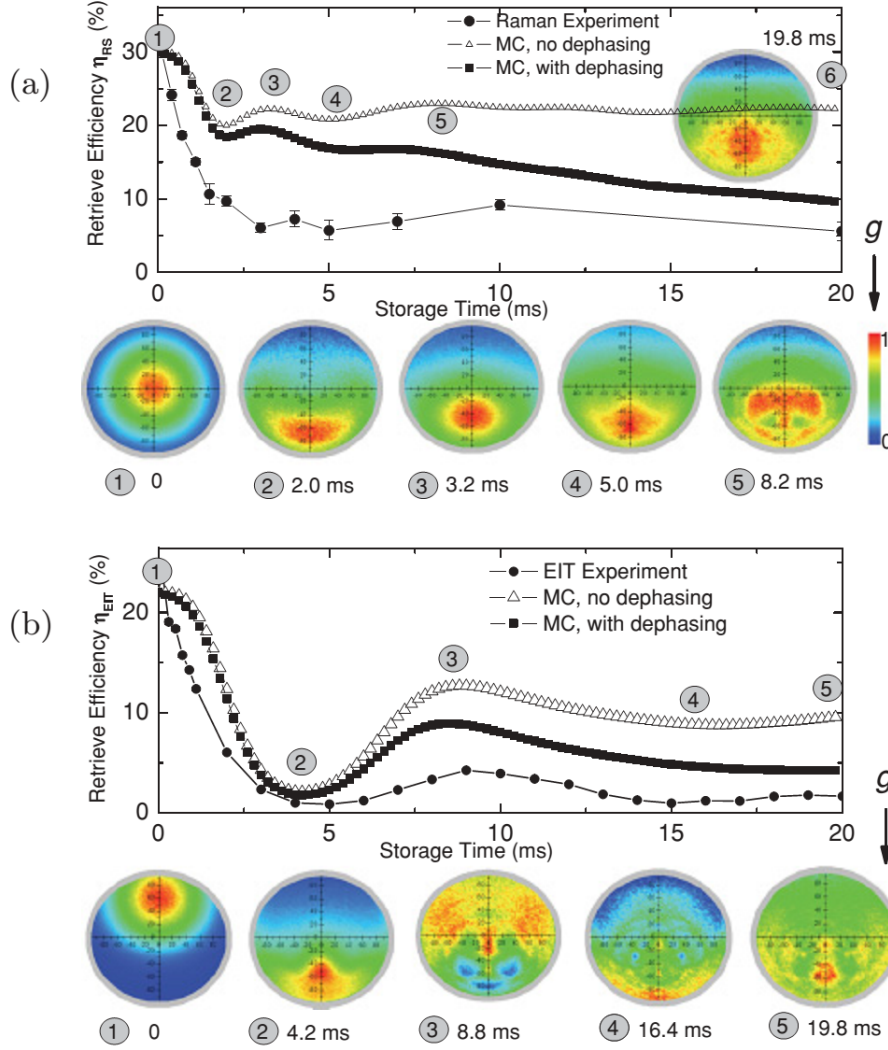


Figure 4.5.: Retrieve efficiencies of the quantum memory for 20ms (picture taken from [79]), we compared retrieve efficiencies and collapse/revival for two cases. In figure a) the gaussian mode is centered well on the trap and the revivals are not as strongly visible than in case b) where the beam is shifted by $60\mu\text{m}$ away from the ensemble center. The empty triangles are the pure MC simulation data from which we can get the filled squares by multiplying it with the atom loss (exponential decay fit to atom number measurement) and the expected dephasing from light shift. As seen in both figures the simulated shape matches the measurement well and key points can be identified in both simulation and measurement. Especially in figure b) the mechanism of revival and decay cycles is apparent throughout points two to five. The discrepancies in amplitude can be attributed to the restriction of the simulation to 2D versus a 3D system and simplifications of the potentials.

Part II.

Experiments on a 2D optical lattice towards atom entanglement.

5. Motivation and theoretical backgrounds for experiments regarding 3D/2D ultracold atoms and optical lattices

5.1. Bose-Einstein condensation

Bose-Einstein condensation (BEC) was first predicted by Bose and Einstein in 1924/25[18, 19], it was not until 1995, however, until the first condensates were produced by Cornell at JILA and Ketterle at MIT[55, 12]. Many interesting experiments using BECs have been done since and are still being performed, we will turn our focus in particular on systems including optical lattices which provide even deeper possibilities of study. With the usage of optical lattices one can simulate complex Hamiltonians, in section 7.1 we will discuss Bloch Oscillations, while in section 8.1 we will turn to experiments regarding superlattices.

Based on the experiments discussed in [61, 57] and [49] we aim for the 4-atom GHZ entangled state as a milestone towards large-scale entanglement using neutral atoms on optical lattices. As shown in those experiments it is already possible to selectively manipulate single atoms reliably without disturbing neighbors on the lattice.

We will go into more details in the respective chapters and start now to provide a brief introduction to BEC. We will follow now with excerpts from [11] for the theory of BEC and then the key points about BKT from [31] in two dimensions. The outline for calculating BEC is normally the assumption of a harmonic trap potential like:

$$V(\mathbf{r}) = \frac{m}{2} (\omega_x^2 x^2 + \omega_y^2 y^2 + \omega_z^2 z^2) \quad (5.1)$$

In a basic simplification one can start out for the case of non-interacting particles, which is normally not the case in most experiments. Of course one might use Feshbach-resonances to tune the used atoms interaction strength/scattering length to a non-interacting regime, and produce BEC [47, 77] as well. Even though our BEC of ^{87}Rb will be interacting we start out with this easier describable case as in [11], where the eigen-energy for N non-interacting particles is just the sum over the energy of each individual particle:

$$\epsilon_N = \sum_i \left(n_i + \frac{1}{2} \right) \hbar \omega_i \quad (5.2)$$

with $i = x, y, z$ and $N = n_x n_y n_z$. If all particles are in the single-particle groundstates

(all $n_i = 0$) we can define the overall ground-state as:

$$\phi((r)_1 \dots (r)_N) = \prod_i \Phi_0(\mathbf{r}_i) \quad (5.3)$$

with Φ_0 given by:

$$\Phi_0(\mathbf{r}) = \left(\frac{m\omega_{ho}}{\pi\hbar} \right)^{3/4} e^{-\frac{m}{2\hbar}(\omega_x x^2 + \omega_y y^2 + \omega_z z^2)} \quad (5.4)$$

where ω_{ho} , the geometric average frequency is defined as:

$$\omega_{ho} = (\omega_x \omega_y \omega_z)^{1/3} \quad (5.5)$$

The density distribution of such a non-interacting gas is then given by:

$$n(\mathbf{r}) = N|\Phi_0(\mathbf{r})| \quad (5.6)$$

whereas the size of the cloud is fixed by the harmonic oscillator length of the trap frequency/ies:

$$a_{ho} = \left(\frac{\hbar}{m\omega_{ho}} \right)^{1/2} \quad (5.7)$$

which of course does not reflect well the structure an interacting BEC poses. To recover the well known Thomas-Fermi shape, it is necessary to refine the theoretical model by introducing interactions between the involved particles. The Hamiltonian describing N interacting bosons is given by [11]:

$$\hat{H} = \int d\mathbf{r} \hat{\Psi}^\dagger(\mathbf{r}) \left[-\frac{\hbar^2}{2m} \nabla^2 + V_{ext}(\mathbf{r}) \right] \hat{\Psi}(\mathbf{r}) + \frac{1}{2} \int d\mathbf{r} d\mathbf{r}' \hat{\Psi}^\dagger(\mathbf{r}) \hat{\Psi}^\dagger(\mathbf{r}') V(\mathbf{r} - \mathbf{r}') \hat{\Psi}(\mathbf{r}') \hat{\Psi}(\mathbf{r}) \quad (5.8)$$

where the first term describes our normal system using bosonic creation and annihilation operators and the second term describes the interaction of particles using a two-body potential $V(\mathbf{r} - \mathbf{r}')$. By using Bogoliubov's ansatz we can rewrite $\hat{\Psi}(\mathbf{r}, t)$ as $\hat{\Psi}(\mathbf{r}, t) = \phi(\mathbf{r}, t) + \hat{\Psi}'(\mathbf{r}, t)$ where $\hat{\Psi}'$ is a perturbation to the expectation value of the field operator $\phi(\mathbf{r}, t)$ which is equivalent to the density by: $n_0(\mathbf{r}, t) = |\phi(\mathbf{r}, t)|^2$. The whole evolution of the wavefunction can be evaluated in the Heisenberg picture by [11]:

$$i\hbar \frac{\partial}{\partial t} \hat{\Psi}(\mathbf{r}, t) = [\hat{\Psi}, \hat{H}] = \left[-\frac{\hbar^2 \nabla^2}{2m} + V_{ext}(\mathbf{r}) + \int d\mathbf{r}' \hat{\Psi}^\dagger(\mathbf{r}, t) V(\mathbf{r}' - \mathbf{r}) \hat{\Psi}(\mathbf{r}', t) \right] \hat{\Psi}(\mathbf{r}, t) \quad (5.9)$$

to solve this equation one approximates the interatomic potential by a direct contact delta-function scaled by an interaction constant:

$$V(\mathbf{r}' - \mathbf{r}) = g\delta(\mathbf{r}' - \mathbf{r}) \quad (5.10)$$

$$g = \frac{4\pi\hbar^2 a}{m} \quad (5.11)$$

where a is the scattering length. This approximation is valid for ultracold gases where primarily two-body collisions governed by s-wave scattering take place. When one inserts those approximations back into eq. (5.9) and uses Bogoliubov's ansatz it yields:

$$i\hbar \frac{\partial}{\partial t} \Phi(\mathbf{r}, t) = \left(-\frac{\hbar^2 \nabla^2}{2m} + V_{ext}(\mathbf{r}) + g|\Phi(\mathbf{r}, t)|^2 \right) \Phi(\mathbf{r}, t) \quad (5.12)$$

which is the famous Gross-Pitaevskii equation. To calculate the ground state of the GPE one can use mean-field theory, by rewriting the wave function as:

$$\Phi(\mathbf{r}, t) = \phi(\mathbf{r}) e^{-i\mu t/\hbar} \quad (5.13)$$

we can rewrite the GPE as:

$$\left(-\frac{\hbar^2 \nabla^2}{2m} + V_{ext}(\mathbf{r}) + g\phi^2(\mathbf{r}) \right) \phi(\mathbf{r}) = \mu \phi(\mathbf{r}) \quad (5.14)$$

where μ is the chemical potential, and ϕ is a wavefunction normalized to N and the mean-field is proportional to $n(\mathbf{r}) = \phi^2(\mathbf{r})$. For the noninteracting case this equation still yields a gaussian density distribution except that it is scaled by \sqrt{N} . Before we directly continue with the case for repulsing interactions (which we are primarily interested in, as we deal with ^{87}Rb), we would like to mention a useful expression obtained by direct integration of the GPE [11]:

$$\mu = (E_{kin} + E_{ho} + 2E_{int})/N \quad (5.15)$$

When one ignores the quantum pressure term ($\nabla^2 \sqrt{n(\mathbf{r})}$ in eq. (5.14)) which is only important at the boundary, one can simplify eq. (5.14) to the so called Thomas-Fermi approximation:

$$n(\mathbf{r}) = \phi^2(\mathbf{r}) = g^{-1}(\mu - V_{ext}(\mathbf{r})) \quad (5.16)$$

which combined with the normalization constraints yields:

$$\mu = \frac{\hbar\omega_{ho}}{2} \left(\frac{15Na}{a_{ho}} \right)^{2/5} \quad (5.17)$$

for the chemical potential. For a spherical trap potential one can calculate the radius of the inverted parabola of the TF density distribution by using $\mu = m\omega_{ho}^2 R^2/2$ as:

$$R = a_{ho} \left(\frac{15Na}{a_{ho}} \right)^{1/5} \quad (5.18)$$

Finally the density at the center of the BEC can be compared to the value of the non-interacting case by:

$$n_{ho}(0) = \frac{N}{\pi^{3/2} a_{ho}^3} \quad (5.19)$$

$$n_{TF}(0) = \frac{15^{2/5} \pi^{1/2}}{8} \left(\frac{Na}{a_{ho}} \right)^{-3/5} n_{ho}(0) \quad (5.20)$$

where we see that the central density is lower for the TF distribution compared to the non-interacting case. Absorption imaging has been and is still one of the standard procedures of analyzing BECs. If one knows the trap frequencies it is directly possible to calculate important properties out of a TOF sequence using[11, 71]:

$$R_i(t) = R_i(0)b_i(t) = \sqrt{\frac{2\mu}{m(2\pi f_i)^2}}b_i(t) \quad (5.21)$$

$$\ddot{b} = \frac{(2\pi f_i)^2}{b_i b_x b_y b_z} \quad (5.22)$$

5.2. The BKT-transition

We now turn to the BKT transition which can occur in 2D systems and summarize key points here taken from the theoretical deduction given in [31, 32]. By confining an atomic gas into a narrow sheet inside a normal trap one can effectively reduce the dimensionality of the gas to 2D. This can be achieved e.g. by adding a high¹ optical potential from two dipole trap beams crossing under an angle θ : the originally 3D trap will be split into several effectively 2D planes with a period

$$l = \frac{\lambda}{2 \sin(\theta/2)} \quad (5.23)$$

Depending on the chosen geometry it is possible to then trap atoms in one, two or even multiple of such sheets and perform experiments. This change of dimensionality has however far reaching effects: as we freeze out one dimension this will modify the interaction strength between atoms:

$$g^{(3D)} = \frac{4\pi\hbar^2 a}{m} \rightarrow g^{(2D)} = \frac{\hbar^2}{m} \sqrt{8\pi} \frac{a}{a_z} \quad (5.24)$$

where a_z is the size of the ground state of the confining lattice. When one compares the phase-space criterion for BEC for the 3D and 2D case in the MF Hartree-Fock approximation, one sees that for 3D a critical point can be found when

$$D^{3D}(\mathbf{r}) = g_{3/2}(Z)e^{-\beta V_{eff}(\mathbf{r})} \quad (5.25)$$

$$V_{eff}(\mathbf{r}) = V(\mathbf{r}) + 2g^{(3D)}n_3(\mathbf{r}) \quad (5.26)$$

has no longer a solution for $Z > 1$ in $g_{3/2}(Z)$ ⁽²⁾. Repulsing interactions in the MF approach raise the necessary number of atoms in most cases about 10% compared to the non-interacting case[31, 32]. For a 2D gas, however, no critical point can be found. If one looks at

$$D^{2D}(\mathbf{r}) = g_1(Ze^{-\beta V_{eff}(\mathbf{r})}) \quad (5.27)$$

$$V_{eff}(\mathbf{r}) = V(\mathbf{r}) + 2g^{(2D)}n(\mathbf{r}) \quad (5.28)$$

¹ $\hbar\omega_{lat} \gg k_B T$, $\hbar\omega_{lat} \gg U$ where $k_B T$ is the thermal energy and U is the interaction energy per atom.

²The polylogarithm

it either supports a finite number of atoms for the non-interacting case or an infinite amount of atoms for any non-zero repulsive interaction strength without any critical point. A different approach[31, 32] using local density approximations (LDA) can however predict the onset of the so called BKT transition from normal to superfluid. Considering a uniform system with phase space density $D = F(\mu, T)$ we can define a critical chemical potential $\mu_c(T)$ at which the superfluid transition occurs. According to $\mu_c(T)$ we will have a D_c which will depend on the interaction strength:

$$D_c = \ln \left(\frac{\xi}{\tilde{g}} \right) \quad (5.29)$$

$$\tilde{g} = g^{(2D)} \frac{m}{\hbar^2} = \sqrt{8\pi} \frac{a}{a_z} \quad (5.30)$$

If the size of the trapped gas is large enough to be described by LDA, the phase space density is given as $D(\mathbf{r}) = F(\mu - V(\mathbf{r}), T)$. A superfluid component will be present in the center region of the trap if the phase space density $D(0)$ is larger than the critical phase space density D_c [31, 36]. By rewriting eq. (5.27) we will be able to calculate the density profile of the trapped gas:

$$D(\mathbf{r}) = -\ln \left(1 - Z e^{\tilde{g}D(\mathbf{r})/\pi} e^{-\beta V(\mathbf{r})} \right) \quad (5.31)$$

depends for any temperature only on: $R^2 = (x/x_T)^2 + (y/y_T)^2$ with $x_i = 1/\sqrt{\omega_i^2 m \beta}$, $i = x, y$ and the total atom number can be calculated as:

$$N = \left(\frac{k_B T}{\hbar \bar{\omega}} \right) \int_0^\infty \tilde{D}(R) R dR \quad (5.32)$$

where $\tilde{D}(R)$ can be calculated from:

$$\tilde{D}(R) = -\ln \left(1 - Z e^{-\tilde{g}\tilde{D}(R)/\pi} e^{-R^2/2} \right) \quad (5.33)$$

As we see the important variables here are the fugacity Z , reduced interaction strength \tilde{g} and the geometric mean frequency $\bar{\omega}$ [31, 32]. We will now close with the calculation of the critical number of atoms for the 2D BKT transition using MFT: For a given interaction strength \tilde{g} one varies Z and can solve eq. (5.31) numerically.

$$\frac{N_c^{(mf)}}{N_c^{(id)}} = 1 + \frac{3\tilde{g}}{\pi^3} D_c^2 \quad (5.34)$$

The calculation for the critical number of atoms matches quite well with QMC simulations according to [31], but the density profiles close to the critical point still show some discrepancies.

5.3. Optical lattices

The potential of an optical lattice created by retroreflected beams forming a standing wave can be described by:

$$V(x, y, z) = V_0 (\sin kx^2 + \sin ky^2 + \sin kz^2) \quad (5.35)$$

where we assume equal strength of all beams, perfect overlap, neglect the gaussian shape and its Rayleigh-length. In our experiment we will of course have beams which are not equally matched - to create the 2D confinement we have a lattice created by two beams which pass under a certain angle to create the 2D “pancakes”. To describe a system of trapped atoms in such a potential we can use the stationary Schrödinger equation which we will discuss w.l.o.g. in 1D:

$$\left(-\frac{\hbar^2}{2m} \nabla^2 + V(x) \right) \psi(x, t) = E \psi(x, t) \quad (5.36)$$

Bloch’s theorem[8] can solve this equation by exploiting the symmetry of the lattice: the eigenstates have the same periodicity as the lattice and only differ by a phase factor:

$$\phi_q^{(n)}(x) = e^{iqx/\hbar} u_q^{(n)}(x) \quad (5.37)$$

where the n signifies the n-th energy band; together with Bloch’s theorem we can rewrite the Schrödinger equation as:

$$\left(\frac{\hbar^2 k^2}{2m} \frac{\partial^2}{dx'^2} + \frac{V_0}{2} (1 - \cos 2x') \right) u_q^n = E_q^n u_q^n \quad (5.38)$$

Where we have used the identity $\sin(\alpha)^2 = \frac{1}{2}(1 - \cos(2\alpha))$ to rewrite the lattice potential in a way to which we will be able to apply the solution of Mathieu’s equation. $x' = \frac{\pi}{a}x$ is the variable transform into 1st Brillouin zone space. As we’re primarily interested in interactions for the lowest band (without Landau-Zener tunneling interactions) we will focus on the solution based on the wannier functions for the localized wavefunctions. With some rewriting we can bring the total equation into Mathieu-equation form as:

$$\left[\frac{\partial^2}{\partial x'^2} + \left(\left(\frac{V_0}{2E_r} - \frac{E_0^k}{E_r} \right) - \cos(2x') \right) \right] u_n^k = 0 \quad (5.39)$$

A general solution to Mathieu’s equation (see [1]) has the form:

$$y = C_1 C(a, q, x) + C_2 S(a, q, x) \quad (5.40)$$

where C and S are Mathieu functions. With the help of Mathematica we will be able to numerically calculate the Wannier functions by using the general solution and some normalization requirements as[10]:

$$w(V_0, x, x_i) = 2L \int_0^{q_r} \cos(qkx_i) C \left[M_A \left(q, -\frac{V_0}{4} \right), -\frac{V_0}{4}, kx \right] + \quad (5.41)$$

$$\sin(qkx_i) S \left[M_A \left(q, -\frac{V_0}{4} \right), -\frac{V_0}{4}, kx \right] dq \quad (5.42)$$

where M_A is the “MathieuCharacteristicA” Mathematica function which gives the characteristic parameter a . $L = \sqrt{\frac{k}{4\pi}}$ and $q_r = 1 - \epsilon$ should be kept close below 1 to keep the solutions fixed to the first band but within sound numerical ranges. From the Wannier function it is easy to calculate the interesting parameters of our optical lattice, namely the on-site-interaction U and the hopping/tunneling term J . In units of E_r U can be given by:

$$U = g^{nD} U_g \quad (5.43)$$

with appropriate interaction constant g and:

$$U_g = \sum_{x=-\infty}^{\infty} w(V, x, 0)^4 \quad (5.44)$$

while:

$$J = \left(M_A\left(q_r, -\frac{V_0}{4}\right) - M_A\left(0, -\frac{V_0}{4}\right) \right) / 4 \quad (5.45)$$

Other popular derivations given in e.g. [35, 27, 66, 85] use (among others) Fourier expansions of the potential to calculate the bands and harmonic approximations. We present a solutions from [85] which differs a bit from our numerical calculations using Mathieu’s equation. In [85] the Bloch-wave energy for the lowest band is given as:

$$\epsilon(\mathbf{q}) = \frac{3}{2} \hbar \omega_0 - 2J (\cos q_x a + \cos q_y a + \cos q_z a) \quad (5.46)$$

and he obtains the J in the limit of $V_0 \gg E_r$ from the 1D-Mathieu equation as:

$$J = \frac{4}{\sqrt{\pi}} E_r \left(\frac{V_0}{E_r} \right)^{3/4} e^{-2\sqrt{\frac{V_0}{E_r}}} \quad (5.47)$$

and the interaction as:

$$U = g \int |\omega(\mathbf{r})|^4 = \sqrt{\frac{8}{\pi}} k a_s E_r \left(\frac{V_0}{E_r} \right)^{3/4} \quad (5.48)$$

Using the already mentioned Fourier expansion it is also very easy to calculate the Bloch-Bands from the Hamiltonian³

$$H_{l,l'} = \begin{cases} (2l + q/\hbar k)^2 E_r & \text{if } l = l' \\ -1/4 V_0 & \text{if } |l - l'| = 1 \\ 0 & \text{else} \end{cases} \quad (5.49)$$

by solving for its eigenvalues in Mathematica for given n and q . Shown in fig. 5.1 are solutions for the 1D case of a 767nm lattice for various potential depths. In a similar way it is possible to construct the Bloch-wavefunction and Wannier-functions of the system by the eigensystem of the Hamiltonian [27, 10] or use the already displayed version using Mathieu’s equations. A depiction of the Bloch-wavefunction for different quasi-momenta can be seen in fig. 5.2.

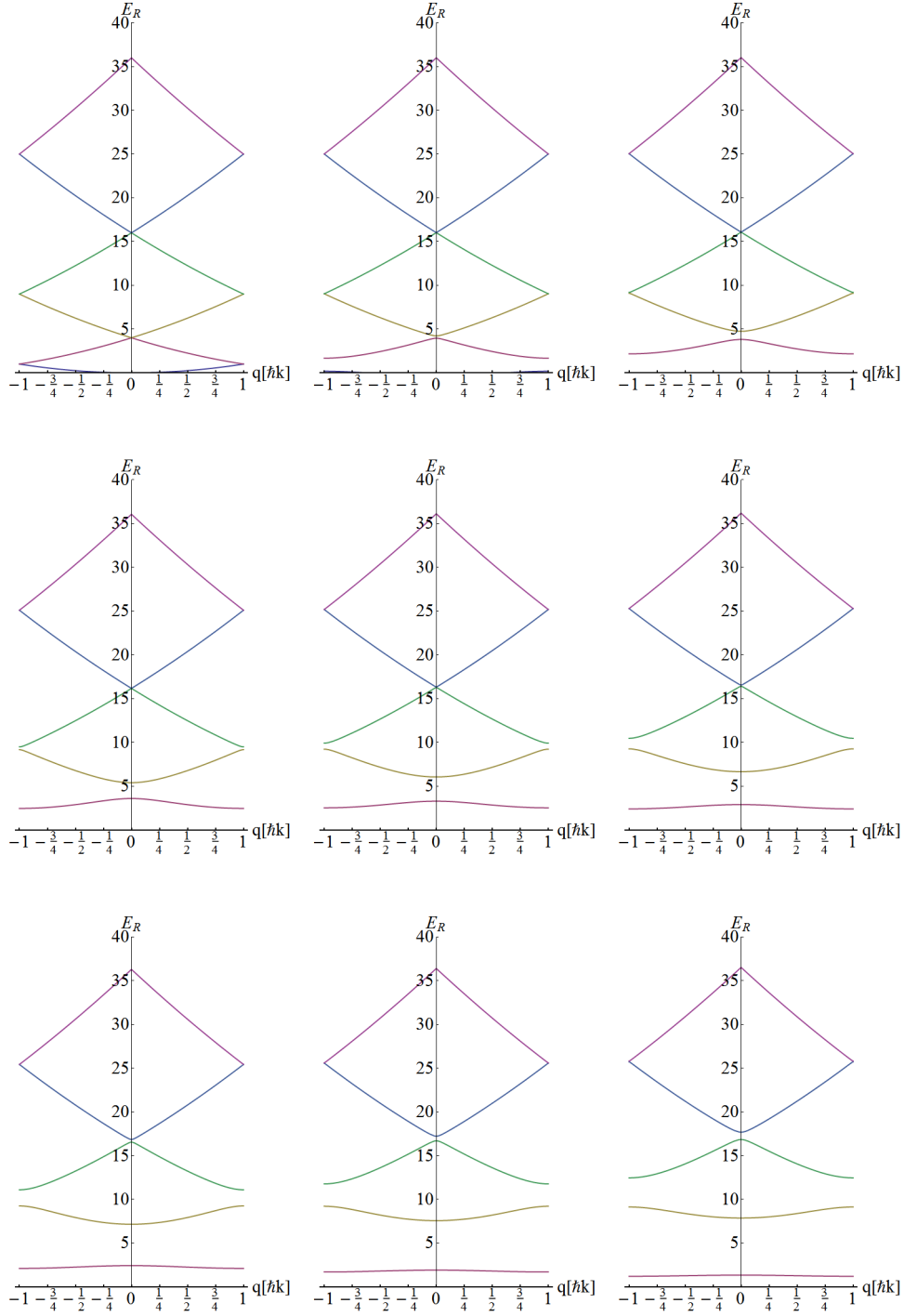


Figure 5.1.: Bloch bands for a 1D-767nm lattice for increasing potential depth from $0E_r$ to $24E_r$ in steps of $3E_r$.

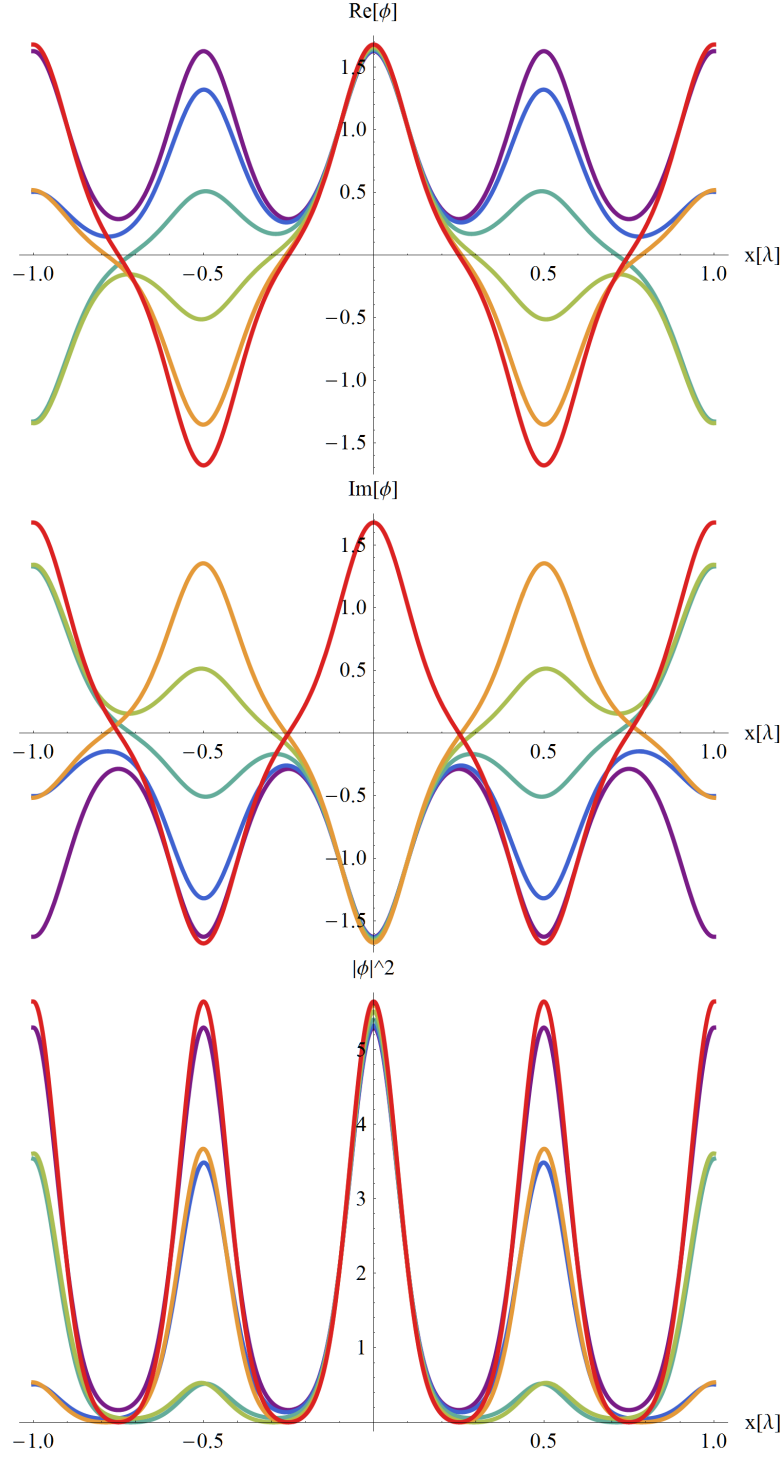


Figure 5.2.: Real, imaginary and absolute values of Bloch-Wavefunctions for quasi-momenta uniformly spaced from 0 to $\hbar k$ (increasing rainbow coloring).

The parameters U and J play an important role to characterize a system of atoms on an optical lattice. In the Bose-Hubbard model their values determine the behaviour of the system, where of great interest are the superfluid and Mott-Insulating states and the transition between the two. The Bose-Hubbard Hamiltonian in second quantization reads:

$$\hat{H} = -J \sum_{\langle ii' \rangle} \hat{a}_i^\dagger \hat{a}_{i'} + \frac{U}{2} \sum_i \hat{n}_i (\hat{n}_i - 1) + \sum_i \epsilon_i \hat{n}_i \quad (5.50)$$

where \hat{a}_i^\dagger is the creation and \hat{a}_i the annihilation operator for an atom at lattice site i . The J term describes the “hopping” between adjacent lattice sites whereas U is the on-site interaction strength between multiple atoms trying to occupy the same site. At zero temperature we can characterize the quantum phase-transitions between the superfluid state and the Mott-Insulator where we define the Superfluid state as:

$$|\psi_{SF}\rangle = \left(\frac{1}{\sqrt{M}} \sum_{i=1}^M \hat{a}_i^\dagger \right)^N |0\rangle \quad (5.51)$$

with N atoms spreading out in a macroscopical wavefunction over M lattice sites. On the other hand the many localized wavefunctions of atoms frozen into a Mott-Insulator are given by:

$$|\psi_{MI}\rangle = \prod_i^M \left(\hat{a}_i^\dagger \right)^n |0\rangle \quad (5.52)$$

In fig. 5.3 we see the phase diagram at zero temperature for superfluid-Mott transitions, depending on the parameters J/U and μ/U we will observe either superfluid (SF) phases or Mott-Insulators (MI) with different fillings. In real systems, normally one can observe a “wedding-cake” structure due to the trap shape: at the corner of the trap we either have a superfluid part or start out with a filling 1 MI and then advance to the core with higher filling MI phase(s) and intermediate SF phases between the respective MI phases. The characterization and calculation of these phase transitions is given in [22, 66].

³For derivation see [27]

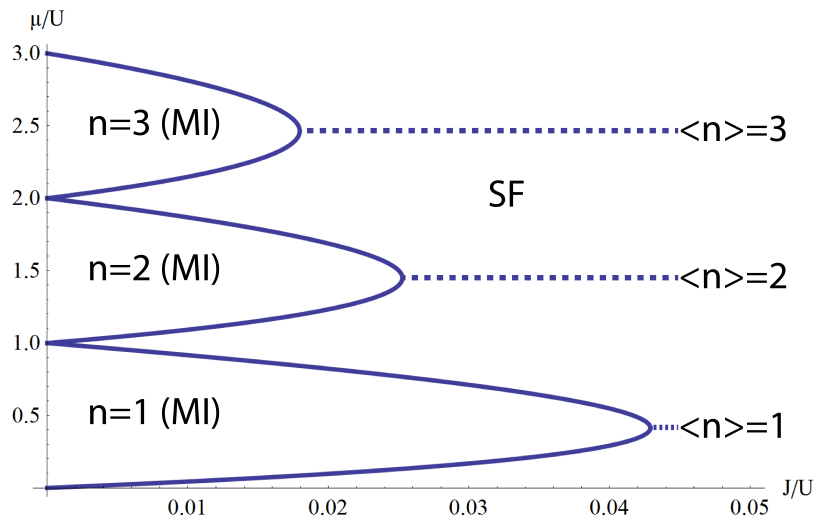


Figure 5.3.: Zero temperature phase diagram of SF-Mott transitions in a 2D lattice.

6. Our new setup

6.1. General design

In this chapter we break down the main components of our experimental system and discuss interesting features of individual components in more detail. We chose a basic design similar to the one mentioned in [26]: We have a two stage vacuum system which is connected to each other via a differential vacuum connection, depicted in fig. 6.1.

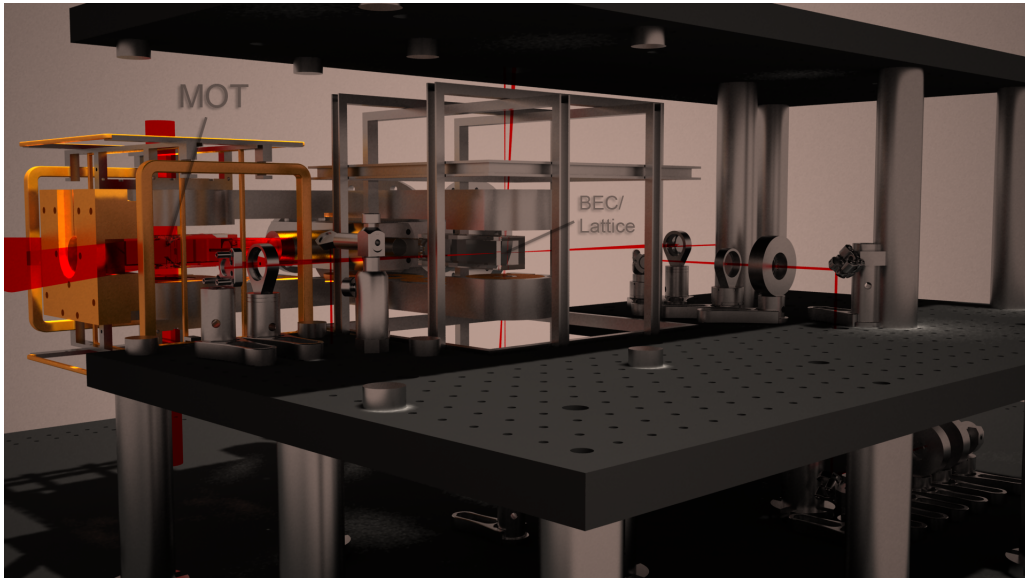


Figure 6.1.: Basic layout of our vacuum system with the two glass cells and the magnetic transfer between both cells, excluding most optics for visibility.

In the first glass cell to the left (surrounded by the copper coils) of fig. 6.1 we create a dense atom cloud using a “Dark MOT” in a high-vacuum and transfer it to the second ultra-high vacuum glass cell using an L-shaped, two layer, magnetic transfer system. In the second glass cell (centered in fig. 6.1) we can create 2D BECs for usage in experiments with 2D optical (super-)lattices using a combination of dipole beams, evaporative cooling and axial confinement beams which we will describe later in more detail. The cooling, repumping, depumping, sigma, imaging and Matisse Laser setups still reside on a secondary optical table apart from the main experiment and are being guided to the main table via fibers. The new dipole laser, long lattice laser as well as accompanying

optics are placed on the remaining space of the experiment table and are also guided by fibers to the final optical setups surrounding the glass cell. For further manipulation of the atomic states we can make use of radio-frequency and microwave coils which require a very sensitive magnetic field stabilization along the major field axis and we are planning an upgrade to include Raman-pumping beams for further state-manipulation. For the ultrahigh vacuum we use an Ion Pump and a Titanium Sublimation Pump both by Varian with which we reach a pressure of normally $< 2 \times 10^{-11}$ mbar in the BEC glass cell.

6.2. Time sequence from MOT to BEC

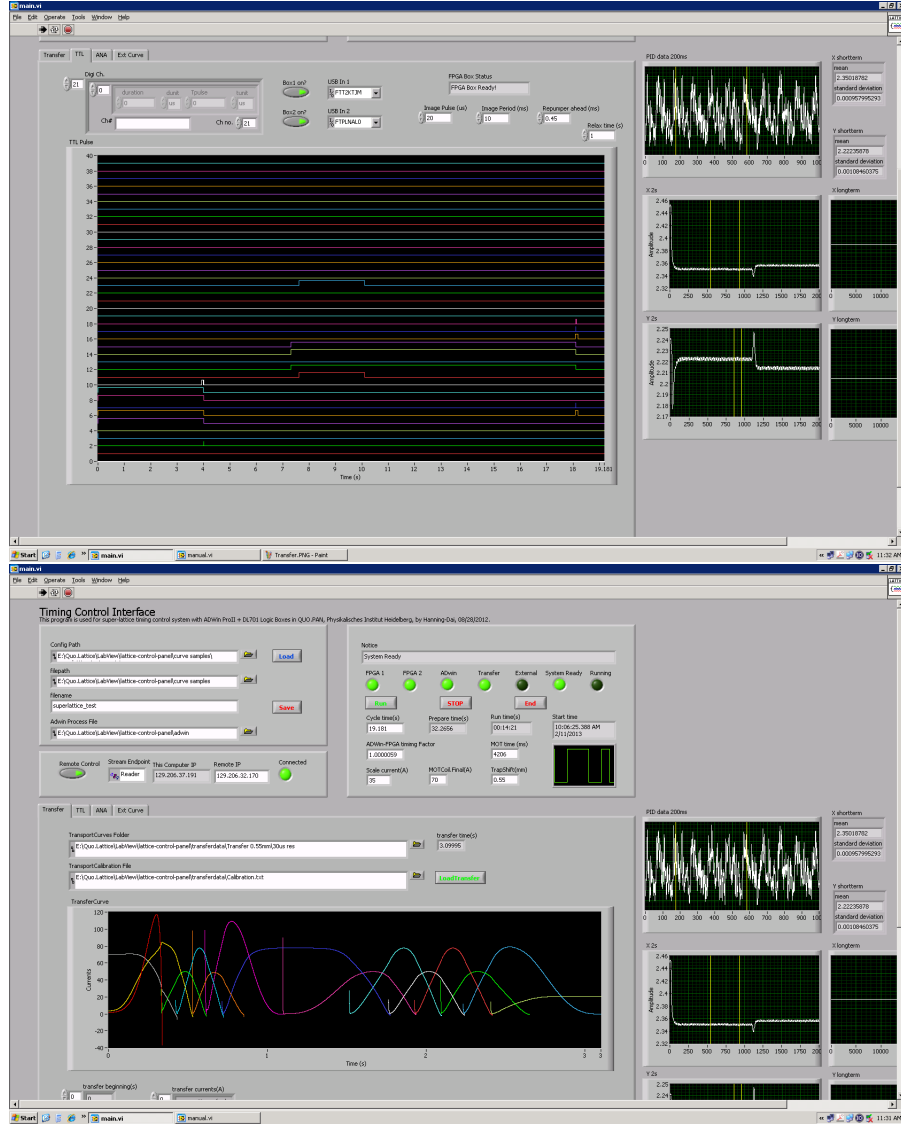


Figure 6.2.: Screenshots of the program which we use to control the system showing TTL and analog sequences controlling the various lasers and coil currents. The timeline in the upper screenshot is from the beginning of MOT production until the final BEC, the lower screenshot shows in particular the current ramps to perform the magnetic transport.

The start of each experiment sequence is similar to the one in section 3.1, and can be seen in detail in fig. 6.2 which is a standard sequence which we use to create a BEC

in the “crossed” dipole trap. We start out by creating a DMOT within 4 seconds and 6ms Molasses cooling of normally $5.9 \cdot 10^8 \pm 2.1 \cdot 10^7$ atoms and a temperature of about $20\mu K$. We pump them into the $|F = 1, m_f = -1\rangle$ state using a σ^- pump for 0.9ms (for more details see section 6.4), increasing a bias field within 15ms and transferring them to a magnetic trap for the transport within 30ms. For the transport we further compress the cloud within 300ms and normally have an atom number of $5 \cdot 10^8$ at $125\mu K$ and a density of $9 \cdot 10^{10} cm^{-3}$. Within 3.3sec we transport the atoms along the L shaped magnetic transport through the differential pumping section into the second glass cell which we will discuss in more detail in section 6.3. After the transfer we normally end up with $3.83 \cdot 10^8 \pm 0.21 \cdot 10^8$ atoms at $(125 \pm 16)\mu K$ in x and $(113 \pm 20)\mu K$ in y direction. We first evaporatively cool and compress the atoms in the magnetic trap down to $(22 \pm 5)\mu K$ in x and $(22 \pm 6)\mu K$ in y direction and $(3.77 \pm 0.05) \cdot 10^7$ atoms using a RF ramp from 15MHz to 3.75MHz in 2 sec, before we ramp down the dipole beam from 5.5W to 0.8W with an exponential constant of 800ms. We then perform a transition to the dipole traps and a magnetic gradient field which just compensates earth’s gravity at whose end we normally have $(1.03 \pm 0.03) \cdot 10^7$ atoms. We further cool them while ramping down the magnetic trap down to 0.4A (3G/cm) to create our pure BEC of up to $8 \cdot 10^4 \pm 4\%$ atoms. From here we can proceed to load the BEC into the 2D-pancake beams within 250ms at 150mW for each beam.

6.3. Magnetic Transfer

By trapping atoms in the weak-field¹ seeking $|F = 1, m_f = -1\rangle$ state using Anti-Helmholtz configured coils one can transport those atoms by two ways: either one moves the individual coils using precise low-noise motors or one assembles actually multiple Anti-Helmholtz coils in two layers which are shifted by the coil radius between each other and calculates the necessary currents to move the trap minimum along such a configuration [26, 53, 50]. This is basically a moving magnetic atom trap and we can calculate the maximally trapable atoms depending on their energy (and thus temperature) from:

$$E_{pot} = -g_F m_F \mu_B |\vec{B}| \quad (6.1)$$

where μ_B is the Bohr magneton and g_F is given in [69] and assumes for $F=1$:

$$g_F \simeq g_J \frac{F(F+1) - J(I+1) + J(J+1)}{2F(F+1)} \implies g_F = -1/2 \quad (6.2)$$

Another two important aspects one has to consider for the transportation is that the magnetic field should not change too fast otherwise one will loose atoms due to Majorana spin-flips[52, 26, 53]:

$$\mathbf{v} \cdot \nabla \left(\frac{\mathbf{B}}{\|\mathbf{B}\|} \right) \ll \omega_L \quad (6.3)$$

¹It is not possible to construct a trap for strong-field seeking states[17].

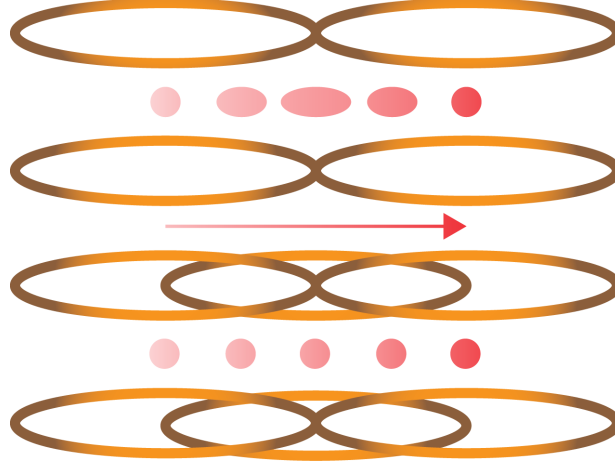


Figure 6.3.: The aspect ratio can be maintained during one transport section (center to center of one coil pair of the same level) if an additional coil is placed in the middle of two coils just above or below the track. Without the additional layer of interlocking coils the atom-cloud would deform and heat up during the transport. This type of track can be extended by adding more coils accordingly.

with $\omega_L = |gm_F\mu_B/\hbar||\mathbf{B}|$ being the Larmor frequency. The aspect ratio of the magnetic field gradient, determined by the Maxwell-equation $\nabla \cdot \mathbf{B} = 0$, should stay constant during transport to avoid heating. While the latter would be most likely easier to maintain using a linear motor, such a design might bring other stability problems: by having to maintain the stability of the transporting motor which would also have to pull the cabling and cooling tubes. Vibrations due to mechanical moving parts would have to be carefully compensated and it might be hard to consider the forces of bending cables/cooling tubes. We decided for the solution using multiple coils as in [26] which uses the already described interlocking coils in two layers which can also maintain a fixed aspect ratio of the gradient during transport. For arbitrary coil shapes one can use Biot Savart's law:

$$B = \frac{\mu}{4\pi} I \int_C \frac{dl \times r}{|r|^3} \quad (6.4)$$

which in case of round coils can be approximated using elliptic integrals [50, 40] to speed up the calculation time. Using cylindrical coordinates (r, ϕ, z) , we can give the

component-wise B-fields by:

$$B_z(r, z) = \frac{\mu I}{2\pi} \frac{1}{\sqrt{(R+r)^2 + z^2}} \left(K(k) + \frac{R^2 - r^2 - z^2}{(R-r)^2 + z^2} E(k) \right) \quad (6.5)$$

$$B_r(r, z) = \frac{\mu I}{2\pi} \frac{1}{r\sqrt{(R+r)^2 + z^2}} \left(-K(k) + \frac{R^2 + r^2 + z^2}{(R-r)^2 + z^2} E(k) \right) \quad (6.6)$$

$$k^2 = \frac{4Rr}{(R+r)^2 + z^2} \quad (6.7)$$

where I is the current and R the radius of a single coil. For the back transformation to cartesian coordinates one has to take care that for some quadrants in 3D the angular component switches sign, e.g. for the BEC Trap coils which lie separated to each other in the z-plane, x going to the right and y to the back:

$$B_{cart}(x, y, z) = \begin{pmatrix} B_r(\sqrt{x^2 + y^2}, z) \cdot \begin{cases} 0 & x = 0 \\ \text{sgn}(x) \cos[\arctan(\text{sgn}(x) \text{sgn}(y)y/x)] & \text{else} \end{cases} \\ B_r(\sqrt{x^2 + y^2}, z) \cdot \begin{cases} \text{sgn}(y) & x = 0 \\ \text{sgn}(y) \sin[\arctan(\text{sgn}(x) \text{sgn}(y)y/x)] & \text{else} \end{cases} \\ B_z(\sqrt{x^2 + y^2}, z) \end{pmatrix} \quad (6.8)$$

By choosing the trapping gradient strength in z-direction (opposite direction of the gravity vector) one can set up a minimization algorithm for the three currents which are needed to transport an atom along a set of coils as depicted in fig. 6.3. By choosing a gradient in z (up) direction, constraining the aspect ratio A to a fixed value during transport we will, together with the Maxwell equation, end up with a fixed shape (fixed gradients in x,y,z yielding a fixed potential shape).

$$B(I_1, I_2, I_3, x, y, z) = B_1(I_1, x, y, z) + B_2(I_2, x, y, z) + B_3(I_3, x, y, z) \quad (6.9)$$

$$\frac{\partial B_z}{\partial z} = - \left(\frac{\partial B_x}{\partial x} + \frac{\partial B_y}{\partial y} \right) \quad (6.10)$$

$$A = \frac{\partial B_y}{\partial y} \bigg/ \frac{\partial B_x}{\partial x} \quad (6.11)$$

For the first MOT coil we need to provide another push coil, directed along the axial movement direction to provide a smooth transition from the original aspect ratio of the MOT (roughly 1) to the new one maintained during the transport as well as compensating for the changed geometry of coil-radii. The minimization algorithm yields the currents which are required to trap the atoms at a certain position. By tracking our geometrical layout in a simulation it is possible to map these with a smooth acceleration curve to time-current pairs. In the experiment we use three power supply boxes developed at the Elektronische Werkstatt des Physikalischen Instituts (see appendix B) to drive the individual coils. The power boxes themselves use IGBTs that can control the current flow using a PI control loop with an external reference given by our AdWin realtime system. The AdWin system is slaved to one of two Logic Boxes which provides

the main clock for the second logic box as well as the trigger to start the AdWin process. One has to take care that there is a slight mismatch of the clock speed of the AdWin and the logic box and thus one has to introduce a small scaling factor in the main LabView program which controls the hardware. The IGBT power supply boxes themselves draw their power from an ESS 30V/500A power supply which can cover the total power requirement. Before we upload the calculated time-current pairs curves to the AdWin memory we further process these pairs using a .dll written in C++ as LabView proved inefficient for this task: we analyze the time sequence and only pass on the data of curves which are to be non-zero at a given time. We sort this data in ascending order of coil number and as there are always only consecutive coils in use it is sufficient to have a block of start- and end-coil identifiers for the memory blocksize. Only when a coil either enters or leaves the start-end block we need to adjust the block identifier. For this case we have one further block which has the $n - th$ process execution number written in at which we will have to switch to the next start-end block, which is equivalent to time due to the fixed process execution intervals. This approach of index-arrays has to be taken because unlike C++ there are no pointers available in the AdBasic programming language. Using this scheme we can save about 90% RAM and it should be the fastest possible way to process the output on the AdWin system later on. The $3\mu s$ achievable process-cycle time is very good considering it is running as realtime-software and not FPGA code. During one execution of this process the AdWin will first output all arrays to keep output timing synchronous with the process start which in term is synchronized with an internal clock. Coming next we only process the necessary updates to those arrays which could take a few cycles more or less depending on data amounts and if-branching. The output analog signals are encoded in 16 bit resolution from -10 to +10V of which we can only use the positive range; small negative values are used to pull down the IGBTs for faster closing and prevention of small leakage currents. The whole assembly is being secured by a standalone security system which measures temperatures, water flow (for the cooling) and voltage drops. In case of emergency this box can immediately deactivate the main powersupply by its own interlock, originally it would also switch off a chiller but since the move to a new building we use a magnetic valve to control the in-house watersupply which is now being used for cooling. Furthermore we only switch off the watersupply if the system is switched off completely now and would keep the water running in case the box switches off the currents due to overload because in this case cooling might actually be critical to avoid overheating damage. A schematic of the control dependency is shown in fig. 6.4; for more details we suggest reading[26, 53, 50].

6.4. Lasers

Our laser setup for the BEC experiments is of course similar to the one used in the quantum memory experiments and we only mention the used detunings for the MOT part: The Toptica DLX 110 is detuned by +190MHz from the $|5^2S_{1/2}F=2\rangle \rightarrow |5^2P_{3/2}F'=3\rangle$ transition, the derived cooler beam is detuned by a double-pass AOM by $-2 \times 104\text{MHz}$ yielding an effective -18MHz detuning. The Toptica DL100 is tuned to the

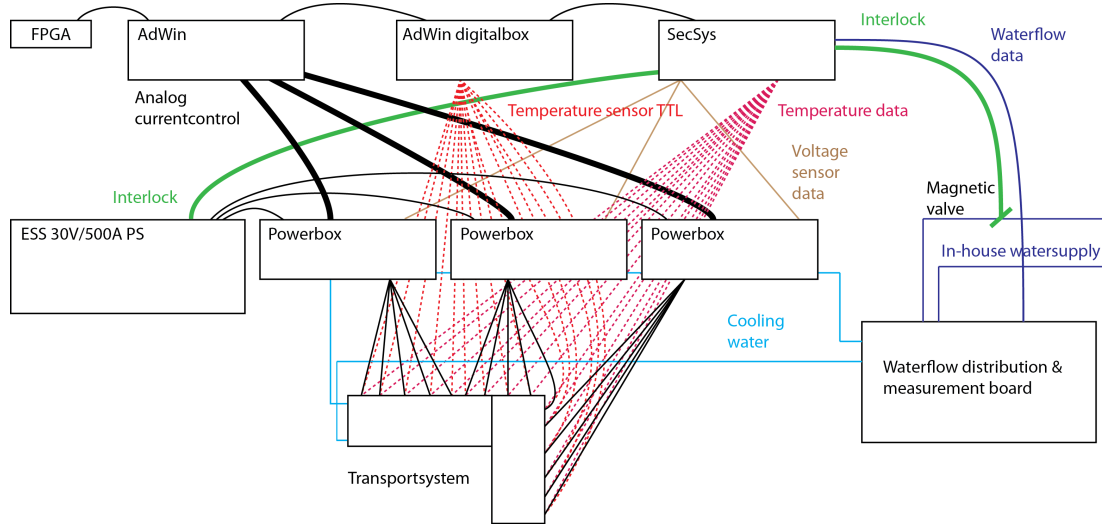


Figure 6.4.: Control chain and interlock security for the magnetic transport: The main trigger for each experiment cycle is being generated from an FPGA “Logic Box” produced by the Elektronische Werkstatt des Physikalischen Instituts, which triggers the main process of an AdWin realtime system. The AdWin system outputs precomputed analog ramps which control the current output of the three powerboxes which have been built by the Elektronische Werkstatt as well. The powerboxes themselves each draw the necessary current from an ESS 30V/500A powersupply. The whole system is being monitored by an individual securitybox (also built by the Elektronische Werkstatt) which checks the voltage drops, waterflow and temperature of the system and in case of errors can switch off both the main powersupply. Since the move into the new lab we replaced a chiller with in-house watercooling and changed the respective interlock on the security box to turn off the power of a magnetic valve when the box is switched off.

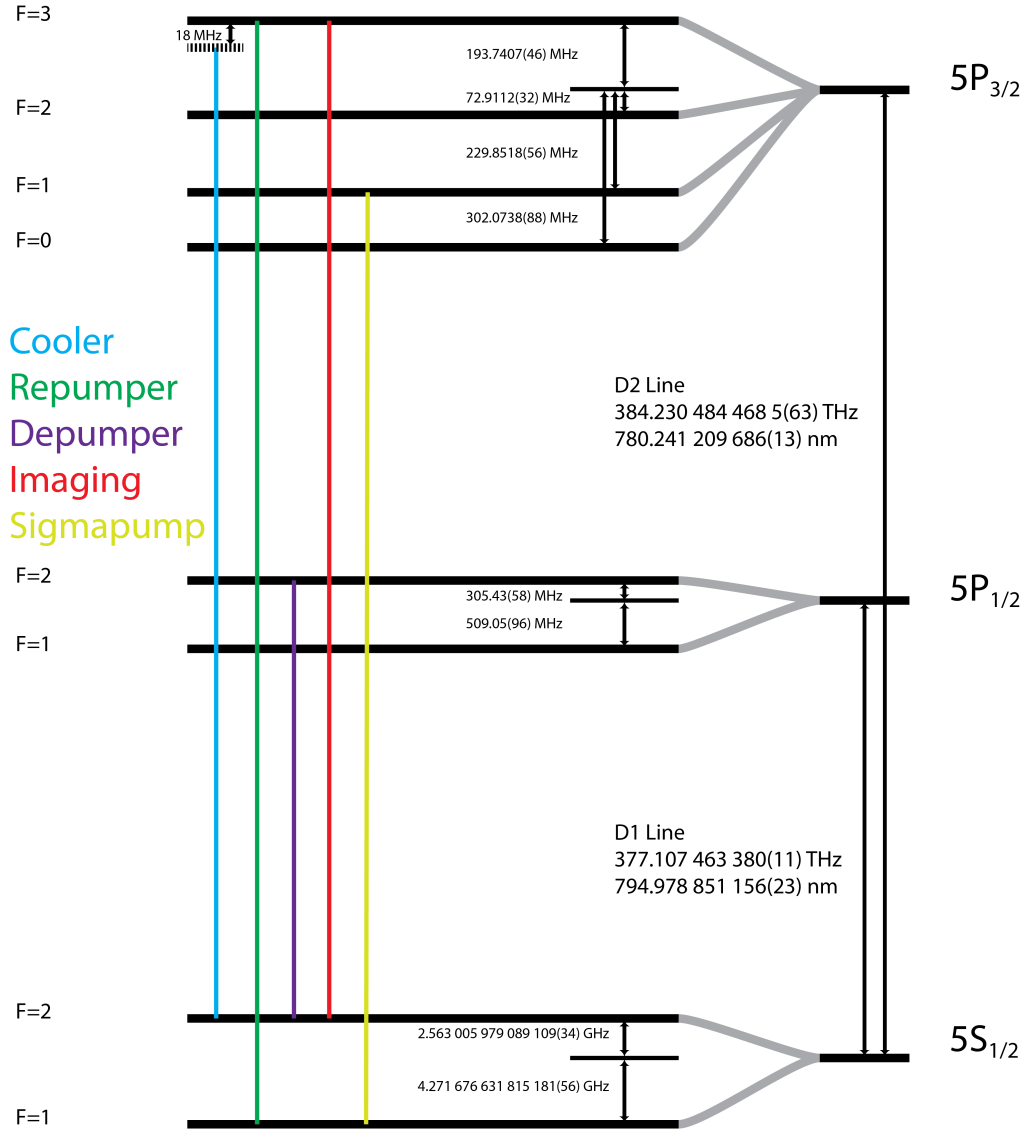


Figure 6.5.: Transitions used for the BEC/lattice experiments

$|5^2S_{1/2}F=1\rangle \rightarrow |5^2P_{3/2}F'=1-2\text{crossover}\rangle$, we tune it by +78MHz for the $\rightarrow |F'=2\rangle$ repumping and -78MHz for the $\rightarrow |F'=1\rangle$ σ pump. A homebuilt depumping laser is tuned to the $|5^2S_{1/2}F=1\rangle \rightarrow |5^2P_{1/2}F'=2\rangle$ transition. We have set the imaging beam to the $|5^2S_{1/2}F=2\rangle \rightarrow |5^2P_{3/2}F'=3\rangle$ transition and use a PBS to feed it either to the side or backport of the glasscell to be able to take pictures either from the side or the front of the ensemble. Finally we use a sigma pump set to $|5^2S_{1/2}F=1\rangle \rightarrow |5^2P_{3/2}F'=1\rangle$ to pump all atoms in the MOT into the weak-field seeking $|5^2S_{1/2}F=1m_F=1\rangle$ state which is required to make the atomic cloud follow the magnetic transport.

For the BEC dipole trap we have an IPG 1070nm fiber laser (55W), an NP photonics 1534nm fiber laser (5W) for a long 2D-grid lattice which is being power stabilized using a PI loop. Furthermore we use the Sirah Matisse, this time set to 767nm for both a pancake lattice (used for 2D confinement) and the short grid lattice. We typically reach 2.5 – 2.7W for 12W pumping power where the range is determined by a tradeoff of output power VS long term frequency stability chosen by a birefringent filter in the laser cavity. When we optimized the power using the birefringent filter we often observed that the plateau of our desired wavelength shortened which will also shorten the overall time during which the laser can be locked to this specific plateau (as it drifts to an edge over time).

We lock the 1534nm and 767nm lasers to each other to form a stable superlattice by shining the 1534nm through a PPLN frequency doubling crystal and overlapping the resulting beam with the normal 767nm beam on an ultrafast photodiode[10, 78]. Using a DP locking card² we can lock the resulting beating signal to each other with an added offset of $\sim 3\text{GHz}$. While we could keep the linewidth stability of the Matisse normally around 50kHz when we use the external PDH cavity there still was a drift of about 1 – 100MHz/h as mentioned in section 3.2. As this drift is undesirable for long term stability of optical lattices we modified the PDH cavity to work with an additional reference beam whose beating signal can be fed to a PI plugin to the Matisse via an NI card. The lattice is oriented upright, facing the front of the glass cell, in this way it is possible to exploit gravity, e.g. in the upcoming Bloch-Oscillation induced transport experiment.

6.5. High resolution Imaging

6.5.1. Design with simulated aberrations and compensations

To analyze quantum systems on an optical lattice it would be of advantage to have in-situ observability, ideally resolving individual atoms/lattice sites as in[67]. To achieve such a high resolution is however very challenging and demanding on the involved parts of the setup and require a very precise alignment to perform as desired. We set out with a Zemax-simulation of the point spread function of a point source coinciding with the atoms position, passing through a glass plate with the physical properties of our glass cell, a custom designed glass-compensator, an f=20mm lens of NA=0.54 for the

²See appendix D

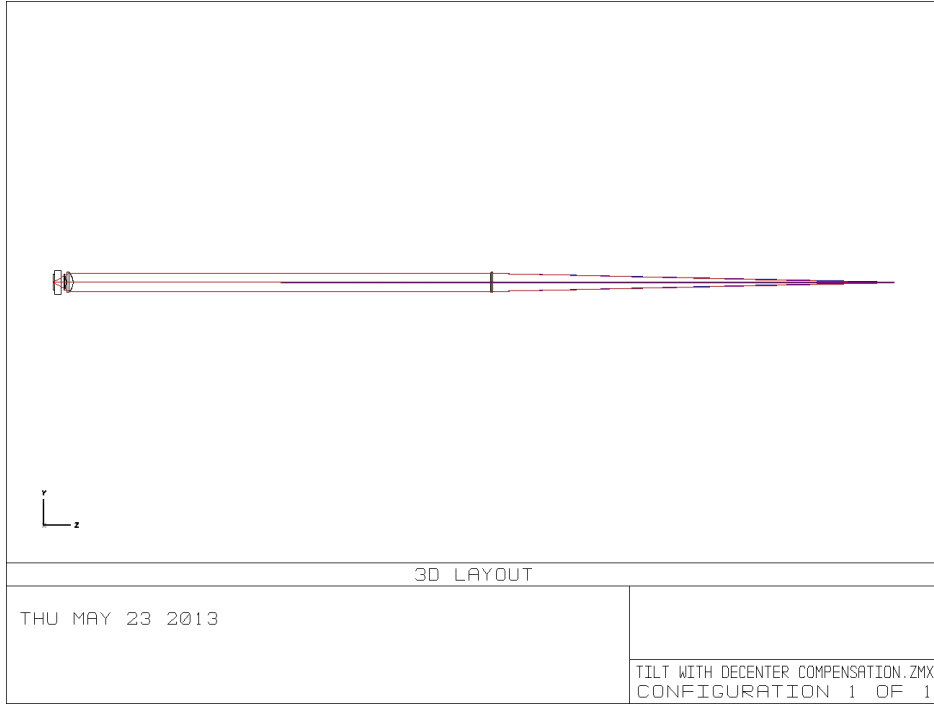


Figure 6.6.: Side-view of the high resolution imaging simulation, compensator and high resolution lens to the very left, 500mm lens at the center.

high resolution and the final imaging lens ($f=500\text{mm}$). The NA for the total system is simulated as 0.56 in Zemax.

A side-view of the simulated setup can be seen in fig. 6.6 taken from Zemax. The glass-compensator is made of N-SF1 and custom designed by LENS-Optics to compensate the wavefront distortion imprinted from the glass-cell. As the manufacturer could not measure this distortion we had to rely on the available dimensions/material data to simulate the required compensator properties. Together with the 20mm lens we should be able to resolve structures of the size $0.77\mu\text{m}$ which we determined by the Rayleigh criterion.

The optimized distances of the optics obtained from Zemax are 3.39mm for the compensator to the glass cell, 1.301mm between compensator and 20mm lens, 520mm between the 20mm high-resolution and 500mm aspherical lens and finally 500mm to the CCD. The spot diagrams and cross sections seen in fig. 6.7 show that the theoretical signal to noise level determined by the ratio of the main signal peak to the first order diffraction peak should be $\gtrsim 50$ for the center. This is only true for perfect alignment however, and as one can imagine for such involved scales already slight misalignments can cause lots of trouble when one aims for a diffraction limited resolution. We performed some additional simulations to see if we could compensate for e.g. lens-tilt because we have only limited degrees of freedom on how each lens can be tuned in the assembly. The

6.5. High resolution Imaging

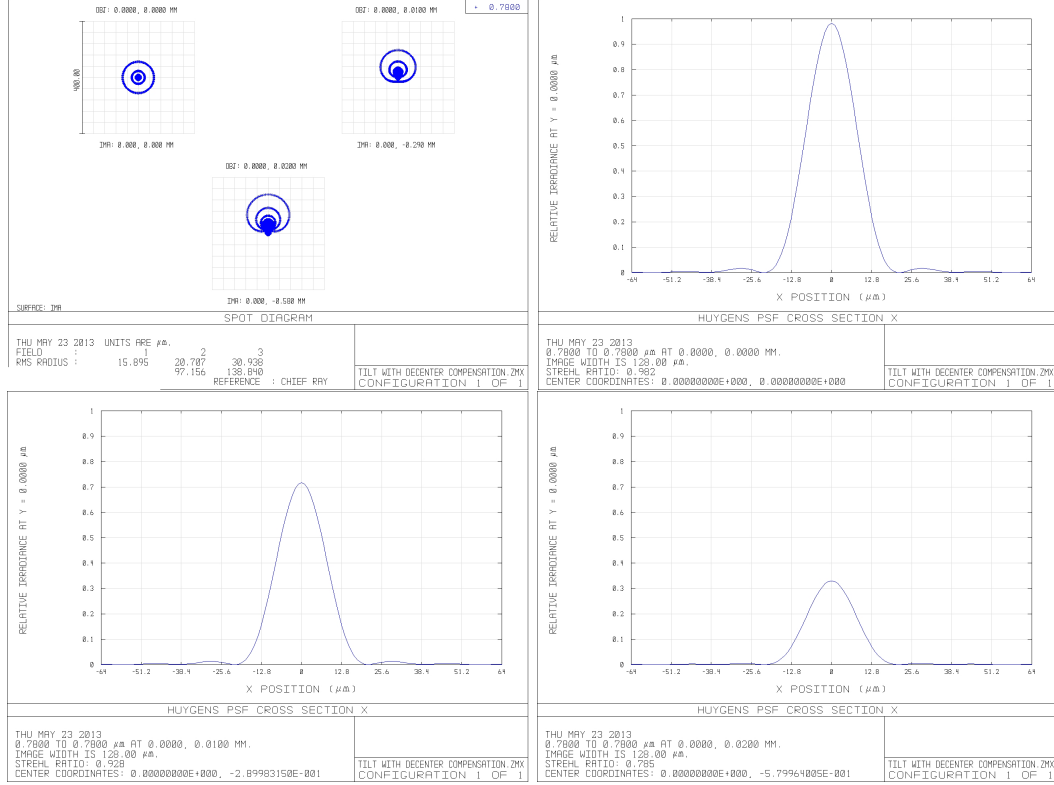


Figure 6.7.: Spot diagrams of the PSF for center, $-10\mu m$ and $-20\mu m$ off center with matching cross-sections showing the signal-noise ratio. The $-290\mu m$ and $-580\mu m$ spot position is due to the 29X magnification of the imaging system.

lens-tilt is indeed a very likely error as we can never be perfectly sure that the imaging assembly is exactly perpendicular to the glass-cell (we will describe the iterative procedure of alignment soon).

In fig. 6.8 we can see how an introduced PSF distortion due to tilt can be compensated through shifting the tilted lens. Of course the perfect imaging resolution can not be recovered but this approach is an acceptable compromise. One could argue that it might be better to find the main error in the given system and start by eliminating that, which in principle might be a good approach but raises other problems: to determine the main error which the PSF picks up from the system one has to fit several orders of Zernike polynomials which can represent the various aberrations like astigmatism, focal-, spherical aberration and so on. This process is neither fast nor easy to carry out so it is not possible to do in an “online” way with a fast response from adjusted tilts/shifts. Our goal is thus to first optimize the alignment as good as possible when we insert each part of the imaging system so that later on we will only have to compensate for very tiny degrees of tilt and other possible misalignments.

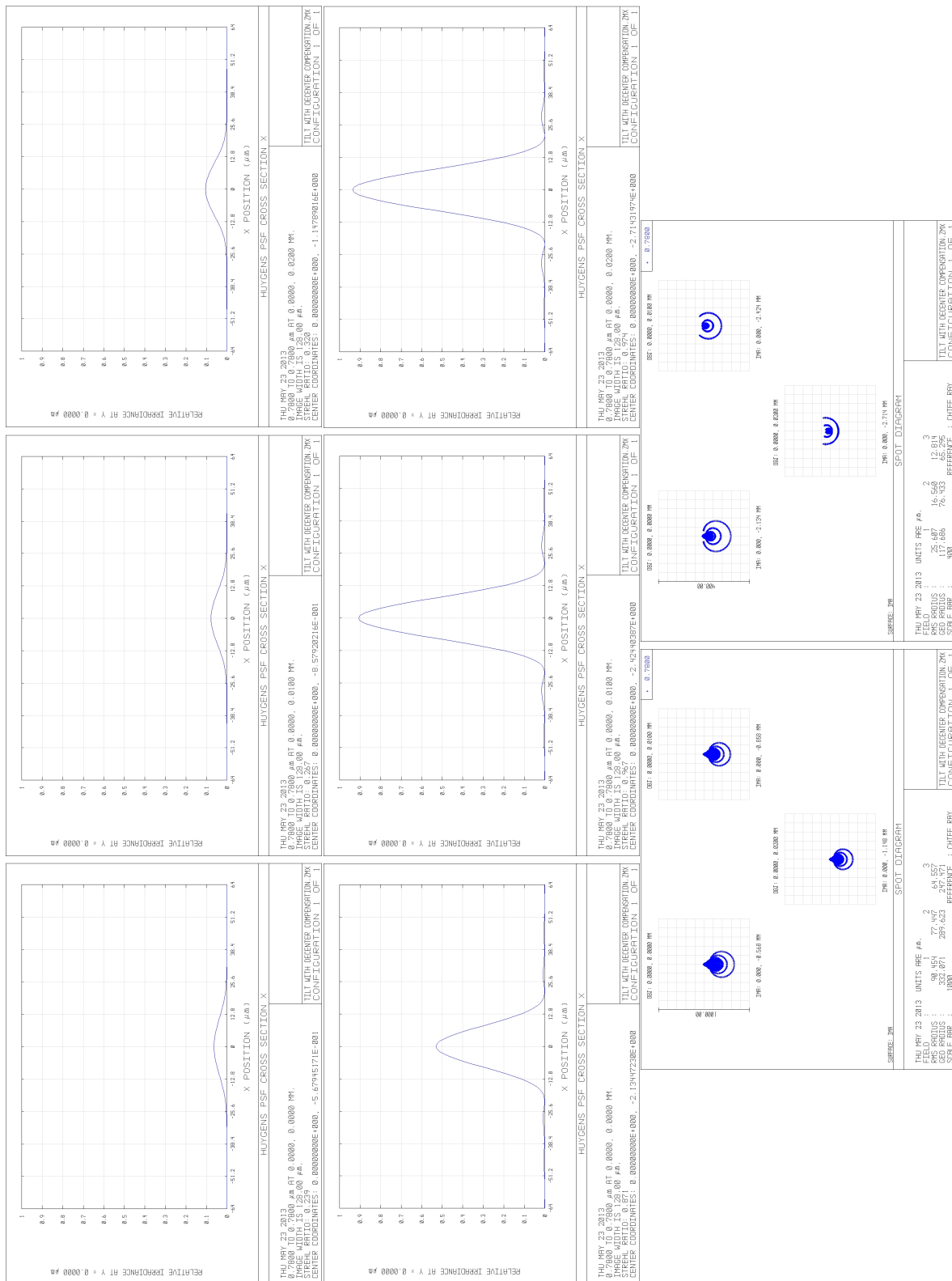


Figure 6.8.: Spot diagrams resulting from a tilt of the 20mm lens (upper row, bottom left) and the corrected spot diagram (center row, bottom right) when we introduce a compensating shift. Images taken again for center, $-10\mu m$ and $20\mu m$.

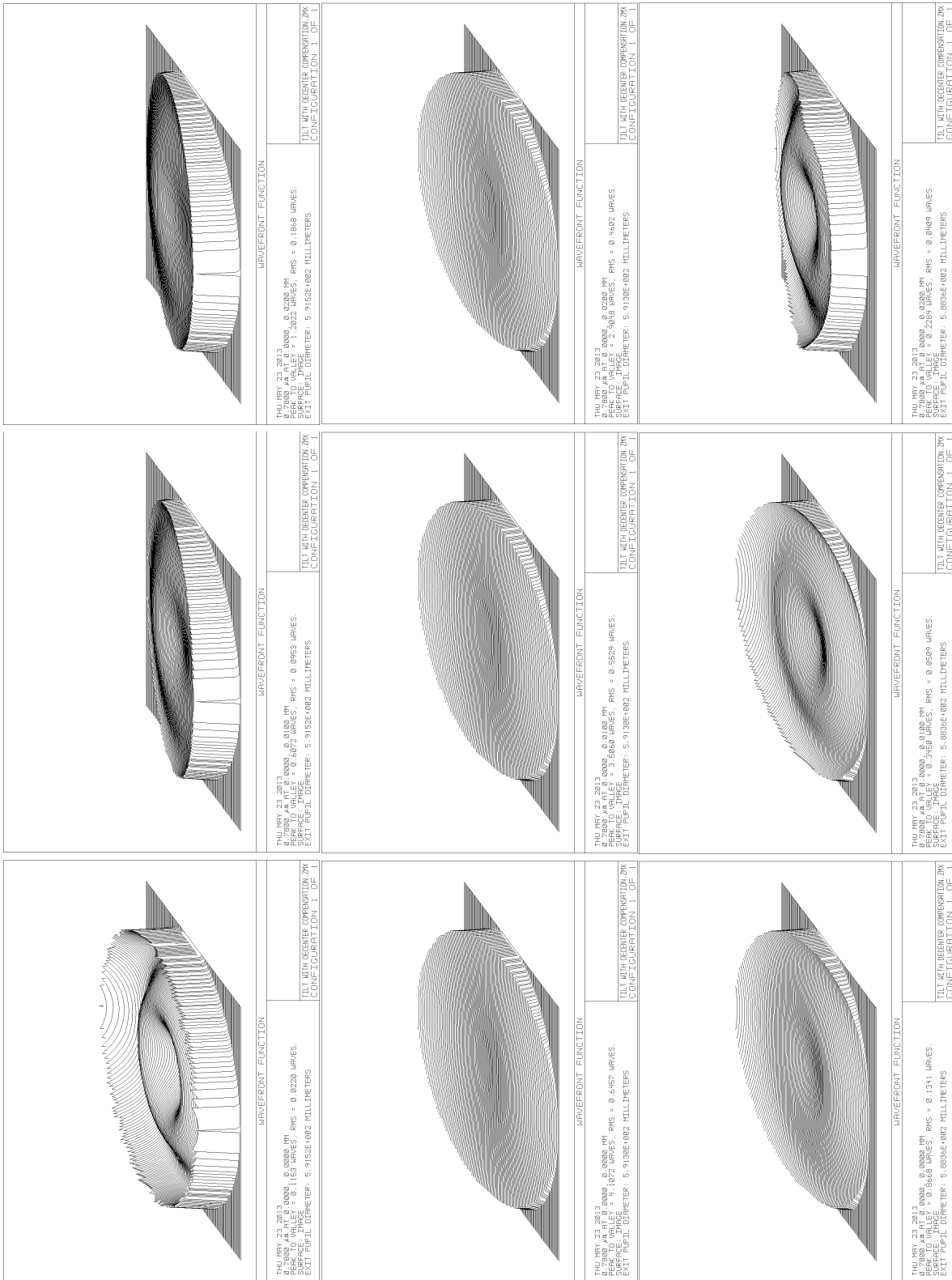


Figure 6.9.: Wavefronts of: First row: untilted system, second row: tilted system, third row: tilted system with compensating shift, positions are the same as in the previous image sets. images.

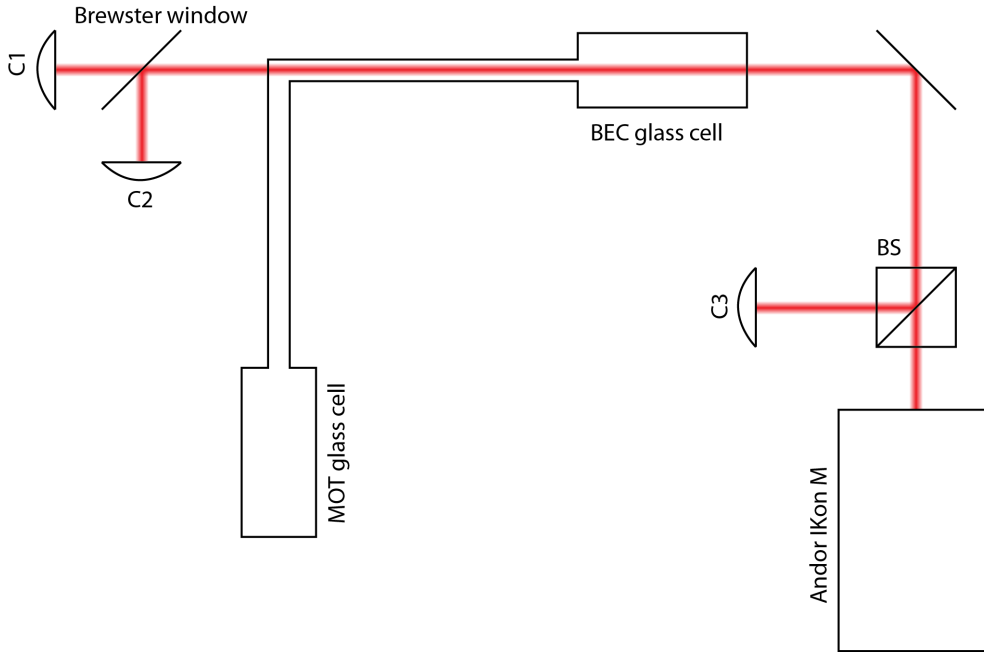


Figure 6.10.: Overview of the elements used in the alignment procedure as described in the text.

Another option would be to use a wavefront sensor combined with either a spatial light modulator (SLM) or a deformable mirror in a feedback loop to optimize the flatness of the wavefront. There are advantages and disadvantages to SLM and a deformable mirror: the SLM has discrete pixels with small gaps in between which might be problematic for the final smoothness and resolution which can be reached by the PSF but normally a SLM has a much higher resolution than a deformable mirror. A deformable mirror has the advantage of being one continuous steady surface but normally has much less actuators available than an SLM pixel matrix. We did not have access yet to any of such devices to make a test and cannot give a conclusive answer to their usefulness in our application, but in principle they should be a promising way to improve imaging systems. In related publications [15, 9] it was shown that great improvements can be achieved using such techniques.

6.5.2. Alignment procedure and performance

The alignment procedure of the imaging system in our system goes as follows: as our glass cell is attached to the vacuum tubes it is the main reference to which all other optics will have to be aligned to. The first step is to align the imaging beam from coupler 2 (C2 in fig. 6.10) perpendicular to the surface of the glass cell, by using the weak backreflection which is generated when it passes through the front face of the glass cell. In a first rough alignment we check that the beam hits the center of a small BEC

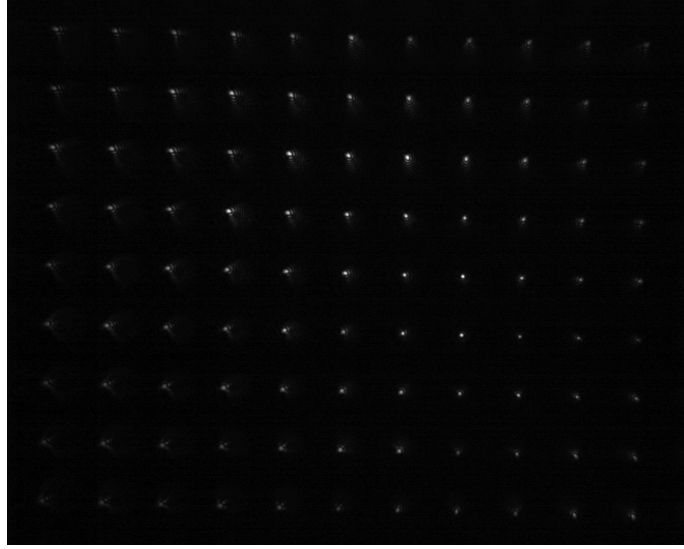


Figure 6.11.: Image of the precision target hole-grid.

and then iteratively overlap the backreflection with the original beam using a pinhole for increased precision. Once the backreflection is well aligned and the beam center still hits the BEC we can be sure that C2 is aligned correctly.

In the second step we shine in a second reference beam from coupler 3 (C3 in fig. 6.10) which is counterpropagating to the beams of C1 and C2. As this beam is only used for calibration, the incoupling beamsplitter sits on a flipable mount so that we can take it out of the system in an easy way. To optimize the alignment of beam C3 we couple its light back directly into the coupler of C2. In the next step we place in the 500mm lens in between the glass cell and the mirror and check its alignment by checking the back reflection to coupler C3. When we have aligned this lens we use a weak intensity light from coupler C2 to check if the Ikon M CCD sits at the focus and if the beam really goes through the center of the lens which can be analyzed from aberrations in the image. Finally we repeat the last step for the high resolution lens of the system until the backreflection matches well enough with the reference beam.

Now we can be sure that the remaining aberrations should mainly be due to defocusing and shift. Shifting the imaging system will also compensate for small remaining tilts as already discussed. Currently we are investigating a redesign of the lens mount combined with a high precision motorized translation stage, as seen in appendix C. Furthermore we replaced the Thorlabs aspherical $f=20\text{mm}$ lens with another version from Asphericon which shows a better performance (25-20 HPX-U). Test images obtained from a high-precision target using a hole-grid with holes of 600nm , equally spaced at $25\mu\text{m}$ are seen in fig. 6.11 and fig. 6.12 shows a best-case average of the obtainable resolution of $1.0\mu\text{m}$. The results are much easier reproducible when using the motorized mount and should lead to an improvement when we install the system back into the setup.

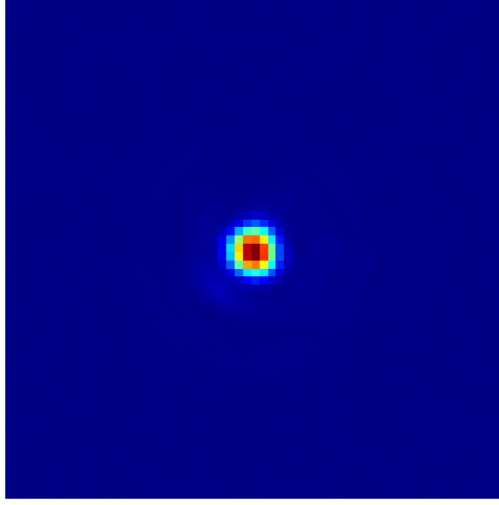


Figure 6.12.: Averaged image of the best case resolution for the precision target hole-grid.

6.6. Experiment preparation

In section 6.1 we already outlined the procedure and atom numbers/temperatures until the point of BEC creation. Regarding the BEC trap we measured its frequencies by using two ways: for the low frequencies of the x and y direction it is sufficient to give a kick to the atoms by suddenly increasing and decreasing the dipole potential and then observe the ensuing oscillations in real space, whereas for the high frequency in z direction one needs to modulate the potential with a small sinusoidal frequency on top of the actual trapping depth. If the applied frequency matches the trap frequency or is an integer multiple thereof one sees a strong loss of atoms[41]. Both can easily be achieved by modulating the reference signal from the AdWin system to the AOM driver which is responsible for the power of the dipole beam. As seen in fig. 6.13 we can obtain the frequency from the x and y direction by releasing the atomic cloud at several start times and measure the center of mass distribution after a short TOF. For x and y we obtain trap frequencies of $\omega_x = 2\pi \times 104.4\text{Hz}$ and $\omega_y = 2\pi \times 53.9\text{Hz}$. Whereas in fig. 6.14 we see the atomic loss generated at double eigenfrequency of the trap which corresponds then to $\omega_z = 2\pi \times 514\text{Hz}$.

Once we have created our BEC we have to load it into our pancake lattice to confine our atoms to an effective 2D system and/or want to apply our optical lattice beams for the experiments. An important aspect here is that we need to be sure that we load atoms to one layer of the pancake lattice. To verify this we scan the position of the lattice across the atoms by moving the mirror assembly on a high precision translation stage with a resolution of 25nm per step (although due to hysteresis it is not reverse direction retrievable). We then perform TOF images from the side of the atom cloud and check for interference patterns (as seen in fig. 6.15) which occur if two neighboring layers get

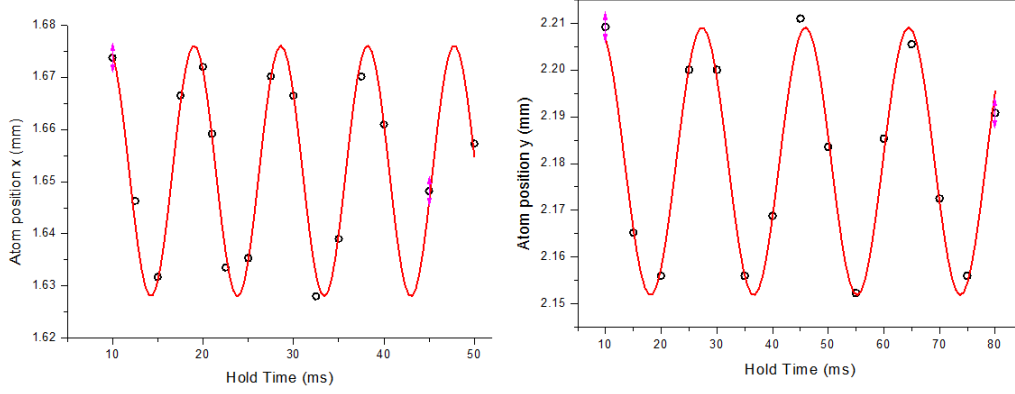


Figure 6.13.: Dipole trap frequency fits obtained from the real space oscillations, projected into TOF center of mass position when releasing atoms at different timings. Figure one showing x and figure two showing the y trap frequency.

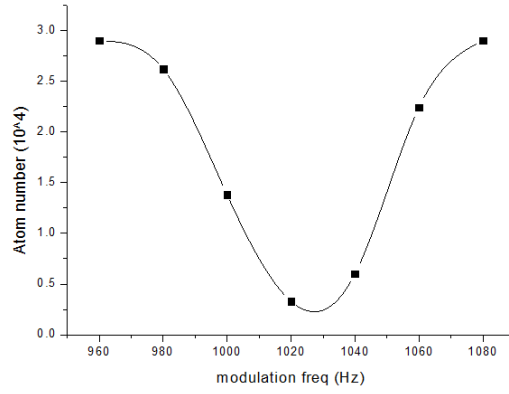


Figure 6.14.: Dipole trap frequency fit in z direction from the second harmonic of parametric excitation.

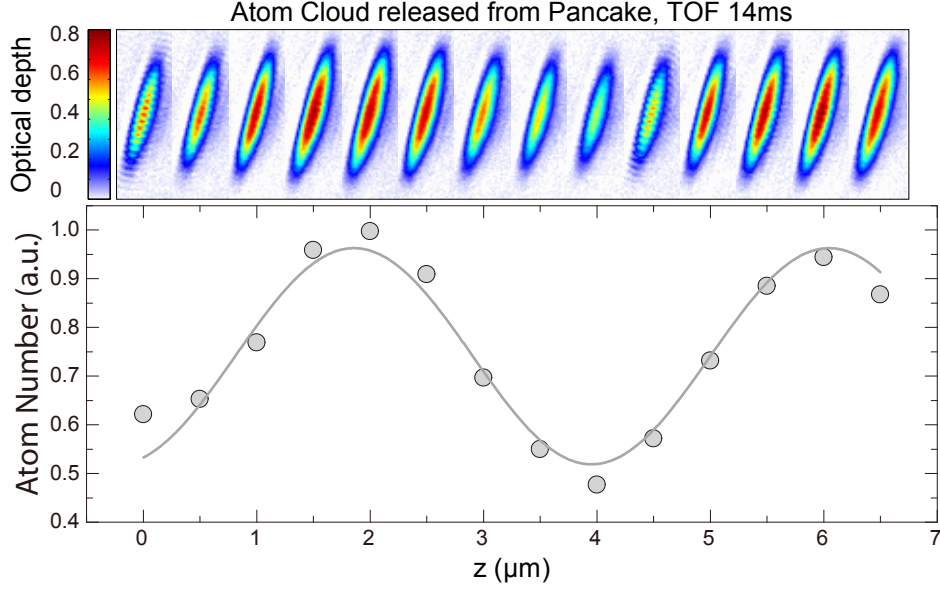


Figure 6.15.: TOF images of atom clouds imaged for different positions of our pancake lattice showing less interference and higher atom numbers if most atoms are filling only one layer [10].

populated. By optimizing both atom number and using the interference pattern as a guide it is possible to load almost all atoms to a single layer (larger than 95% as seen in fig. 6.15). We obtained the frequencies for the pancake beam in the same way as we already did for the other dipole trap. In fig. 6.16 we can see the projected center of mass after releasing the cloud at given times and an additional TOF of 4ms, where the atoms have initially been kicked for 1ms at a strength of $1/4W$. The respective trap frequencies obtained are $\omega_x = 2\pi \times 40.7\text{Hz}$ and $\omega_y = 2\pi \times 54.5\text{Hz}$. For the high frequency in fig. 6.17 we used the sinusoidal modulation around the second harmonic of the trap frequency which were at $\omega = 2\pi \times 4.212\text{kHz}$ in the old lab and $\omega = 2\pi \times 3.168\text{kHz}$ in the new lab.

To optimize the overlap of the 2D lattice with the atom cloud we followed a routine outlined in [23]: optimizing Kapitza-Dirac[42] diffraction patterns (especially the 1st diffracted part of an atom cloud VS the undiffracted portion) sequentially using the same settings of laser intensity and pulse length. By iterative alignment of the beams after comparison of the diffracted atom's fraction one can optimize towards the ideal overlap of beams and atoms. By using a short and weak enough power of the pulse we can ensure to stay just beneath the possible first maxima of atoms which can be transferred into the first diffraction order for the given combination of the two and then optimize the beam position towards a maximum amount of atoms in mentioned order. An illustrative image of Kapitza-Dirac scattering can be seen in fig. 6.18, for lattice optimization one would not use as many orders but it is very useful to determine the lattice tilt from the picture.

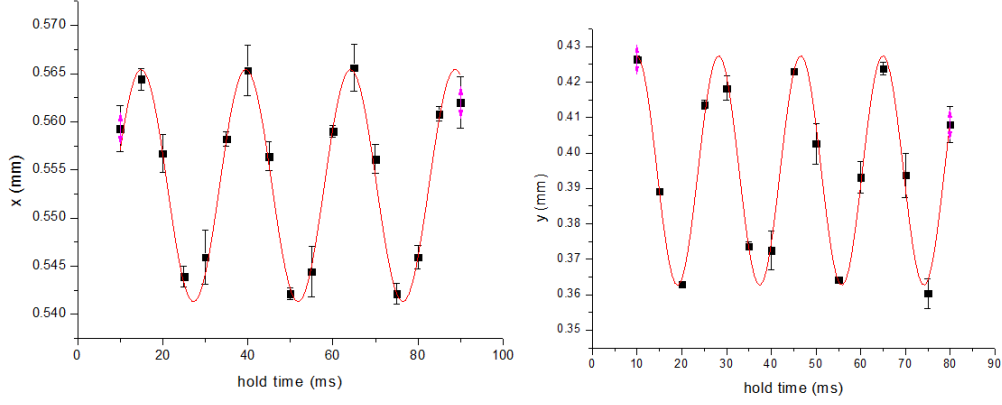


Figure 6.16.: Pancake trap frequency fits obtained from the real space oscillations, projected into TOF center of mass position when releasing atoms at different timings. Figure one showing x and figure two showing the y trap frequency.

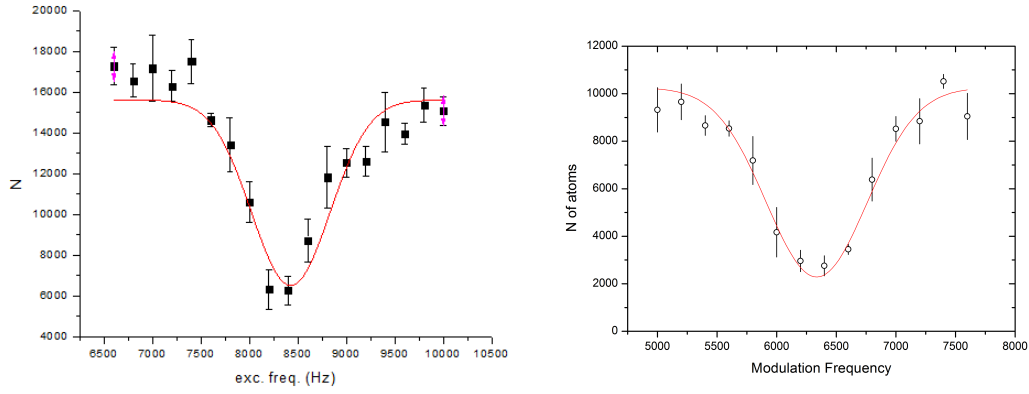


Figure 6.17.: Comparison of the pancake trap frequency in z direction in the old and the new lab, the difference can be attributed to the fact that we did not use a magnetic gradient field to levitate the atoms in the new measurement which would deliver a higher, probably almost same value. Modulation frequencies are around the second harmonic of the parametric excitation.

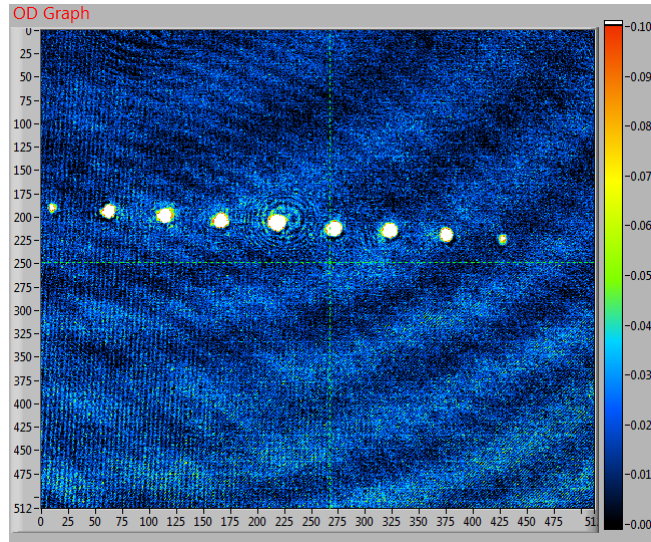


Figure 6.18.: 4th order Kapitza-Dirac scattering for illustration, normally only the 1st and 2nd order are being used for calibration as this high population in higher orders can only be achieved for very high pulse intensities and under normal circumstances only the low orders have a high enough signal/noise population ratio. One can, however, extract the lattice tilt much better with so many diffraction orders.

The Hamiltonian which describes the BEC population undergoing diffraction in a pulsed 1D lattice is given by:

$$H = -\frac{\hbar^2}{2m} \frac{\partial^2}{\partial z^2} + V_0(t) \cos(kz)^2 \quad (6.12)$$

which can be discretized for numerical differential equation solving by using an ansatz of $\psi(t) = \sum_n c_n(t) e^{i2nkz}$ and $n = 0, \pm 1, \pm 2, \dots$ with $c_n(0) = \delta_{n,0}$ and introducing dimensionless parameters [23]:

$$\alpha = (E_r^{(2)}/\hbar)\tau \quad (6.13)$$

$$\beta = (V_0/\hbar)\tau \quad (6.14)$$

$E_r^{(2)}$ being the two-photon recoil energy $((n\hbar k)^2/(2m))$ yielding the equation:

$$i \frac{dc_n(t)}{dt} = \frac{\alpha n^2}{\tau} c_n(t) + \frac{\beta}{4\tau} (c_{n-1}(t) + 2c_n(t) + c_{n+1}(t)) \quad (6.15)$$

Simplifications of this model can be given e.g. if the Raman-Nath criterion is satisfied:

$$T_{pulse} \ll T_{RN} \equiv \frac{\hbar}{\sqrt{U_0 E_L}} = \frac{T_{ho}}{\pi} \quad (6.16)$$

where $E_L = \hbar^2 k_L^2/(2M)$ is the lattice recoil energy and $T_{ho} = 2\pi/\omega_{ho}$ the harmonic oscillator period [38]) are given in [23] as:

$$P_n = J_n^2 \left(\frac{\beta}{2} \right) \quad (6.17)$$

the Population of the n th order after a pulse in the Raman-Nath regime, with J_n being the Bessel J functions of first kind and $\beta = (V_0/\hbar)\tau$ a measure of the area of the pulse [23]. By taking into account the square TTL pulse-profile present in most real world applications eq. (6.17) can be expanded to:

$$P_n = J_n^2 \left(\frac{\beta}{2} \text{sinc} \frac{\alpha}{2} \right) \quad (6.18)$$

with $\alpha = (E_r^{(2)}/\hbar)\tau$ being the pulse duration in units of 2-photon recoil time [23]. In general numerical solving of eq. (6.15) yields accurate results only for lower potential depths, for higher intensities it is better to numerically calculate the time evolution of a system using a Hamiltonian as in eq. (5.49). We take q as zero which is a well approximation for ultracold atoms, and the time evolution using N orders/bands is given by:

$$U(q, V, \Delta t) = \sum_{n=1}^{2N+1} e^{-\frac{i}{\hbar} \text{EVal}(H(q, V), n) \Delta t} |\text{EVec}(H(q, V), n)\rangle \langle \text{EVec}(H(q, V), n)| \quad (6.19)$$

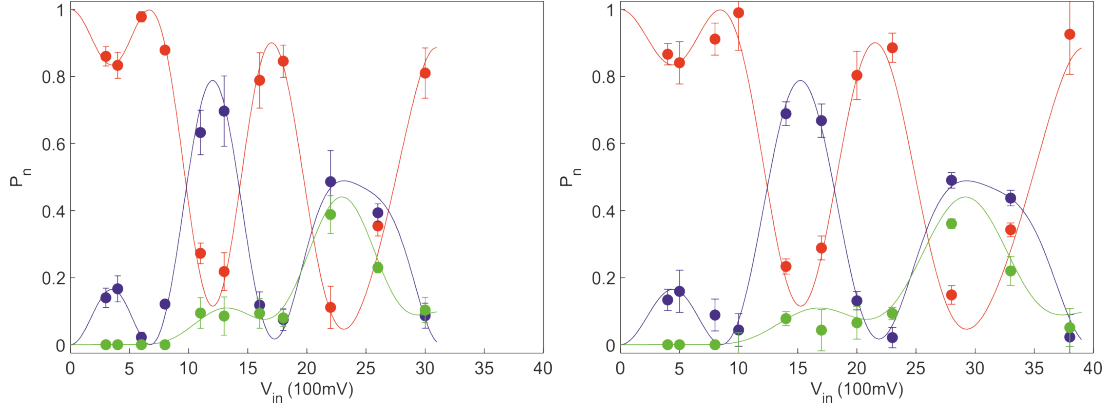


Figure 6.19.: KD scattering for a fixed pulse duration ($40\mu s$) with varying potential depth (767nm, units in E_r), experimental results with fitted curves to the Hamiltonian for the x and y lattice.

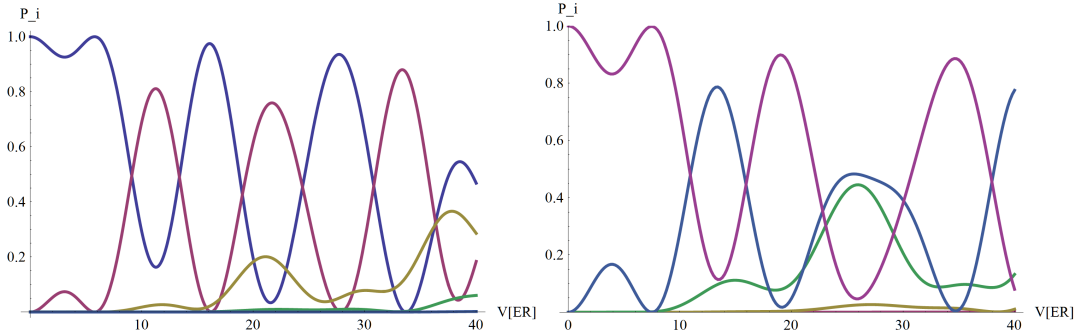


Figure 6.20.: Discrepancy between the two KD-scattering models, with the 2nd being the more accurate one as seen from data in fig. 6.19. Pulse length $40\mu s$, potential given in E_r for 767nm laser.

where E_{Val} and E_{Vec} yield the $n - th$ Eigenvalues/vectors of the supplied system. The initial state is simply given by a $2 \cdot N + 1$ zero-vector with a 1 at the $(N + 1) - th$ position. By stepping through time we can now evolve the initial system to the points in time and/or energy we want to evaluate. We compare experimental results for the calibration of the lattice depth with the fitted model of the time evolution ansatz in fig. 6.19, and the discrepancy between model eq. (6.15) and eq. (5.49) can be seen in fig. 6.20; the experimental results clearly show that only the latter model is suitable for higher pulse strengths, as seen in fig. 6.19.

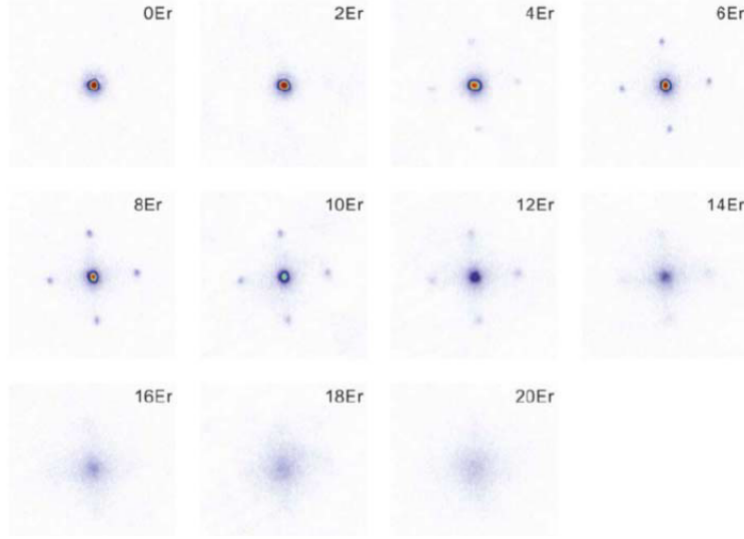


Figure 6.21.: TOF images showing the MI-transition when the lattice depth is increased[78].

6.7. Mott Insulator transition

Once we have set up and calibrated the lattice depth using the described methods we proceeded with a test of the Mott-Insulator transition in the 2D lattice. We start out with ~ 8000 atoms in our quasi-2D trap of $30\text{Hz} \times 60\text{Hz} \times 4.9\text{kHz}$ and use the 767nm laser for the short 2D lattice. We ramp the lattice depth using a smooth S-curve/sigmoid-curve with a length of 200ms , whereof 100ms are an exponential function with timeconstant 30ms , and the second part has timeconstant -30ms . In fig. 6.21 we can see the typical TOF images of the MI-transition when the lattice depth is increased. To verify the quality of the transition to the MI regime we analyzed the visibility of the interference fringes of the TOF images and compared it with the case of a linear ramp which is expected to perform worse. The visibility is defined by [24]:

$$V = \frac{N_a - N_b}{N_a + N_b} \quad (6.20)$$

where we define the regions for counting according to picture section 6.7, from [78]. In an ideal superfluid we would obtain $V = 1$ whereas an ideal Mott Insulator would show $V = 0$, intermediate values indicate imperfections of the transition to the MI state [27]. We compared the 200ms sigmoid curve with a 30 linear and a 30ms exponential ramp and held the atoms for different times before releasing them for a 12ms TOF image. Results are shown in section 6.7 and clearly show that the s-curve performs superior compared to both linear and exponential ramps. Each datapoint requires taking at least 20 shots and using image-post processing to remove background noise, the atom number fluctuation does not contribute to a fluctuation of the visibility however and it takes

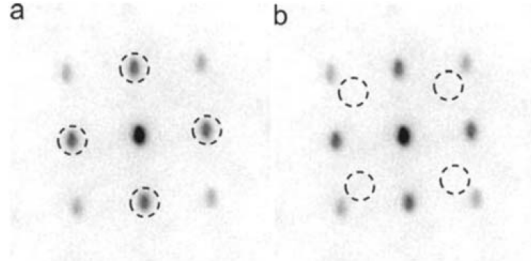


Figure 6.22.: Regions which are being used to define the Mott-insulator visibility.

further studies to obtain the primary source of the still quite large error bars[78].

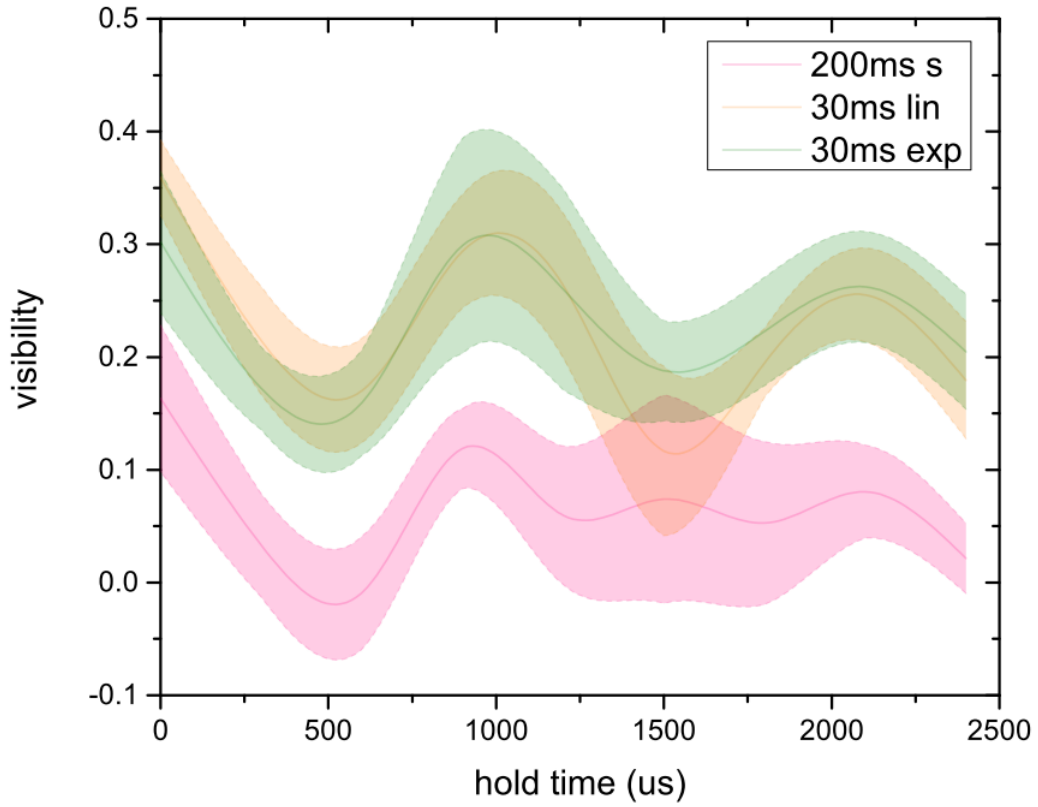


Figure 6.23.: Visibility of the MI-transition for different ramping curves and holding times.

To determine the required lattice depth for the onset of the MI-phase transition we ramp the lattice to different values and again measure the visibility; the ramp curve is a combination of a 10ms linear ramp to $2E_r$ with an added 200ms s-curve as before. In

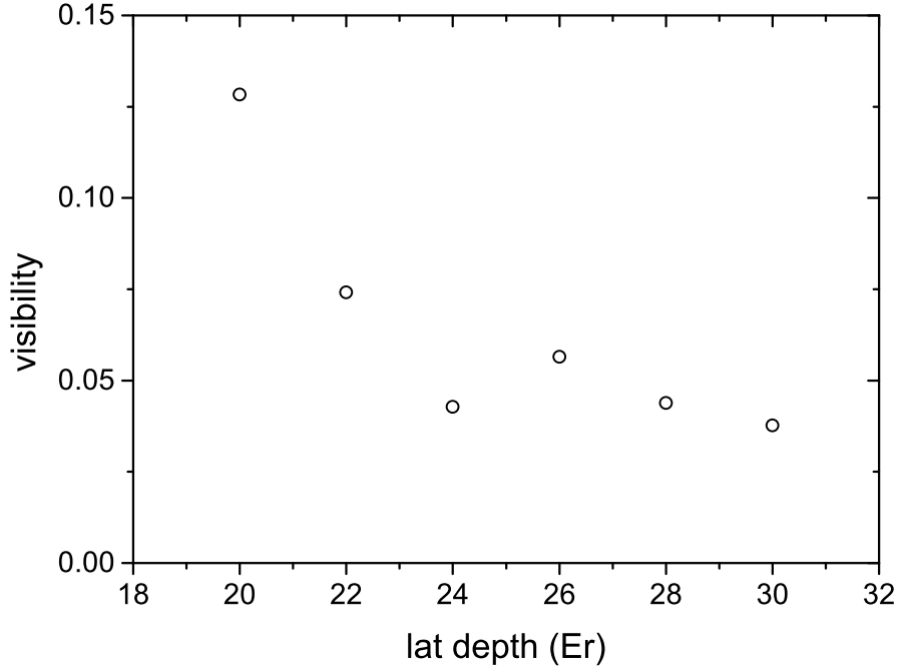


Figure 6.24.: Mott Insulator visibility VS final potential ramp depth.

fig. 6.24 we see that beginning from $20E_r$ the visibility decreases rapidly and beyond $24E_r$ settles around a noisy value close to zero. According to this data we choose $26E_r$ as final ramp depth in order to really reach the MI phase while keeping the photon scattering induced heat low[78]. We now perform a series of images to scan the evolution from the superfluid phase to the MI-phase using adiabatic parameters: 30ms linear ramp from 0 to $0.4E_r$ being followed by a 160ms s-curve from $0.4E_r$ to $26E_r$ [78]. The pictures are taken by using the same analog curve each time but switching off the TTL signal at the desired point during the ramp which will immediately switch off the lasers and thus release the cloud for TOF. In fig. 6.25 we see the evolution of the visibility from $5E_r$ to $26E_r$ with a pronounced kink around $17.5E_r$ which is interpreted as a sign of redistribution in the shell structure of the MI density [24]. Even though the total visibility is offset from day to day measurements the kink stays reproducible at the same potential height.

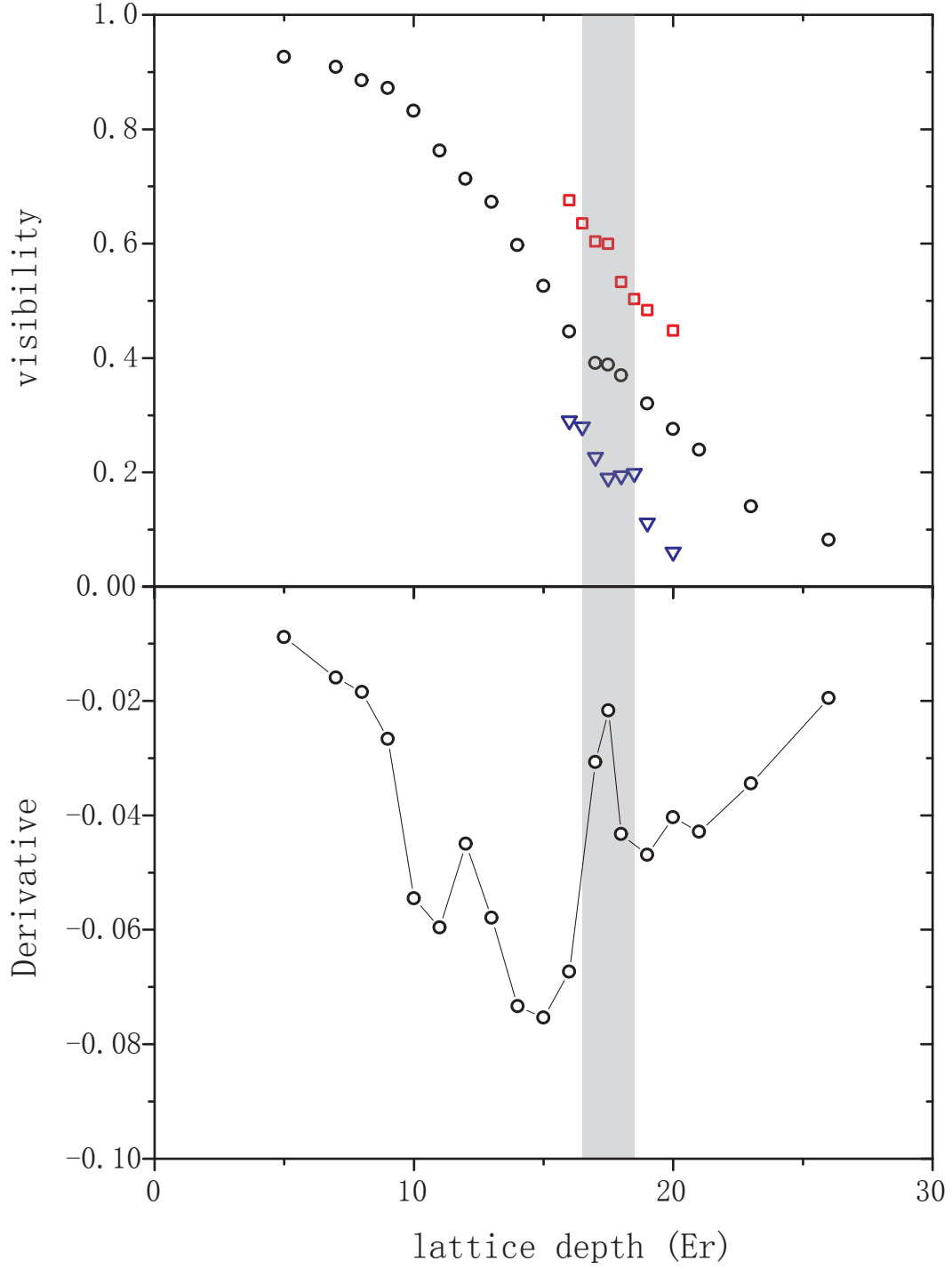


Figure 6.25.: Visibility evolution from SF to MI phase, red and blue datapoints taken on different days show different visibilities but the kink indicating redistribution in the shell structure of the MI density stays at the same position.

7. Transport on a lattice due to 2D Bloch oscillations

7.1. Motivation and theory

Bloch oscillations and associated effects like Zener tunneling go a long way back to the original papers by Bloch[8] and Zener [80] studying the properties of a perfect crystal under the influence of an external force/field in solid state physics. Theoretically the constant force of a weak electric field on electrons would not lead to conduction in an ideal crystal but rather to an oscillatory movement as the electrons traverse the Brillouin-zone at 0K[39].

Under normal circumstances however this effect is not visible due to defects in most solid states leading to fast decoherence. They have been observed indirectly in semiconductors via its terahertz radiation emitted from the oscillating electrons e.g. [13], directly in two dimensions in photonic crystals [73], induced transport by Super-Bloch Oscillations in one dimension [33], breathing modes of thermal atoms [2] and precision measurements of gravity [63]. Further suggestions which use Bloch-Oscillations include e.g. “matter-lasers” and matter-beamsplitters [72] and possible applications for quantum computing.

In [81] Zhang and Liu point out that unlike in e.g. [33] a two dimensional system would not require the modulation of the force to induce long distance transport across the lattice. Zhang and Liu point out the interesting possibilities of more complex lattice structures using e.g. three beams to form a triangular lattice whereas we will use a normal grid structure in regard of upcoming planned experiments. In general one could simulate almost arbitrary systems using ultracold atoms in two dimensions due to the large tunability of optical lattices and geometries. Zhang and Liu describe the movement of a wavefunction¹ by the semiclassical approximation[39, 81]:

$$\dot{\mathbf{r}} = \frac{1}{\hbar} \nabla_{\mathbf{k}} E^n(\mathbf{k}) \quad (7.1)$$

and considering an external force in integral form:

$$\mathbf{r}(T) - \mathbf{r}(0) = \frac{1}{\hbar} \int_0^T dt \nabla E(\mathbf{k}_0 + \mathbf{F}/\hbar \cdot t) \quad (7.2)$$

¹Even though we use ultracold atoms the same applies for other systems e.g. as in the mentioned photonic crystals and thus we adopt the more general term of wavefunction.

here E^n is the dispersion relation for the energy bands and we drop the n-th index notation in eq. (7.2) as we will only consider atoms in the tight-binding regime where only one energy band exists. In the one-dimensional case and with constant force the atoms will continually travel across the brillouin zone where at the border their k-vector will flip to the opposite side. As for a normal balanced symmetrical lattice the brillouin zone is symmetric as well there will be no net gain in neither momentum nor center of mass movement which we can briefly summarize (as done in [81]):

$$k = k + nG \quad (7.3)$$

$$T = G/F \quad (7.4)$$

with $n \in \mathbb{Z}$, G being the reciprocal lattice vector and T the time it takes to traverse the brillouin zone at constant F . Using those we can conclude:

$$F/\hbar \int_0^T dt \frac{dr}{dt} = F/\hbar \int_0^T dt \nabla_k E(k_0 + F/\hbar \cdot t) \quad (7.5)$$

$$= E(k_0 + G) - E(k_0) = 0 \quad (7.6)$$

which shows that there will be no net displacement on the lattice for the static force case. By modulating the force as in [33], however transport accross the lattice becomes possible. In the 2D case it is even not necessary to modulate the force to induce transport, it is sufficient to provide a force which is slightly misaligned from the lattice axes.

If the angle is chosen correctly it can lead to a very long transport across the lattice in perpendicular direction to the force. Illustrated in fig. 7.1 is the movement accross a 2D Brillouin-zone which easily explains the transport phenomena associated with the 2D case: while the Bloch-Oscillations along the force direction cancel out the net movement in real space very fast they accumulate positive or negative momentum and thus movement along the perpendicular axis for a very long time if the force angle is relatively small. For our optical lattice we can calculate the transport by giving our band energy as[56, 85]:

$$\epsilon(\mathbf{k}) = \sqrt{s} - 2J(\cos((k_x + F_x/\hbar \cdot t)d) + \cos((k_y + F_y/\hbar \cdot t)d)) \quad (7.7)$$

with

$$s = V_0/E_r \quad (7.8)$$

$$E_r = \frac{\hbar^2 k^2}{2m} \quad (7.9)$$

$$J = \frac{4}{\sqrt{\pi}} E_r s^{3/4} e^{-2\sqrt{s}} \quad (7.10)$$

and by putting those in eq. (7.2) yields:

$$r(T) = 2J \left(\frac{\frac{\cos(k_x d) - \cos(d(\frac{F_x T}{\hbar} + k_x))}{F_x}}{\frac{\cos(k_y d) - \cos(d(\frac{F_y T}{\hbar} + k_y))}{F_y}} \right) \quad (7.11)$$

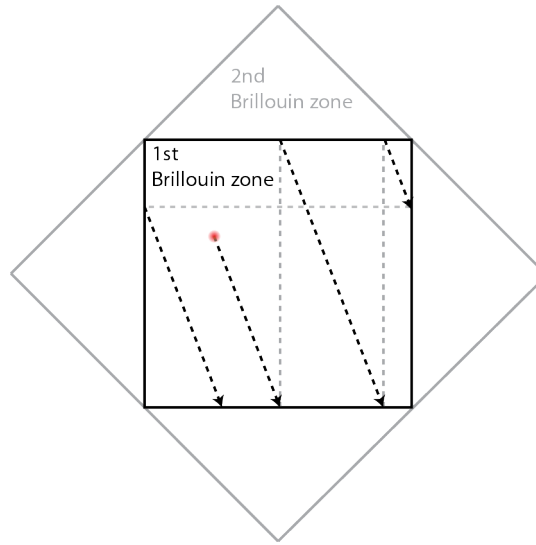


Figure 7.1.: The k -vector in the 1st Brillouin-zone of a 2D lattice is being dragged along it due to an external force. If the force angle is slightly mismatched to the lattice's main axes we can see a large transport in the perpendicular direction as the net momentum switchings along the semi-parallel axis mainly cancels net movement in that direction while the perpendicular component stays in either positive or negative regions of the Brillouin-zone for a longer time, leading to transport.

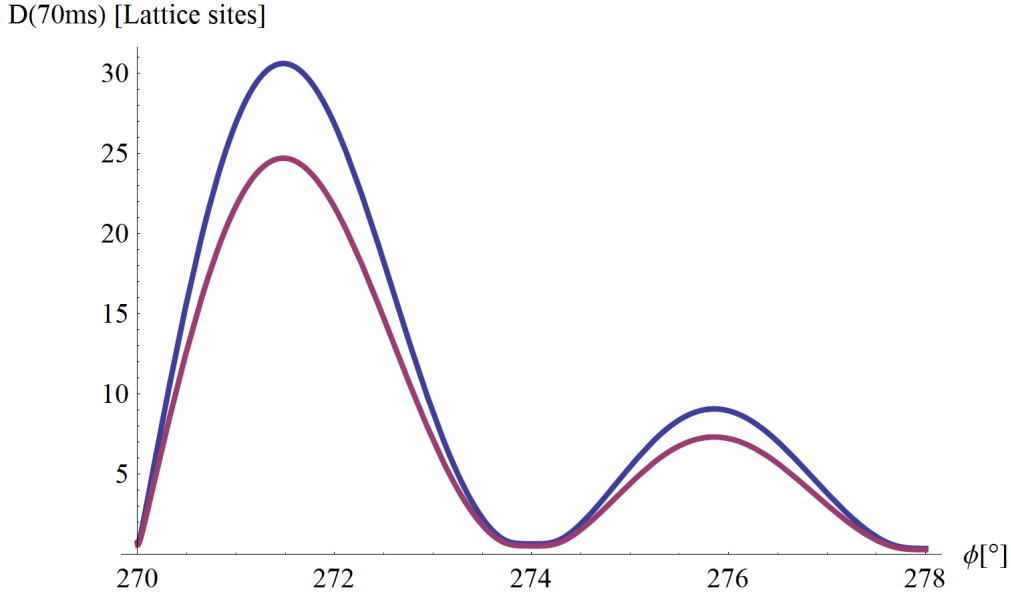


Figure 7.2.: Comparison of the predicted total transport distance for: 70ms, lattice size $1534/2\text{nm}$, $P = 7E_r$, $F = g/8$ pointing in ϕ blue: model from eq. (5.47), purple: model eq. (5.45)

Another way would be to directly calculate the tunneling (J) parameters using the Wannier-functions as described in section 5.3 which obtains us with a slightly different value and of course also changes the total transport distance prediction. A comparison of the two models is shown in fig. 7.2;

From eq. (7.11) we can obviously infer that this transport has an oscillatory behavior as well but for the right timings and force we can observe a large transport across the lattice before the cloud returns to its origin. For a deeper understanding it is helpful to plot the behavior of $r(T)$ vs time, $r(T)$ vs force angle for fixed time and so on, as in fig. 7.3.

7.2. Magnetic fields and electro/magnetic stability

7.2.1. Side coils

To induce the necessary force we can rely on magnetic fields generated by our trap coil and an additional gradient coil assembly in x-direction. By overlapping the fields of two coils we gain the possibility to rotate the force vector in a 2D plane by varying the currents to those coils. With the later mentioned Ring-Exchange experiment in mind we planned a pair of coils which together with the trap coils should be able to generate gradients up to 100G/cm along the diagonal direction². Further requirements were the

²The current requirements for the Bloch-Oscillation induced transport experiment are smaller.

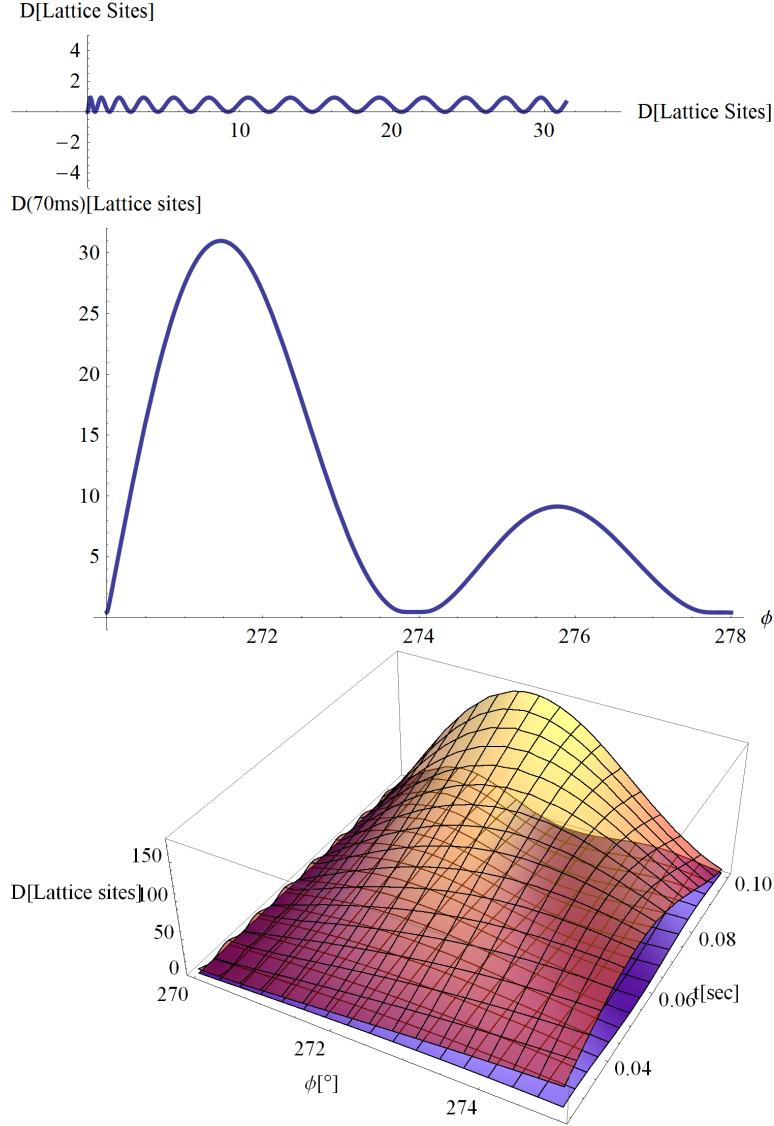


Figure 7.3.: 1) Bloch oscillation induced transport, $r(t)$ from 0 to 70ms, initial k -vector and force shifted by 1° from gravity direction, $F = g/8$ strength, $\lambda = 1534\text{nm}$ lattice (yields an effective lattice period of 767nm) at $7E_r$. 2) Distance from initial position after 70ms of transport for different force angles (ϕ), same lattice strength and force magnitude. 3) Distance from initial position VS transport time and force angle at same overall magnitudes in comparison with a shorter lattice ($\lambda = 1534\text{nm}$ (blue tones), $\lambda = 767\text{nm}$ (red to yellow)). Distances are given in lattice sites which are individually normalized to the respective lattice size.

option to generate an additional offset field if need arises and a high homogeneity thereof.

Due to the high required gradient it was necessary to either produce a coil with many windings or a small coil nearby the glass cell with an intermediate amount of windings. As there was not enough space to put a large coil with enough windings outside the magnetic transport frame we settled for a small pair of coils which would be placed with only millimeter distance to the sides of the glass cell and almost filling the complete height between the transport plates. We printed a special holding frame with a 3D printer in which the coil pair could be glued (see appendix E for drawings). Unfortunately the left holding clamp construction was a bit too thin and one plastic holder broke off during installation which necessitated the production of an alternate holding clamp made out of metal in which the original clamps could be enclosed (see appendix E, last two drawings). The coils themselves consist of 8 layers wound in the same direction with 10 windings per layer. Due to the tight space constraints every two layers have to be connected to each other externally which is actually not bad as we can use either e.g. 2×4 layered coils or a single 8 layer coil. The calculations were carried out for the following setup:

- Two coils each having 4 layers.
- Inner radius of 14.5mm
- Outer radius of 20mm
- Wire strength 0.55mm (0.5mm wire, rest should be from glue)
- Inner distance of 4.4cm between the coil pairs

which yields a current requirement of 9.910A for the trap coil and -8.789 A for the new gradient coils when a gradient of 100G/cm along 315° is desired. Due to the high currents and relatively small wire thickness one has to carefully check the temperature stability of the coils as those are not actively coolable. When one uses 10A in a pulsed sequence of 18s (which is a typical cycle duration) the coil's temperature will oscillate around a semistable value reached through heating and cooling between current pulses. The semistable value depends on the pulse's duration and was measured over a term of 20 minutes within which the coils normally reached their semistable condition.

Pulse duration	T[°C]
100ms	27,7
150ms	30,0
200ms	33,3
400ms	44,6

As we will most likely use currents slightly below 10A and pulses of about 100ms this should not pose a problem for the coils, especially as the glue stability (UHU Plus 300 epoxy) only starts to deteriorate significantly beyond 40°C , and can in principle work

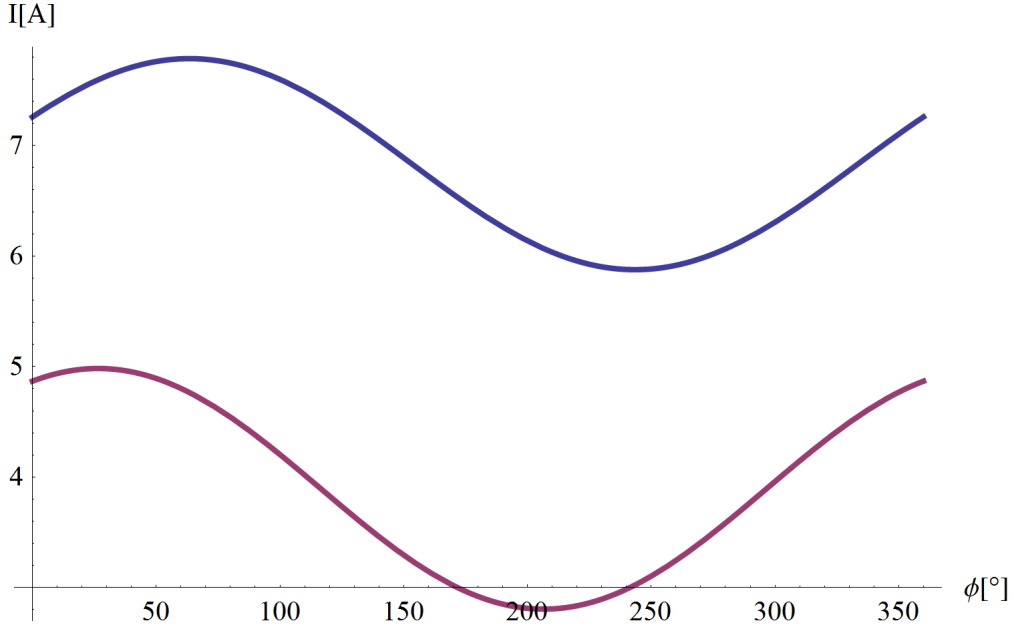


Figure 7.4.: Required currents to generate a force with magnitude $g/8$ along the desired angle. Blue is the current for the trap coil, purple for the side coils using 4 of the 8 available layers of each coil.

up to 100°C. Like in section 6.3 we can set up a simulation of our coils that solves the equation:

$$\nabla \mathbf{B}_{\text{trap}}(I_1) + \nabla \mathbf{B}_{\text{x}}(I_2) = \begin{pmatrix} 2m_{Rb} \frac{g}{n} \cos(\Phi) / \mu_B \\ 2(m_{Rb}g - m_{Rb} \frac{g}{n} \sin(\Phi)) / \mu_B \end{pmatrix} \quad (7.12)$$

where ∇B is approximated by first order forward finite difference, g earth's acceleration, n for fractional force magnitude selection, and we used:

$$F = g_F m_F \mu_B \nabla \mathbf{B} \quad (7.13)$$

where g_F is the same as in eq. (6.2).

7.2.2. Magnetic field stability and effects

As already mentioned the precision of the force's angle and magnitude is crucial to the transport, depending on the deviation of the force we will end up more or less far displaced from the predicted destination. We measured our current sources noise using an Agilent 34410 multimeter which can store 50k samples in one measurement and has a sampling rate up to 1kHz, enabling us to resolve up to 500Hz frequency noise. The precision depends on the integration time, it is given in the manual and has been verified for the selected speed with a null measurement. From the FFT we see in fig. 7.5 that the primary noise on our power supply is from 50Hz which most likely couples in from

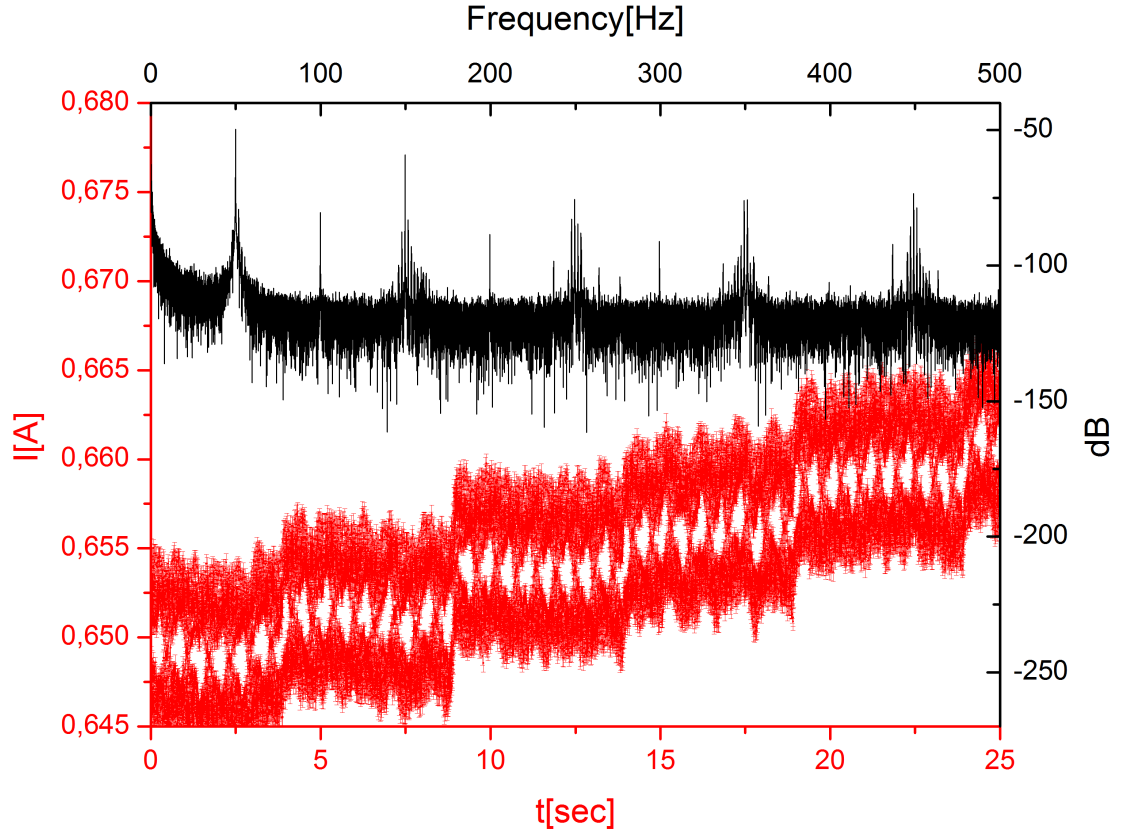


Figure 7.5.: Noise of the current supplies for the trap gradient field showing mainly 50Hz noise from the powerline, the resolution is smaller than the AdWin resolution where normally each step is clearly separated from the next one. The min-max deviation is 11.3mA and $\sigma = 3.1\text{mA}$.

the powerline over the voltage transformers in the boxes. To simulate the effects on our transport we evaluated eq. (7.2) with keeping F dynamically changing as:

$$\mathbf{r}(T) = \int_0^T 2dJ \sin [d(\mathbf{k} + \mathbf{F}(I_1, I_2, \Delta I_1, \Delta I_2, \Phi, t)/\hbar)t] dt \quad (7.14)$$

and:

$$F = F_B(I_1, I_2, \Delta I_1, \Delta I_2, \Phi, t) + F_G \quad (7.15)$$

$$B(I_1, I_2, \Delta I_1, \Delta I_2, t) = B(I_1 + \Delta I_1 \sin(50 \cdot 2 \cdot \pi t)) + B(I_2 + \Delta I_2 \sin(50 \cdot 2 \cdot \pi t + \Phi)) \quad (7.16)$$

If we assume an order of 5mA noise on the current the modified transport should look like in picture one of fig. 7.6, whereas already 10mA would most likely yield unuseful behavior as seen in the second picture of fig. 7.6. The phase between the two currents is not really fixed in our system but in principle the minimum total transport distance would occur at $\Phi = \pi$ and its overall effect of phase is normally negligible.

7.3. Experiment

7.3.1. Preparation

In the old lab we tried producing a very small BEC to facilitate a good starting condition from which we could easily see transport. We could reach e.g. ~ 130 atoms by ramping down our dipole trap to 0.05V, hold it there for 200ms and then ramp up again linearly to 5V in 2s (seen in fig. 7.7). For the case of a 2D lattice using $\lambda = 767\text{nm}$ at $7E_r$ we can calculate the optimal magnetic fields for a lattice tilt of 4.18° and an acceleration magnitude of $g/8$ as: 5.970A for the trap and 3.390A for the X-coil, yielding a force direction along 269° .

Ideally we should ramp to the desired value within 1ms so the atoms can follow the change of the magnetic field vector, for the side coil the ramp speed is on this order, so a square pulse will actually produce a curve which meets this requirements; the trap coil can follow a square pulse on the order of $500\mu\text{s}$, so a linear ramp of 1ms should perform better.

As of writing we could neither use the high-resolution imaging nor the side coil as it would need careful realignment of the system so we tried to find other parameters which might still work for the available system. Considering our $\sim 4.18^\circ$ lattice tilt (obtained from 4th order KD-scattering centers (fig. 6.18)) we can expect transport behavior in our system by applying 0.595A to the trap coils, leading to a transport of over 120 lattice sites within 70ms which is the same as for the calculated 2D magnetic field currents given above.

7.3.2. First test in 2D, observation of 1D Bloch Oscillations

We loaded a 2D lattice within the pancake while maintaining additional confinement from the dipole beams and tried to observe the transport by tuning down the magnetic

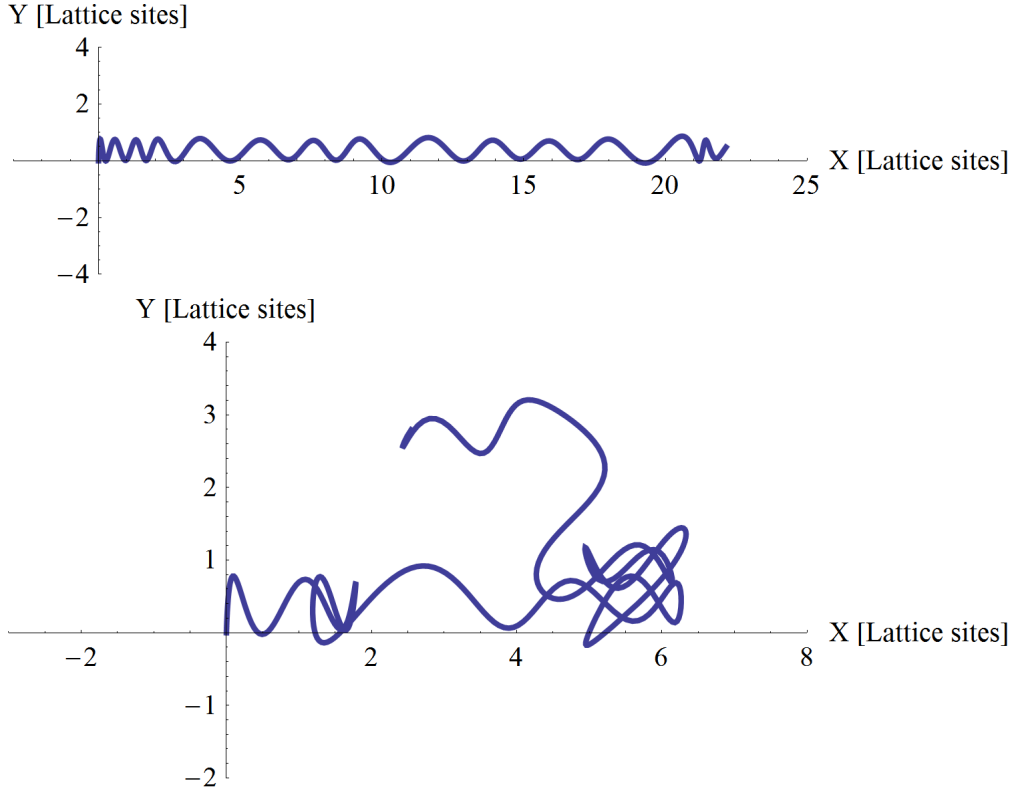


Figure 7.6.: Effects of electrical noise on the transport, we show the predicted $D(T)$ curves for two cases: a) $\pm 5.5\text{mA}$ on the transport coils and $\pm 3.5\text{mA}$ for the X-gradient coils and b) $\pm 10\text{mA}$ for both coils which would most likely make any transport indiscernible from noise.

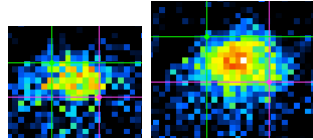


Figure 7.7.: Tiny BECs of approximately 130 and 250 atoms.

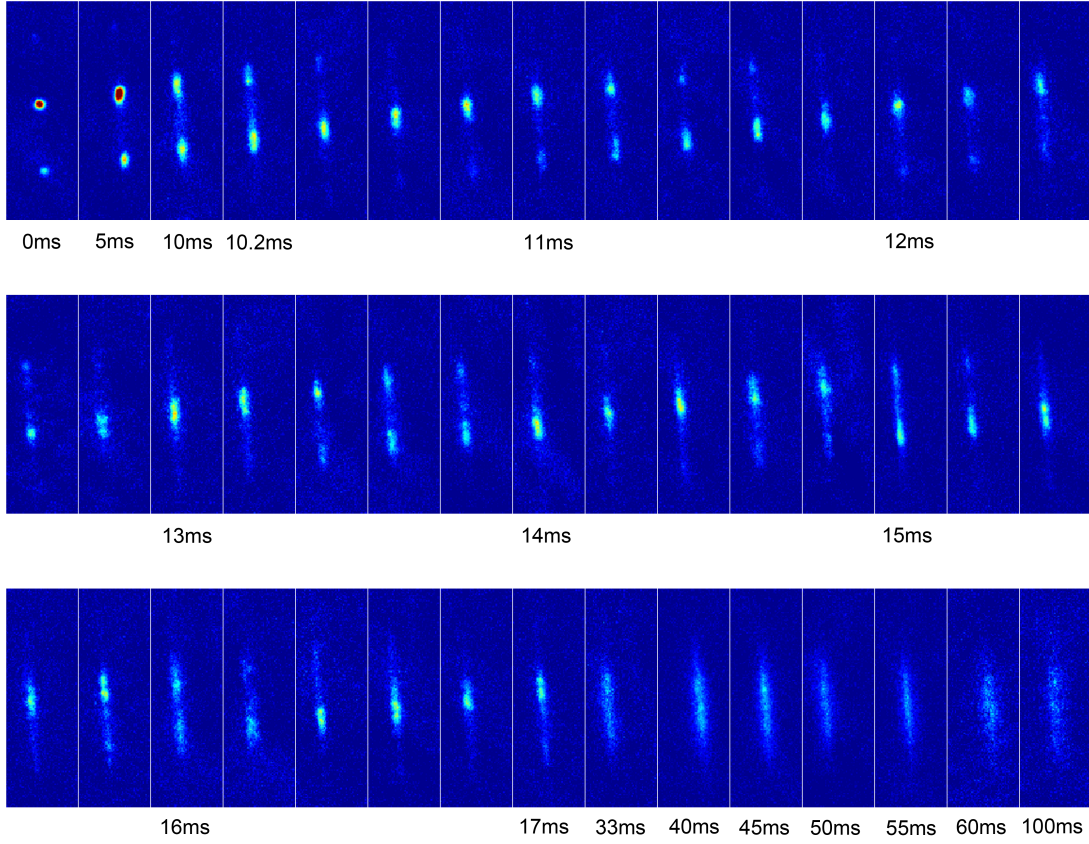


Figure 7.8.: 1D Bloch oscillation in a vertical lattice due to gravity visible for 17ms, but already decohered at 33ms.

field of the trap coil to the estimated $0.6A$, waiting for 70ms and then taking pictures. The transport could not be observed, however, which led to further investigation.

We tried to observe the Bloch Oscillations using a simplified approach and first disabled the x-lattice and the pancake, creating a semi-1D lattice in which we could observe Bloch Oscillations. Experiments showed that it is helpful to turn off the main dipole trap during the oscillation and tuning the cross-dipole to $0.45V$ from $1V$ during the lattice holding period. We also turn off the magnetic field completely for this test and the primary force which acts on the atoms should be gravity³. It is necessary to keep the main dipole at least above $0.4V$ to provide sufficient confinement to the atoms, higher values might introduce higher scattering rate loss and decoherence.

³Another effect which will definitely play a role for the 2D case is the inhomogeneity due to the gaussian beam shapes, leading to effective forces between lattice sites, especially in the outer regions.

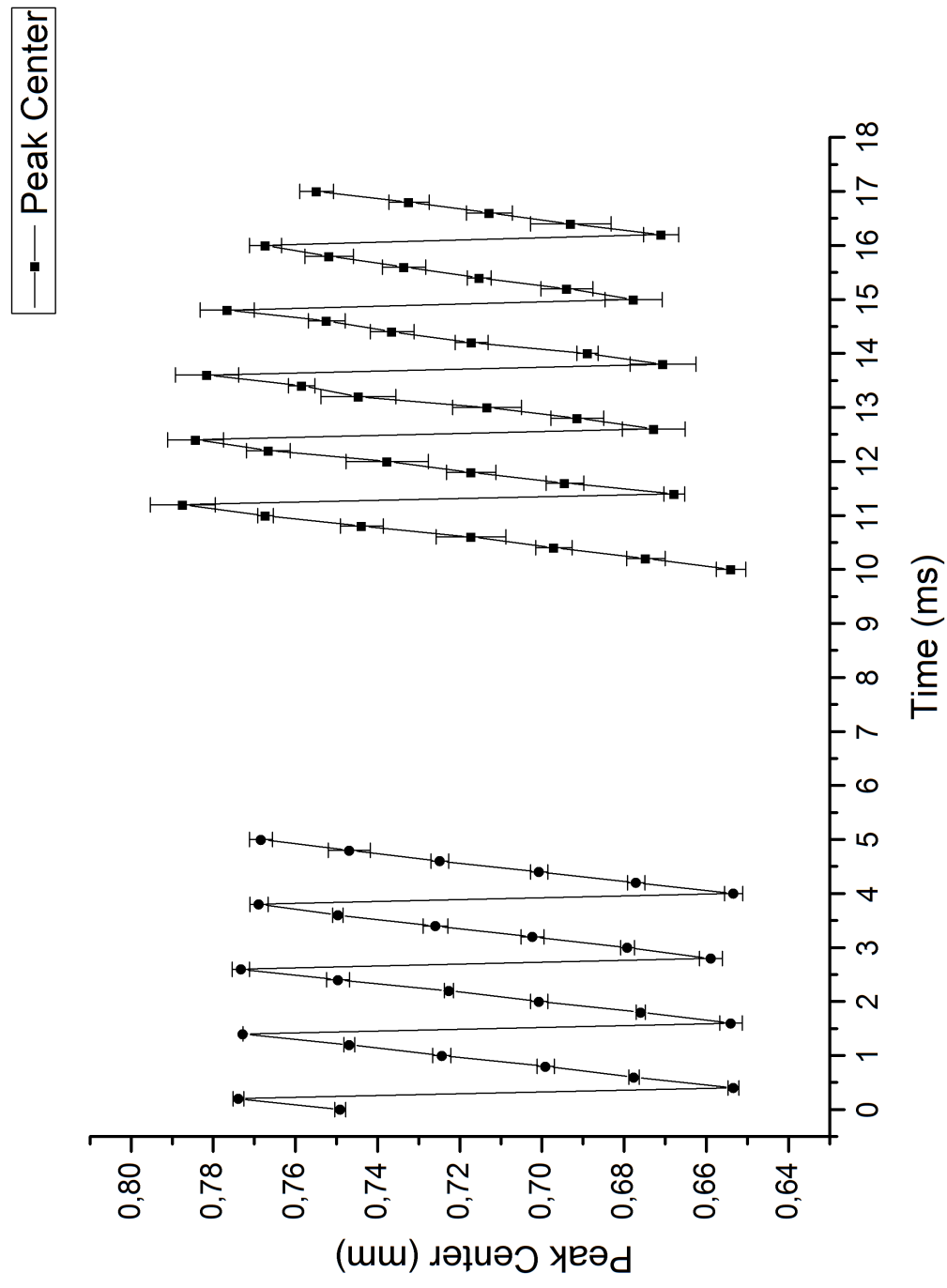


Figure 7.9.: Oscillation period extracted from fig. 7.8, yielding 1.2ms.

In fig. 7.8 we can see the evolution of the Bloch Oscillations for different holding times, we switch off the lattice and magnetic field instantaneously⁴ and observe the cloud after 12ms TOF. From the TOF images we can extract the oscillation period as 1.2ms as seen in fig. 7.9. The main decoherence should be due to the high scattering length/rate of ⁸⁷Rb, although from a similar experiment in 1D using Cs which for some cases is tuned to the approximately same scattering length as ⁸⁷Rb by Nägerl's group [33, 30] we would expect a coherence time long enough to see the transport.

We analyzed the decoherence timescale by measuring the spread of the momentum distribution as in [54, 30]. A comparison with thermal atoms shows a clear advantage of using BEC due to their initially collective almost zero momentum; decoherence due to 2-body collisions due to higher density will only play a role where the thermal atoms have already reached a completely smeared out momentum distribution, see fig. 7.10. For the BEC case a longer timescale evolution can be seen in fig. 7.11, the decrease of momentum spread around 30ms could indicate a weak Bloch-Oscillation revival as demonstrated in [54] but normally one would expect a better signal to noise ratio in such a case.

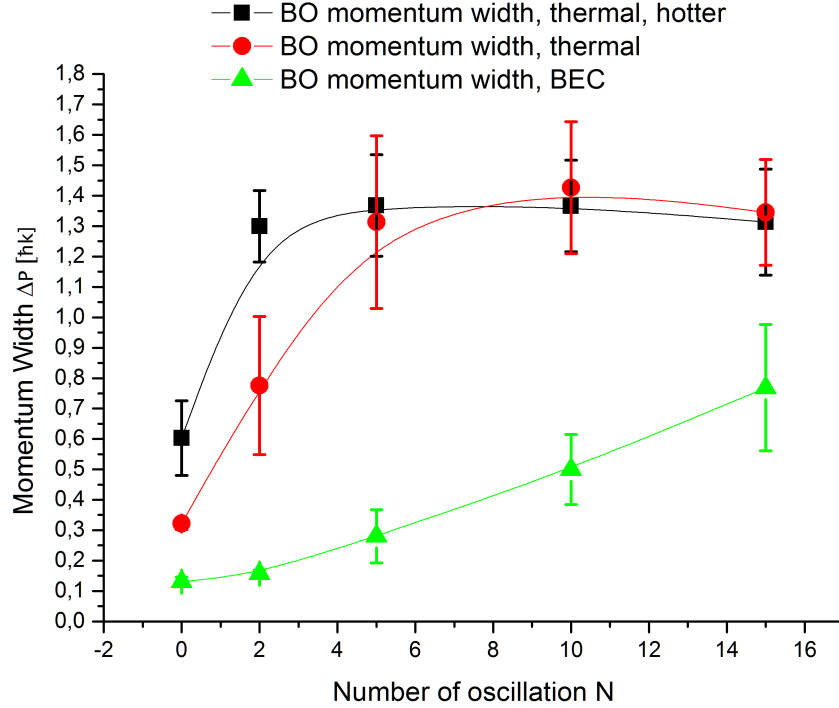


Figure 7.10.: Spread of the momentum distribution of 1D Bloch-oscillations using thermal and Bose-Einstein condensed atoms.

⁴It leads to an exponential drop with 50μs to 1ms timeconstant which depends on initial to final current and are empirical values from measurements of the PI current monitor as well as eddy-current induced magnetic field noise measurements.

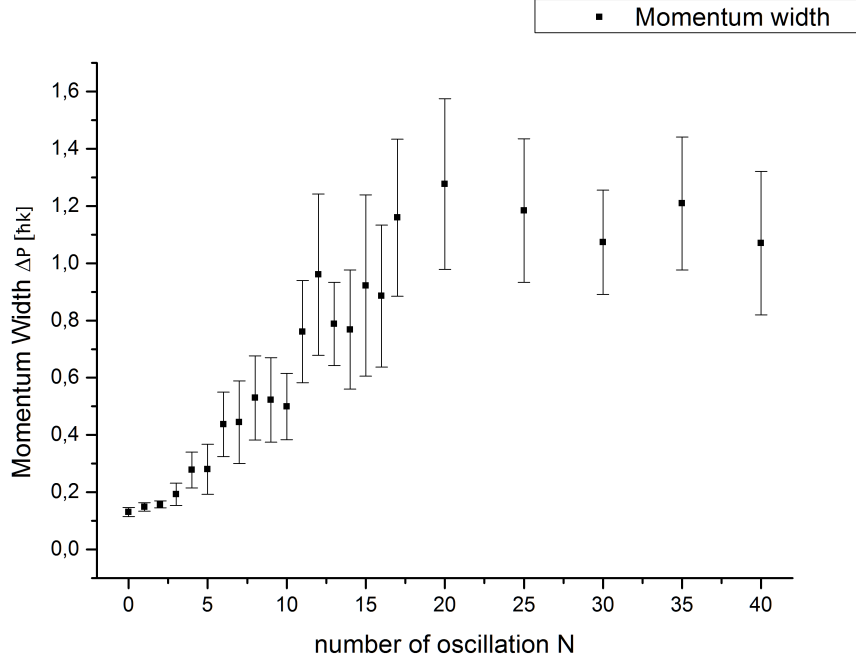


Figure 7.11.: Spread of the momentum distribution of 1D Bloch-oscillations using BEC atoms for a longer timescale.

7.3.3. Revisiting the 2D case

The 2D geometry might however have crucial differences, the gaussian beam shape of the blue detuned lattice leads to a difference of acceleration/force subjected to the lattice sites depending on the distance from the center of the beam. We can approximate this to be on the order of $1m/s^2$ at the 100th lattice site in x direction, which is already much larger than the required value of $\sim 0.6m/s^2$. This could be compensated by using the cross-dipole beam, although only to a certain degree.

A better approach would be to use wide lattice beams which, however, would increase the laser power demand. Furthermore one might scan the current of the magnetic field during the transport to keep the center of mass of the cloud under comparatively constant force, the outer parts of the cloud would still observe some change of the force though which would still lead to a blurring and/or decoherence. Furthermore one should consider the ramping down of the magnetic field; from our preliminary results it is evident that we cannot observe Bloch-Oscillations on the desired timescale. By considering the ramp down of the magnetic field strength at the beginning we might however gain a small improvement of the covered distance in the early time regime. Instead of jumping down to $\sim 0.6A$ with a stepfunction which leads to aforementioned exponential drop of $50\mu s$ to $1ms$, it should be better to tune the magnetic field to $0.71A$ with a $2.5ms$ exponential decay. The $2.5ms$ decay constant has been derived from simulation seen in fig. 7.13, whereas $0.71A$ can be extracted from fig. 7.12;

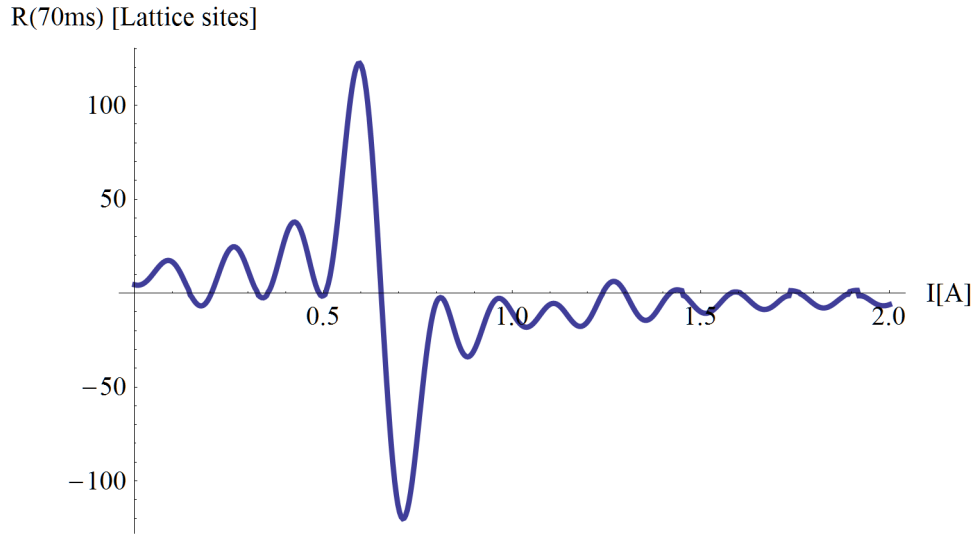


Figure 7.12.: Expected absolute distance multiplied with the x position sign covered after 70ms of transport, indicating why it is preferable to stay at the higher current value.

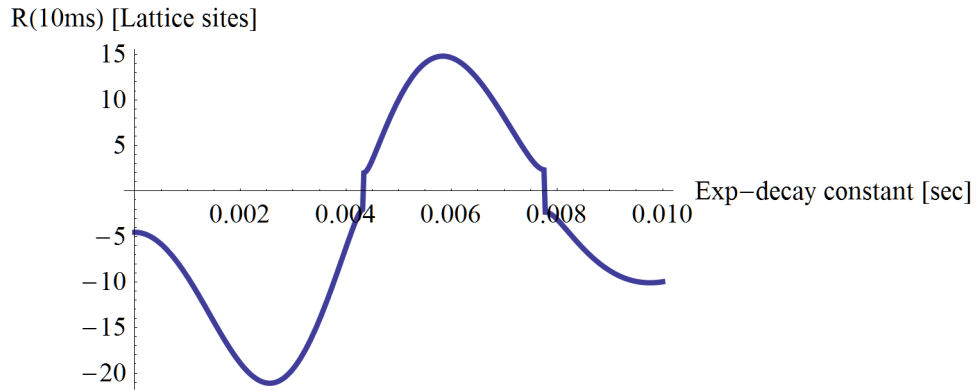


Figure 7.13.: Expected absolute distance multiplied with the x position sign covered after 10ms of transport for different ramp down speeds of the magnetic field.

In fig. 7.12 the total transport of sites multiplied by the x direction sign after 70ms is shown, already indicating why the higher ending current makes sense. In fig. 7.13 we reduce the total transport time to 10ms which is closer to a value which we might actually achieve to observe in-situ ⁵. To see if the magnetic field ramping affected the stability of the Bloch-Oscillations we compare several cases:

- Holding the atoms at the initial magnetic field at 4.6A (compensates gravity) for 2.5ms
- Switching the magnetic field down to 0.71A immediately, exploiting the natural exponential decay of the coils on the order of $500\mu s$ to 1ms.
- Ramping down the magnetic to 0.71A exponentially within 2.5ms.
- The same as point 2 and 3 but with an additional holding time of 1ms.

The results can be seen in fig. 7.14 and suggest that a controlled ramping down to the desired current results in a slightly less increase of Δk than the immediate jump, as the outer diffraction peaks are more pronounced in the ramping case and the central diffraction peak, even though washed out a lot already at 3.5ms, is still less wide for the slow ramp case. This is appreciable for the following measurement in-situ, where we compared several cases to check for presence/absence of transport due to 2D Bloch-Oscillations. We employ the aforementioned optimizations of a 2.5ms exponential ramp down of the magnetic field and scan only within 10ms from the onset of ramping down the magnetic field current, as we cannot expect any coherence beyond this point from the previous measurements.

In fig. 7.15 we plot our findings of transport due to Bloch-oscillations once VS time with a fixed target current of 0.73A. In the first plot while the second plot kept the imaging time fixed at 7ms;10ms and we scanned the final current value after the 2.5ms ramp-down. We see a transport of about 0.8 pixels center-of-mass movement in the ideal case of 0.73A final current which is about $2.4\mu m$ according to our estimated resolution of $3\mu m$ with the standard objective. Compared to the case where we keep the current at 4.5A we can see a clear difference outside the 1σ region even though it is quite large for all datapoints. Each datapoint was obtained by averaging 20 gaussian fits to 20 individual pictures which had been cleaned of background noise beforehand [60].

We cannot, however differentiate well between cases where we ramp down the current to different values than 0.73A because both error bars are large and theoretical differences are small on the accessible timescale. Especially the case for ramping down to 0A should yield only a fraction of the observed covered distance (nonzero because of the lattice tilt!), we cannot differentiate this case from the “optimal” one in our measurement (see fig. 7.15, picture 2). The total distance which is covered in the “optimal” case is also

⁵An upcoming 2D measurement using TOF shows observable oscillations for only 3.5ms, as the TOF time is 12ms, however we might still see something in-situ for a longer time than 3.5ms. Gustavsson of Nägerls group also switches the scattering length to 0 during TOF in [30] to reduce decoherence/momentum spread during TOF for non-zero scattering length Bloch-Oscillation experiments which led to this assumption.

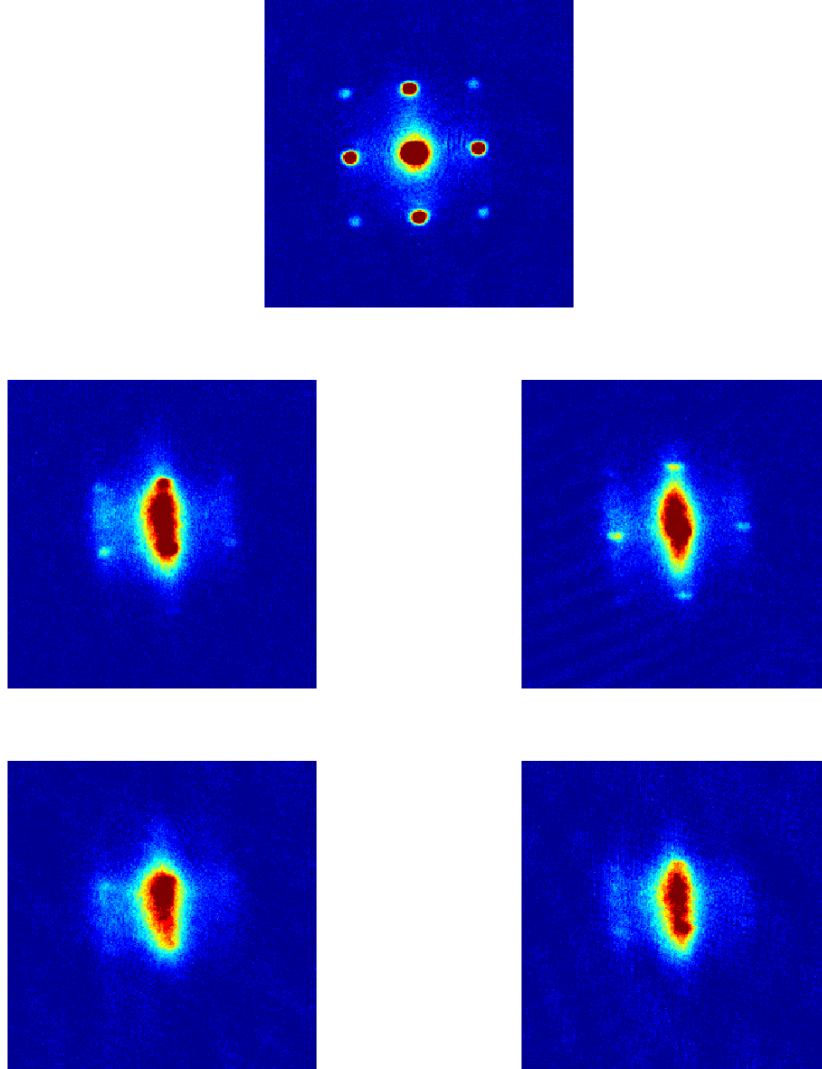


Figure 7.14.: TOF Images of 2D Bloch-oscillations: First picture: Current held at 4.6A after 2.5ms holding time as “zero-reference”, 2nd row: comparison between “jumping” the current from 4.6A to 0.71A and ramping the current from 4.6A within 2.5ms exponentially down to 0.71A, each 2.5ms after the current decrease started, 3rd row: the same as the second row but with an additional 1ms holding time.

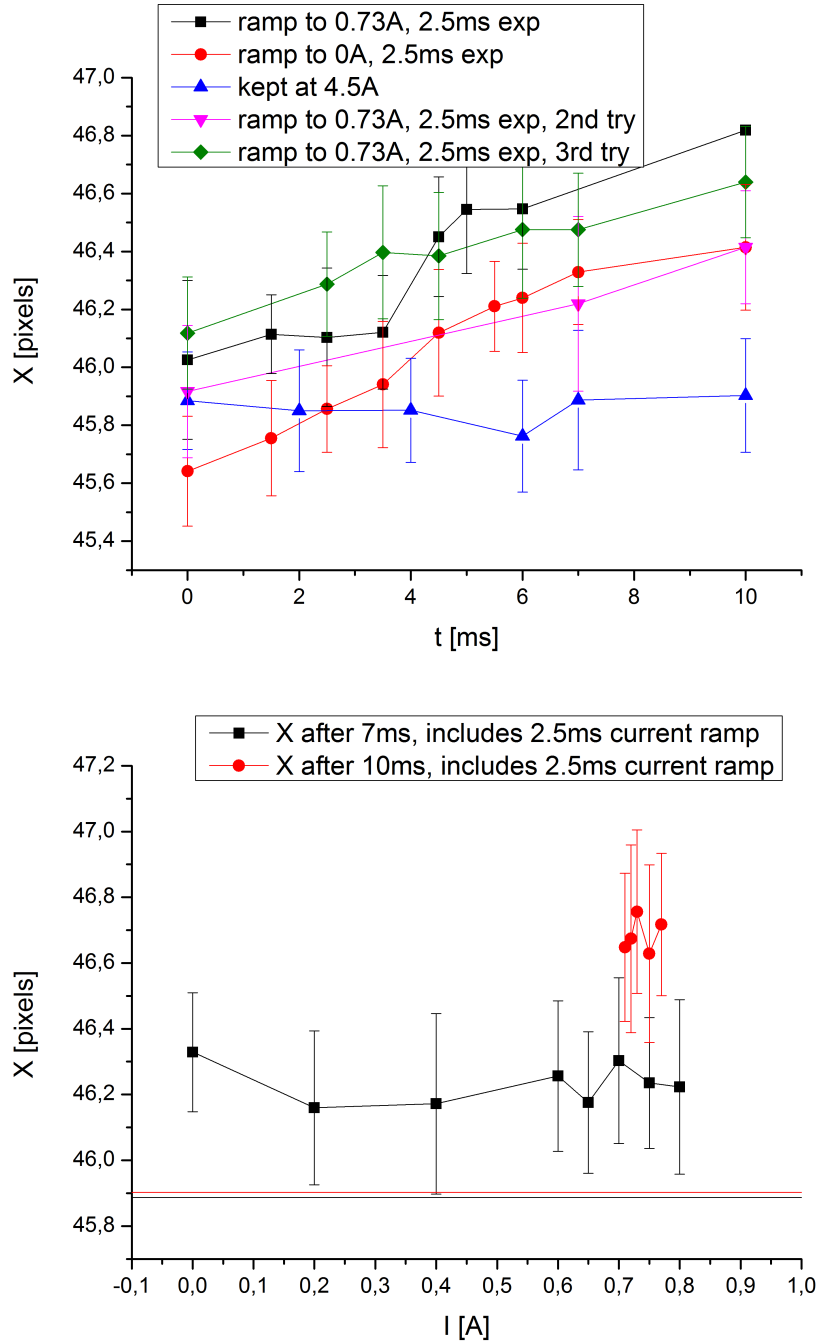


Figure 7.15.: In Situ analysis of the center of mass position/transport of a small BEC in a lattice of $7E_r$ for different cases of timings with fixed final magnetic field strength/force and for fixed timings and varying final magnetic field strengths/forces. The horizontal black and red lines in the second plot indicate the “0” position if we would keep the current at 4.5A and kept the atoms held for the same amount of time.

smaller than the predicted distance by almost $1/2$. From the TOF pictures (fig. 7.14) we can also not make a clear statement for the in-situ coherence after the 3.5ms mark - it should be a bit longer as the atoms still interact during TOF which leads to further decoherence, but to which degree this plays an effect we do not know. As the force difference on the atoms from the 4.5Å case and the 0.73Å case is less than one g and the lattice is at $7E_r$ the transport phenomena has still to originate from dynamics in the first Brillouin zone. It is not clear if those originate from Bloch-Oscillations in the observed timescale from 3.5 – 10ms.

The transport effect is, however, repeatable and separable from the non-moving case with 2σ confidence. To get a clearer result it will be necessary to use the high-resolution imaging system as well as further improvements on the system. The main decoherence effects should be the large scattering length of ^{87}Rb and the differential force on the atoms depending on position of the lattice. It would be necessary to widen the lattice beam waist and it would be beneficial to use a red instead of a blue detuned dipole trap to improve the latter effect. A further possibility might be the usage of RF-driven feshbach resonances as described in [34, 43, 74] to decrease the scattering length, which we will discuss a bit more in chapter 9.

8. Ring exchange Experiment

8.1. Theory

In “Minimum instances of topological matter in an optical plaquette” [61] Paredes and Bloch suggest several experiments regarding topologically ordered states, including resonating valence bond (RVB), Laughlin-states, string-net condensed states and a ring-exchange interaction across a plaquette. Thereof Bloch’s group realized the RVB in an experiment[57] later on.

We were particularly interested in the ring-exchange as it is a GHZ state using one plaquette. We will first give a brief overview over the mentioned possibilities as an introductory overview of possible experiments on plaquettes and then describe the requirements of realizing the ring exchange.

As already mentioned in section 6.4 we use a superlattice of two wavelengths and all further mentioned experiment (suggestions) require the use of such a system. The tunability of the laser’s phase and intensities opens us up the possibility to either have double wells in either direction going over imbalanced double wells to the other extreme of combining two into one big well. Furthermore we can tilt the potential of each plaquette along e.g. the diagonal axis using a magnetic gradient field as will be required later on. Like in [57] we denote the corners of our plaquettes as given in fig. 8.1 and use the suggested states of ^{87}Rb : $|\uparrow\rangle = |F=1, m_F=1\rangle$ and $|\downarrow\rangle = |F=1, m_F=-1\rangle$. and give the Hubbard Hamiltonian associated with a single plaquette by:

$$H = - \sum_{\langle i,j \rangle, \sigma} t_{ij} (a_{i\sigma}^\dagger a_{j\sigma} + H.c.) + U \sum_{i, \sigma, \sigma'} n_{i\sigma} n_{i\sigma'} + \sum_{i, \sigma} \mu_{i\sigma} n_{i\sigma} \quad (8.1)$$

where $a_{i\sigma}$ is the bosonic annihilator, $n_{i\sigma}$ the number operator for sites i and spin σ , t_{ij} the tunneling amplitude between sites $i \rightarrow j$; in our case e.g. along the x direction for t_{12}, t_{34} and finally $\mu_{i\sigma}$ being an offset energy at respective sites.

8.1.1. RVB states

RVB states were suggested already in 1931 by Pauling [62] to characterize chemical bonds of molecules, later on reexamined by Kivelson and Anderson for high-TC superconductivity[45, 3] and as already mentioned in the papers by Paredes/Bloch and the experiment by Nascimbene [61, 57]. For a four particle plaquette the states are:

$$|\Phi_{\pm}\rangle \propto \left(s_{1,2}^\dagger s_{4,3}^\dagger \pm s_{1,4}^\dagger s_{2,3}^\dagger \right) |0\rangle \quad (8.2)$$

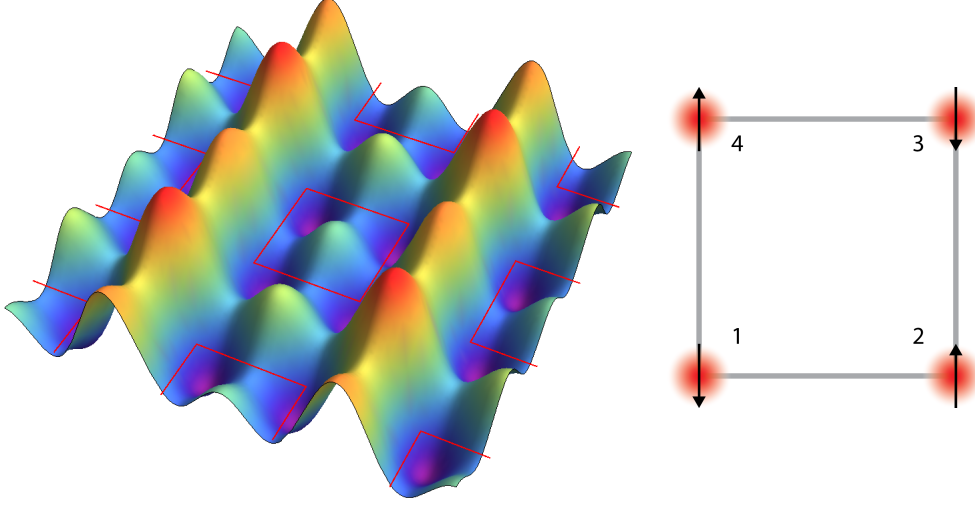


Figure 8.1.: a) Arbitrary superlattice potential showing imbalanced double well structure and plaquette overlay. b) Numbering order of the plaquette corners.

where $s_{i,j}^\dagger = (a_{i\uparrow}^\dagger a_{j\downarrow}^\dagger - a_{i\downarrow}^\dagger a_{j\uparrow}^\dagger)$ creates a singlet state at sites i and j with $|0\rangle$ being the vacuum state. To generate the RVB state it was suggested to start out with the four single particles per site and only allow tunneling along one direction e.g. y . The initial state is then:

$$|VB_y\rangle = s_{1,4}^\dagger s_{2,3}^\dagger |0\rangle \quad (8.3)$$

and by adiabatically turning on tunneling along x it will be transformed to $|\Phi_+\rangle$. In the experimental realization the procedure is as follows (description from: [57]): On a short and long x/y lattice with 767nm and 1534nm with an additional 844nm z -confinement lattice the atoms are loaded into a $n = 1$ Mott-insulating state. In the following the y -double wells are merged to allow for spin-changing collisions, separated again and then one waits for the singlet-triplet oscillations. This creates the initial $s_{1,4}^\dagger s_{2,3}^\dagger |0\rangle$ state. This state can be evaluated by band-mapping techniques of which we don't go into further details here.

The final state $|\Phi_+\rangle$ was created by exploiting the fact that it is adiabatically connected with the initial state: by ramping the short x lattice down using an adiabatic curve and ramping it up again it is possible to probe the oscillations between the two states of $|\Psi_+\rangle$. The theoretical description in [61] for the adiabatic turn on is interesting in light of its connection to the next section: it assumes very small values for the tunneling amplitudes in x and y direction in comparison to the on-site interaction ($tx, ty \ll U$)

and the system is governed by the so-called superexchange interactions:

$$H_S = J_x(\hat{P}_{1,2} + \hat{P}_{3,4}) + J_y(\hat{P}_{2,3} + \hat{P}_{1,4}) + \dots \quad (8.4)$$

with $\hat{P}_{ij} = s_{i,j}^\dagger s_{i,j}$ being the projector on a singlet state at sites i, j , $J_i = 4t_i^2/U$ and the dots hint higher order terms in J [61]. A sudden increase in e.g. t_x from 0 to $t_y (> 0)$ will produce oscillations between $|VB_x\rangle$ and $|VB_y\rangle$ with resonance frequency $2J_y/\hbar$ as seen in [57].

8.1.2. Laughlin state

Laughlin states[48] play a major role in the explanation of the fractional quantum Hall effect [75]. On a plaquette a Laughlin state of two particles can be created using $|\phi_+\rangle$ and rewriting its form [61] using:

$$|\Phi\rangle = \sum_{x_1, x_2} \psi(x_1, x_2) S_{x_1}^+ S_{x_2}^+ |\downarrow\downarrow\downarrow\downarrow\rangle \quad (8.5)$$

where S_x^+ is the spin raising operator for site x and $|\downarrow\downarrow\downarrow\downarrow\rangle = a_1^\dagger a_2^\dagger a_3^\dagger a_4^\dagger |0\rangle$. Rewriting a four spin state in such a way is valid if the total spin sum is zero. $|\Phi_+\rangle$ can now be used to write:

$$\psi(x_1, x_2) = z_1 z_2 (z_1 - z_2)^2 \quad (8.6)$$

with $z_i = e^{i\pi/2x_i}$, $x_i = 1, \dots, 4$ and by removing the spin down particles the other spin up particles will form a Laughlin state. It is an eigenstate of the total angular momentum operator $\hat{L} = \sum_m m a_m^\dagger a_m$ with eigenvalue $L = 4$ and $a_m^\dagger = \frac{1}{2} \sum_{l=1}^4 e^{i\pi/4ml} a_l^\dagger$ being the creation operator for a particle with angular momentum m [61]. This state is equivalent to a quasi-hole state at the center of the plaquette and by rewriting eq. (8.4) as

$$H_S = \frac{1}{2} S^2 - H_{HS} \quad (8.7)$$

with $H_{HS} = \sum_{i,j} J_{i,j} \hat{P}_{i,j}$ (the Haldane-Shastry model) and $J_{i,j}^{-2} = \sin(\frac{\pi}{2N}(x_i - x_j))$ the excitations of H_S are of the form of $\frac{1}{2}$ quasiholes which are equivalent to $\frac{1}{2}$ anyons [61].

8.1.3. Ring exchange

Originating from lattice gauge theories [46] comes the minimum lattice gauge Hamiltonian describing a system of four spins [61]:

$$H_G = -J_\square S_1^x S_2^x S_3^x S_4^x + J_+ \sum_{\langle i,j \rangle} S_i^z S_j^z \quad (8.8)$$

where the first term is from our desired ring exchange, also called a flux interaction where all spins simultaneously flip their spins for $J_\square < 0$ and the J_+ terms generate preferably

interactions among neighboring spins where $J_+ > 0$ favors antiparallel neighbors. Now we turn to the groundstate which has the form:

$$|\square\rangle = \frac{1}{\sqrt{2}} (|\uparrow\downarrow\uparrow\downarrow\rangle + |\downarrow\uparrow\downarrow\uparrow\rangle) \quad (8.9)$$

which is a GHZ state. It is of our interest to observe this state without any disturbance from the superexchange which is quite difficult as under normal circumstances the coupling for two particles is stronger than this fourth order exchange. The coupling strengths are normally on the order of $\sim t^2/U$ for second order processes and $\sim t^4/U^3$ for the ring exchange. The trick is now to suppress second order tunneling while keeping the fourth order on a reasonable timescale for an experiment which can be achieved by applying a diagonal magnetic field gradient along the plaquettes as hinted before. The gradient e.g. along the primary diagonal (fig. 8.2) produces an energy gap Δ and changes the effective Hamiltonian by restricting the possible interactions [61]:

$$H_R = -J_\square(S_1^+ S_2^- S_3^+ S_4^- + h.c.) + J_+ \sum_{\langle i,j \rangle} S_i^z S_j^z + J_\times(S_2^+ S_4^- + h.c.) - \Delta \sum_i B_i S_i^z \quad (8.10)$$

and:

$$\begin{array}{l|l} J_\square \approx 24t^4/U^3 & B_1 = 0 \\ J_+ \approx 4t^2/U & B_2 = B_4 = 1 \\ J_\times \approx 16t^4/U^3 & B_3 = 2 \end{array} \quad (8.11)$$

Where eq. (8.8) and eq. (8.10) are equivalent within the subspace generated by $|\uparrow\downarrow\uparrow\downarrow\rangle$ and $|\downarrow\uparrow\downarrow\uparrow\rangle$ [61]. Entanglement in form of the $|\square\rangle$ state can evolve from preparing the state $|\uparrow\downarrow\uparrow\downarrow\rangle$ and letting it evolve for a time depending on $\omega = J_\square/\hbar$. As we normally have our atoms aligned in the $|\uparrow\rangle$ state already from the transport and cooling, we assume that we initially start out with the $|\uparrow\uparrow\uparrow\uparrow\rangle$ state. By tilting the superlattice in x and y direction we can adress spin 1, both spin 2 and 4 or spin 3 by using two-photon raman transitions to flip the spins[49].

In our case we will use the frequency necessary to flip both 2 and 4 at the same time. By assuming a Lorentz-shaped resonance for the spin exchange transition frequencies we estimate the required magnetic field gradients which would be necessary to suppress the second order tunneling to 1% of the fourth order tunneling[10]. Together with some realistic values for potential depths and overall magnitude of the exchange frequencies we can give some reasonable possibilities which could be accessible by:

$U_{\text{blue}}[E_r]$	$U_{\text{red}}[E_r]$	$J[2\pi\text{Hz}]$	$U[2\pi\text{Hz}]$	$J_{\text{neighbor}}[2\pi\text{Hz}]$	$J_\square[2\pi\text{Hz}]$	$\nabla B[\text{G/cm}]$
80	-75	203.56	735.40	225.39	103.62	59.37
90	-95	225.52	766.99	265.23	137.58	69.86

(8.12)

Within $\frac{\pi}{4\omega}$ the initial $|\uparrow\uparrow\uparrow\uparrow\rangle$ will evolve to $\frac{1}{\sqrt{2}} (|\uparrow\downarrow\uparrow\downarrow\rangle + i|\downarrow\uparrow\downarrow\uparrow\rangle)$ which is equivalent to $|\square\rangle$ up to a phase factor and can easily be transformed into same[61].

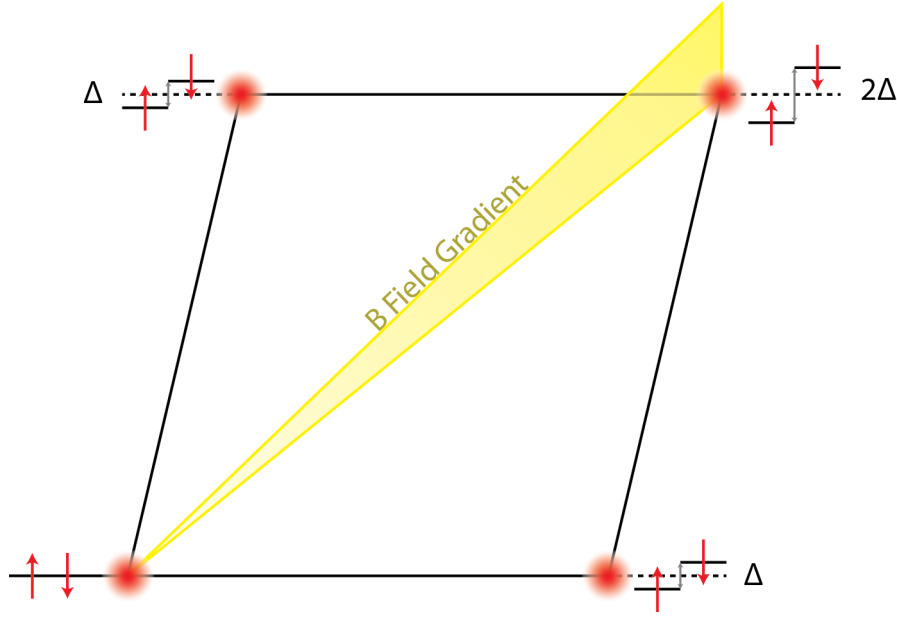


Figure 8.2.: Plaquette with magnetic field gradient applied along the main diagonal and associated energy level shifts.

8.2. Magnetic field stabilization

As the vibrational modes are spaced at about 5kHz[10] in our setup we needed to stabilize the magnetic fields and compensate for background magnetic noise as those would already disturb the addressability in such a narrow band. Stabilization to the required level is not a trivial task, for the approximately 2G offset-field which we use to Zeeman-shift the atomic levels, already 1mG is equivalent to 1.4kHz noise. In a long time measurement we could measure background fluctuations in our old lab to be on the order of 0.7mG which appeared roughly sinusoidal with a period of 36sec and a long time drift range of 2.5mG over 10h. In the new lab we measured background noise on an intermediate timescale to be maximally 1.6mG in the 40 – 50Hz band, 1mG at 60Hz, 0.45mG at 80Hz, 0.1mG at 450Hz and several further peaks below 0.1mG at higher frequencies.

To be able to work with reproducible field strengths we set out to build a locking loop which should stabilize the magnetic fields close to the desired 2G with high precision. As the ratio of magnetic background noise compared to the required offset field is very large we had to split the field generation into two parts. We used the already existing 25 winding offset coil as the main coil to produce the 2G and use another single loop which provides us with a much finer tunability of the magnetic field per applied current for the stabilization. We control the compensation coil current in a feedback loop using a HMC2003 high precision magnetic field sensor (resolution $40\mu\text{G}$), an AdWin 18bit input card and an analog controlled power supply by High-Finesse which has a short term

stability on the order of $3 \cdot 10^{-5} \text{A}$ and a medium term stability of $< 10^{-4} \text{A}$.

It should be sufficient to suppress only field fluctuations along our quantization axis (B_y) as the earth magnetic field is already roughly compensated along the other directions and $B_y \gg B_x, B_z$, we can thus assume:

$$\frac{\Delta \mathbf{B}}{|\mathbf{B}|} = \sqrt{\frac{\Delta B_y^2}{|\mathbf{B}|^2} + \frac{\Delta B_x^2}{|\mathbf{B}|^2} + \frac{\Delta B_z^2}{|\mathbf{B}|^2}} \simeq \Delta B_y = \Delta B \quad (8.13)$$

The HMC2003 outputs 1V per Gauss with a maximum range of 2G^1 to resolve the originally desired 0.1mG background stabilization one needs to be able to detect at least 0.1mV differences.

We first tested a PI card from our electronic workshop together with a 16bit DAC AdWin card as a reference which has a resolution of $0.3 \pm 0.1 \text{mV}$ (theoretically $20\text{V}/2^{16}$). This resolution can be extended to 0.1mV by combining two channels with a passive circuit (see appendix A) made only of resistors and capacitors that divides the voltage of the second channel by roughly 10 and adds it to the first one while at the same time filtering high frequency noise by being a 1kHz lowpass filter. Even though the stability of a single level of the AdWin is quite well it is however not enough to really provide 10 clearly separable sublevels using this approach. But as we can clearly see from the measurement point distribution thickness for individual levels in fig. 8.3 we could use this circuit to deliver an at least 0.1mV stable source. Furthermore we can see that the repeatability for a single level is quite well in the blue cycle (and even longer, but not shown in that graph for readability). What we can also see is that not all levels are equidistantly spaced to each other which could be a small problem if we used the AdWin output as a reference. Using this setup we could already see that the available resolution of the PI card was too low, being only 0.6mV and that another approach to be able to reach better results would be required.

We finally decided on using a multiplexed 18bit AdWin input card, the advantage of the multiplexed card being a stated error of 1 bit smaller than in the parallel version, on the other hand one is more limited on speed if one would want to measure multiple channels as switching the multiplexer takes relatively long. As we already assumed that the stabilization of one axis should be enough this is not a problem. Investigation of the AdWin 18bit card showed that we needed short, shielded cables with careful positioning in relation to other electrical cables combined with an integration/averaging measurement to achieve 0.1mV precision. A main measurement cycle at 100kHz sampling 20 measurements down to an effective speed of 5kHz is sufficient to achieve this precision.

The High-Finesse powersupply supports an analog control input from -10 to $+10\text{V}$ which yields -5 to $+5\text{A}$, along with the 16bit DAC card from the AdWin system this can provide a resolution of about 0.15mA. The needed accuracy for our “one loop coil”² is on the order of $2.7\text{mA} \equiv 10^{-4}\text{G}$ which is more than fulfilled. The PI regulation itself

¹The dynamic range can be extended by using its internal offset coils but this would require a very stable offset current and would still increase the overall error proneness, this is why we rather chose to operate with field strengths $B \leq 2\text{G}$.

² $25 \times 25\text{cm}$ with a distance of 10cm

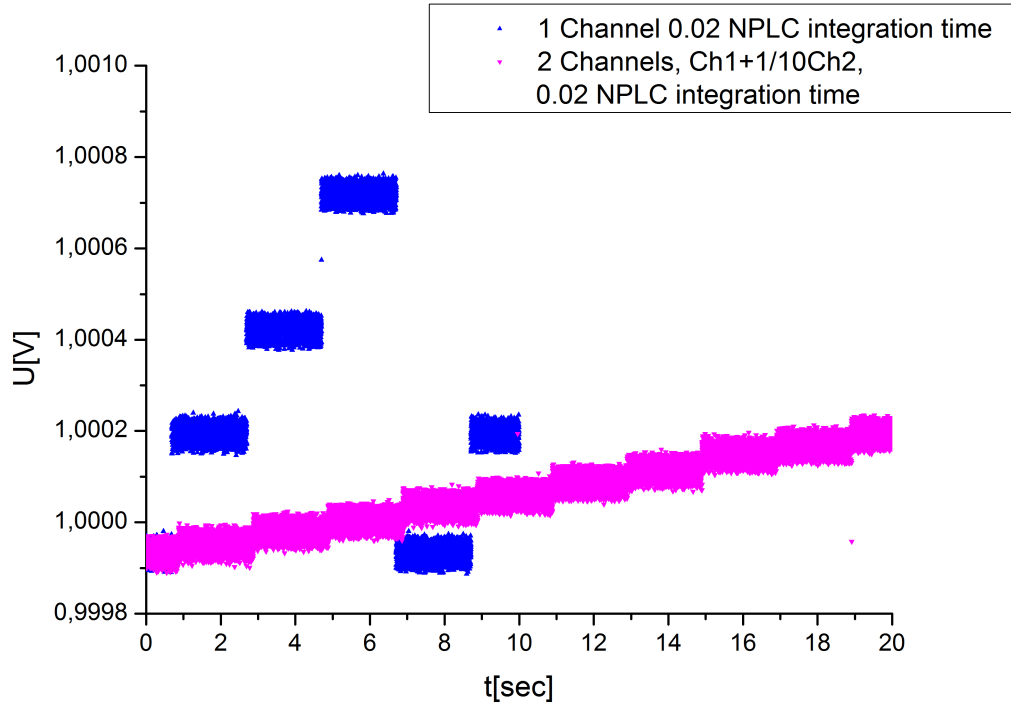


Figure 8.3.: Resolution of the AdWin 16bit analog output cards, blue being one single channel and pink two combined channels using a $\text{Channel} + 1/10 \text{ Channel}$ circuit with builtin 1kHz lowpass filter.

is realized as a software process on the AdWin realtime system and can be tuned with a programmable reference value and experimentally tested P,I,D settings. In fig. 8.4 we can see the frequency response for several P and I settings³, the system can suppress noise down to about an overall $\sigma = 0.2\text{mG}$ under ideal conditions on a test setup, there are several limitations however:

- The HMC2003 has a builtin 1kHz lowpass filter, on the experiment table we could not reach magnetic noise compensation beyond 300Hz.
- Furthermore the noise can only be suppressed to $\sigma = 0.25\text{mG}$ on the main experiment setup which we attribute to cable crosstalk.
- The High-Finesse power supply has a bandwidth of about 3kHz which is lower than the stated specification but should not limit us before the HMC2003 lowpass.

Further considerations have to be taken for the placement of the sensor inside our compensation coil setup to reach optimal operation of the system. Ideally we would like to have the sensor as close to the actual atoms as possible - which we cannot do because we would have to place it inside the vacuum for that. Further complications arise from our magnetic transfer system: too strong magnetic fields disorient the sensor and could permanently damage it. A compromise is to find a position which is not affected too strong from the magnetic transfer system but still provides good agreement of the fields at the atoms site. In fig. 8.5 a simulation of the magnetic field difference dependent on sensor placement is shown and has been calculated by:

$$B1(I1, x, y, z) - B2(I2, x, y, z) \quad (8.14)$$

with I1 and I2 chosen such that:

$$B1(I1, 0, 0, 0) = 2G \quad (8.15)$$

$$B2(I2, 0, 0, 0) = (2 + 10 \cdot 10^{-5})G \quad (8.16)$$

for the evaluation of the plot we set z to 4.1cm, y to 0cm and vary x (which is perpendicular to the magnetic transport). The 4.1cm for z were chosen due to spatial restrictions of optical access and for x we are limited to 6 – 7cm because of the thickness of the transport plate.

In fig. 8.6 is shown the effect of the magnetic transfer on the chip at the peak moments for several nearby transport-coil combinations. Only the maximum curve is of interest for a given position, which is for accessible regions only the top brown one. As the placement of our sensor is already quite restricted due to the mentioned requirements it is good to see that for the previously chosen position the expected field strengths are not extraordinarily high. We still need to perform a set/reset⁴ procedure to realign the magnetic susceptible components of the sensor each time before using the locking. If

³We normally keep D to zero as it normally worsens the stabilization at other values.

⁴Described in a supplemental manual from Honeywell[37]

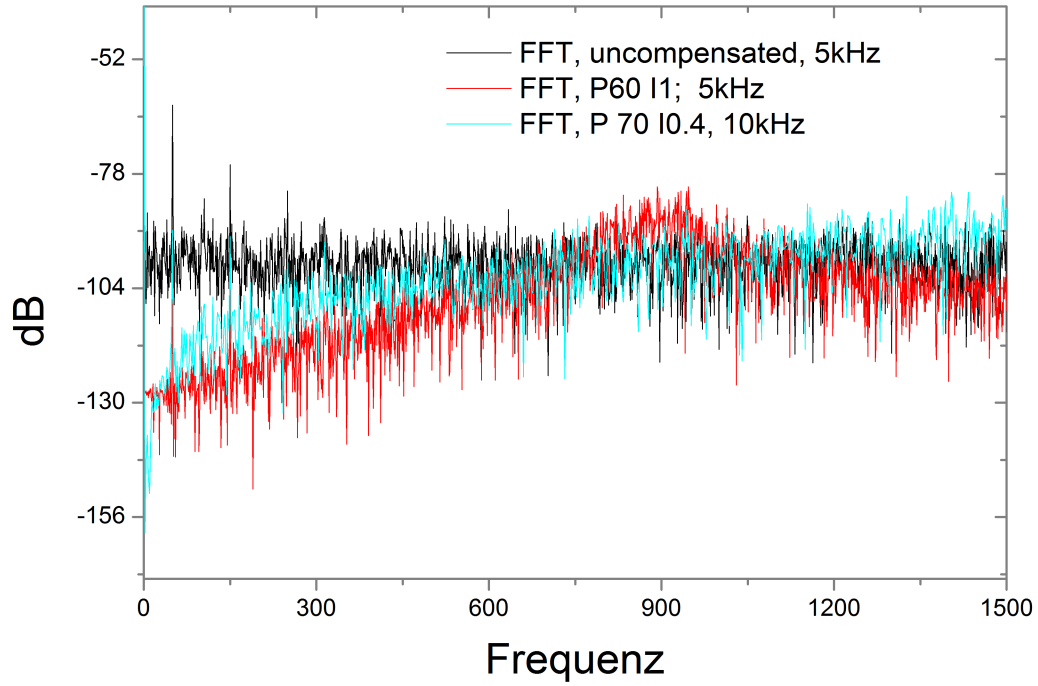


Figure 8.4.: Frequency response of the magnetic noise compensation loop: the black line represents the uncompensated background while the red and cyan settings show two attempts with different P,I and sampling speeds. The 10kHz sampling speed has an overall worse performance as the sampled voltages from the sensor are not sufficient to reach the required accuracy. Furthermore we see an increase in noise around 900Hz and beyond which we can attribute to the 1kHz low-pass filter in the magnetic field sensor.

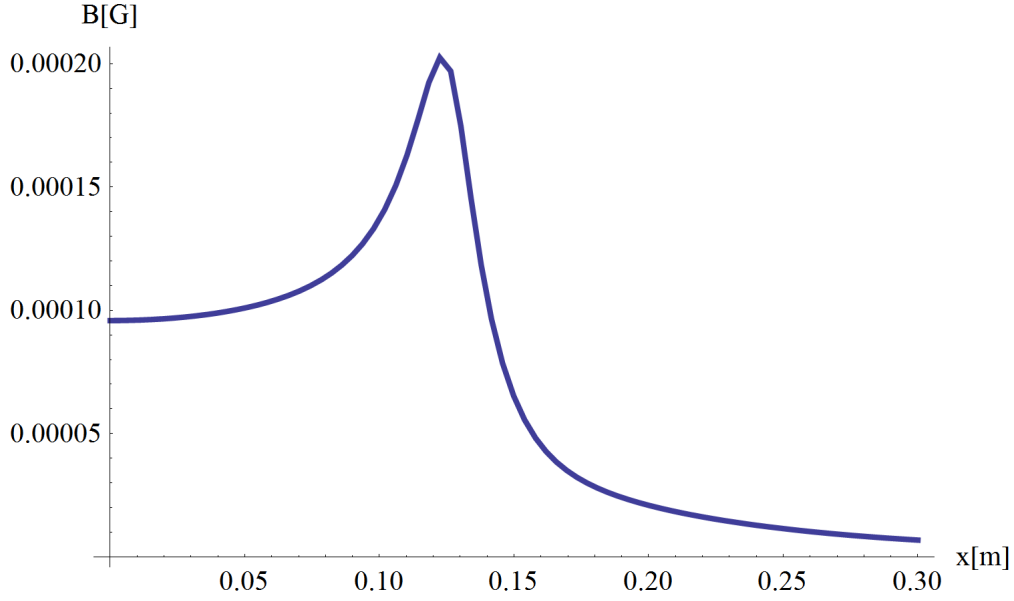


Figure 8.5.: Simulation of the deviation of the magnetic field on the 0.1mG scale depending on the position of the sensor displaced along x (or y) axis, whereas the z axis is displaced 4.1cm due to spatial restrictions in the setup.

one neglects the set/reset procedure there can be an offset to the field strength and in the worst case the orientation of the sensor axis has been flipped from the magnetic transport which leads the locking circuit to drive the power supply to its maximum power because the signal is interpreted with the wrong sign and cannot lock at all.

8.3. Gradient coils

8.3.1. Side coils revisited

To suppress the second order tunneling well beneath the fourth order tunneling it is necessary to provide a magnetic field gradient on the order of 60-70G/cm as mentioned in section 8.1.3 which should be tunable in diagonal direction. We use the same coil setup as in section 7.2.1 and are able to create gradients on the order of 100 – 125 G/cm along the diagonal direction, should need arise we could even double the amount of layers by using the ones which were reserved for additional offset fields. From fig. 8.7 we can deduce that actually only one specific diagonal direction will be usable to generate the high magnetic field gradient: two diagonals have permissively high current requirements which would most likely destroy the coils due to heat production and one of the solutions which are in the 10A range actually require the trap coil to run a negative current which is not possible with our setup.

To evaluate the homogeneity of the gradient it is instructive to at least plot the

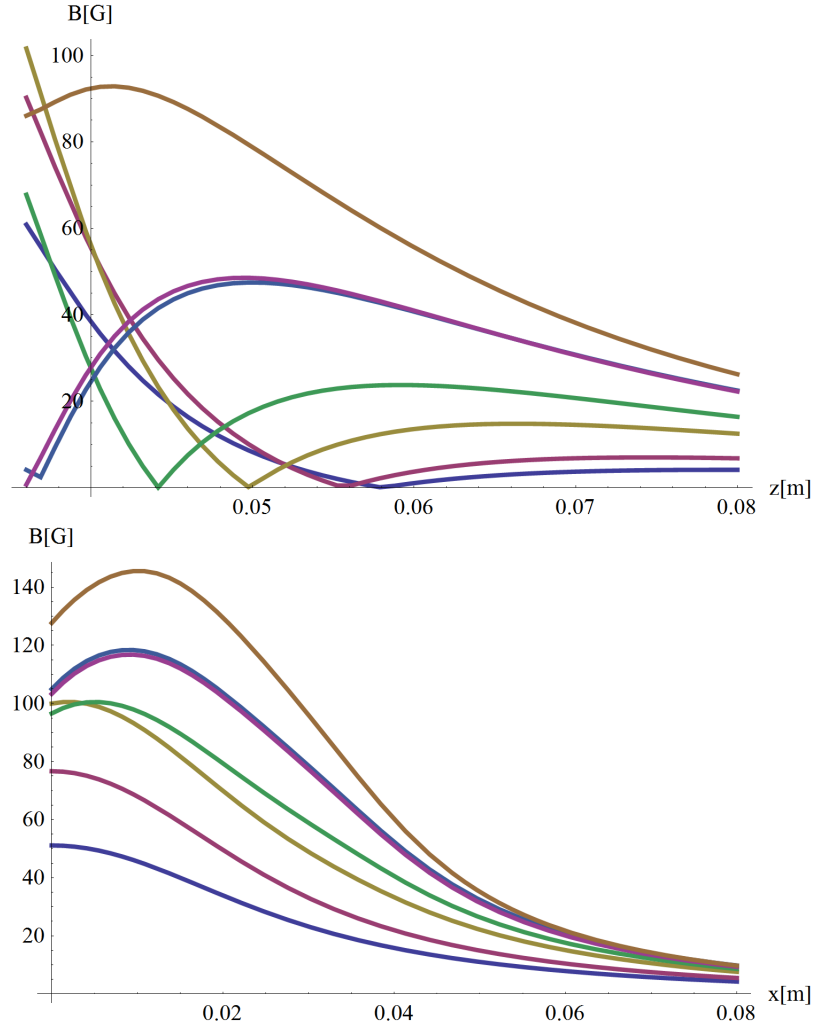


Figure 8.6.: Simulation of the magnetic field strength at the peak currents for all nearby transport coil configurations. In the upper plot we keep x and y fixed and only vary the height of the chip. The lower plot shows the field strengths for a height of 4.1cm and varying distance to the side of the track.

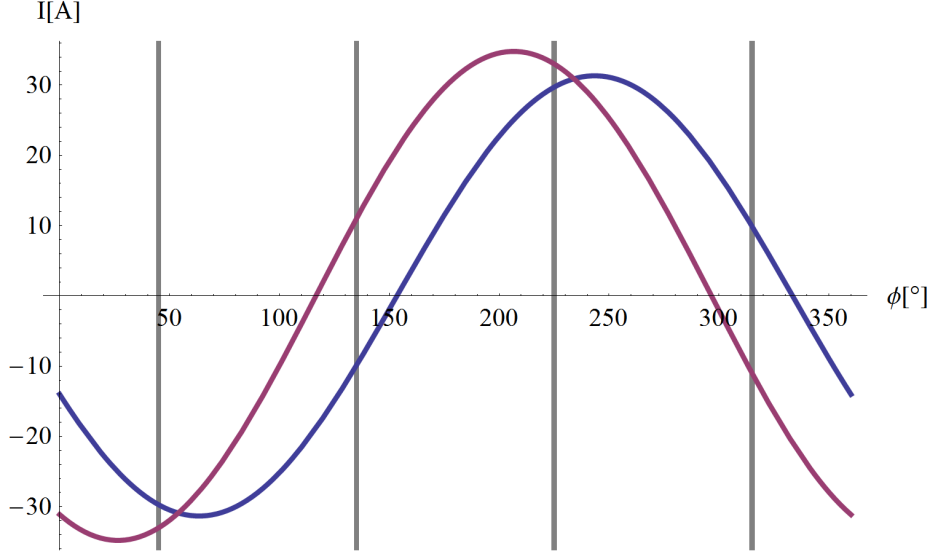


Figure 8.7.: Required currents to generate a gradient field of 125G/cm pointing in a direction given by ϕ with our set of coils using 4 layers of the 8 available of the sidecoil, blue being the current for the trap and purple for the sidecoils.

vector components of both field and gradient of the setup for the three main axes cross-sections once and it is also easy to spot any errors if one mixes up any coordinate back-transformation axes. If those look correct it is normally enough to compare four corners of a square - we chose 25 lattice sites to the left/right and top/bottom. One should check for both angle and magnitude of the chosen spots and as our atoms will sit approximately $90\mu\text{m}$ under the center of the trap we cannot expect symmetry for the four corners. Nonetheless the values should be quite close to each other which is required to get comparable results between individual plaquettes and is also true because we are still very close to the center of the coils and the involved distances are small compared to the coils' size.

For comparison, the magnetic field gradients at the four corners are:

Lattice #	$X = -25$	$X = 25$
$Y = -25$	(88.388 (x), -88.389 (y)) G/cm	(88.388 (x), -88.389 (y)) G/cm
$Y = 25$	(88.389 (x), -88.388 (y)) G/cm	(88.389 (x), -88.388 (z)) G/cm

where the real distance can be calculated by multiplying the Lattice number with $\lambda/2$ (for our case of the 1534nm lattice this is 767nm). We also investigated the ramping speeds of our gradient coils and compared those with the Larmor frequency:

$$\omega = \frac{eg|\mathbf{B}(t)|}{2m} \quad (8.17)$$

to avoid losses due to Majorana spin flips we should stay below this frequency when

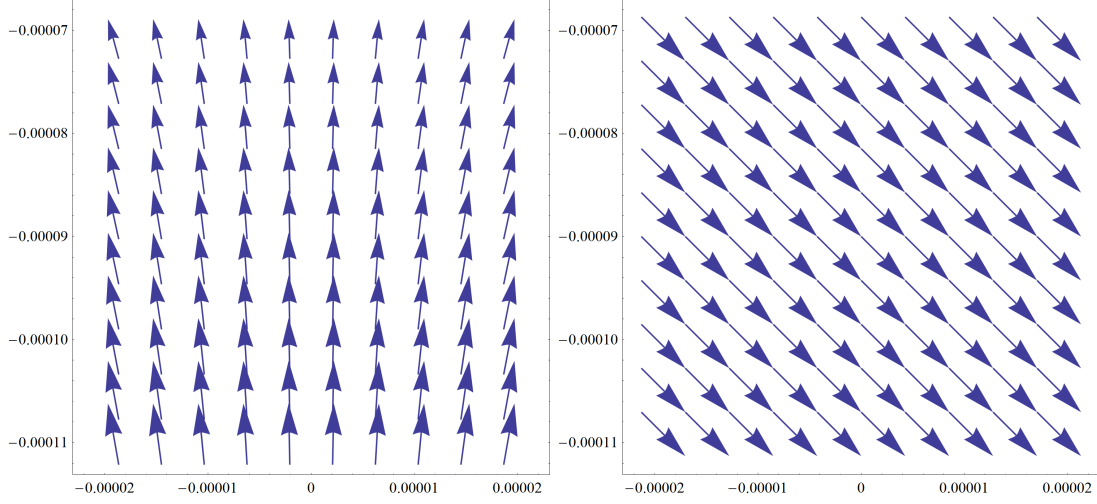


Figure 8.8.: a) Magnetic field of the gradient coils, x/z axes cross-section. b) Magnetic field gradient of picture a), units are in $[m]$ and correspond to an area of -25 to $+25$ lattice sites, the gradient in this area can be seen as homogeneous.

we rotate our magnetic field to the 45° direction. A simulation which compares the magnetic field direction rotation frequency with the Larmor frequency can be seen in fig. 8.9 which was carried out for the following parameters:

- Magnetic field ramped from 0 to 125G.
- Trap current linearly ramped from 0 to required current within $500\mu s$, linearly.
- X coil current ramped from 0 to required current with negative exponential function with $32\mu s$ timeconstant (from measurement).
- Initial offset magnetic field of 2G, linearly switched off over $500\mu s$.

as we can see there is a difference by a factor $> 10^2$ which should slow enough for the atoms to follow the magnetic field change.

8.3.2. MOSFET switch to change between one and two layered trap coil

An interesting possibility outlined by Selim Jochim was the idea to be able to switch our trap coil from a two layer (above and below the glass cell) operation mode into one layer mode. The magnetic field of a single coil will in our case have a smoother potential shape than in the two layer case, while the gradient of the two layer case is smoother and will perform better for such applications. A comparison of both magnetic fields and magnetic gradients for the two cases can be seen in fig. 8.10 and from a harmonic fit to the potentials we can estimate trap frequencies of $\omega = 2\pi \cdot 34.48\text{Hz}$ for the two-layer case and $\omega = 2\pi \cdot 2.94\text{Hz}$ for the one-layer case.

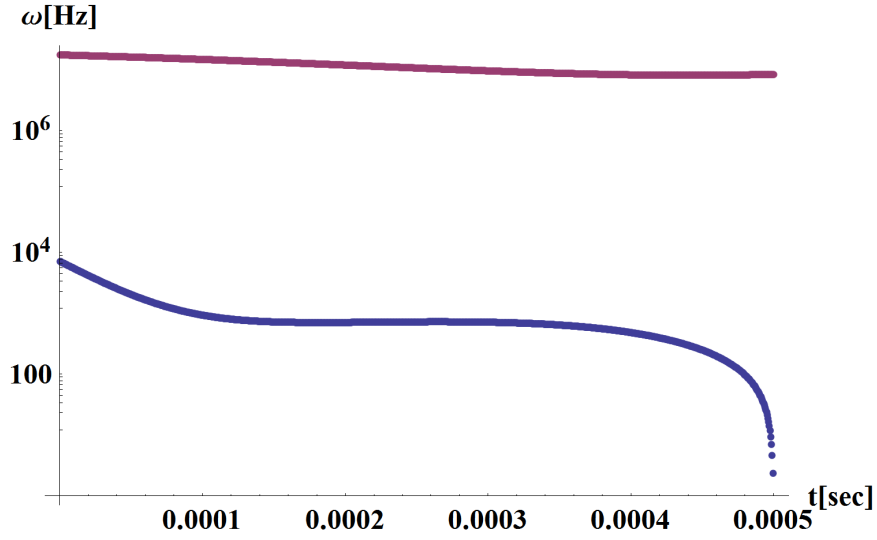


Figure 8.9.: Larmor frequency (purple) VS field direction rotation frequency (blue) over time.

We were kindly provided with designs for MOSFET switches and drivers from Gerhard Zürn of Selim's group which we could insert in between our power lines to be able to select either one or two layer operation as seen in fig. 8.11. The MOSFETs (IRFB 3077) are screwed to massive copper banks which are insulated from a base plate with kapton foil and by using only plastic screws; for additional security of overvoltages we use S20K20 varistors from Epcos which will protect the MOSFETs from overvoltages if the coils are being switched off fast.

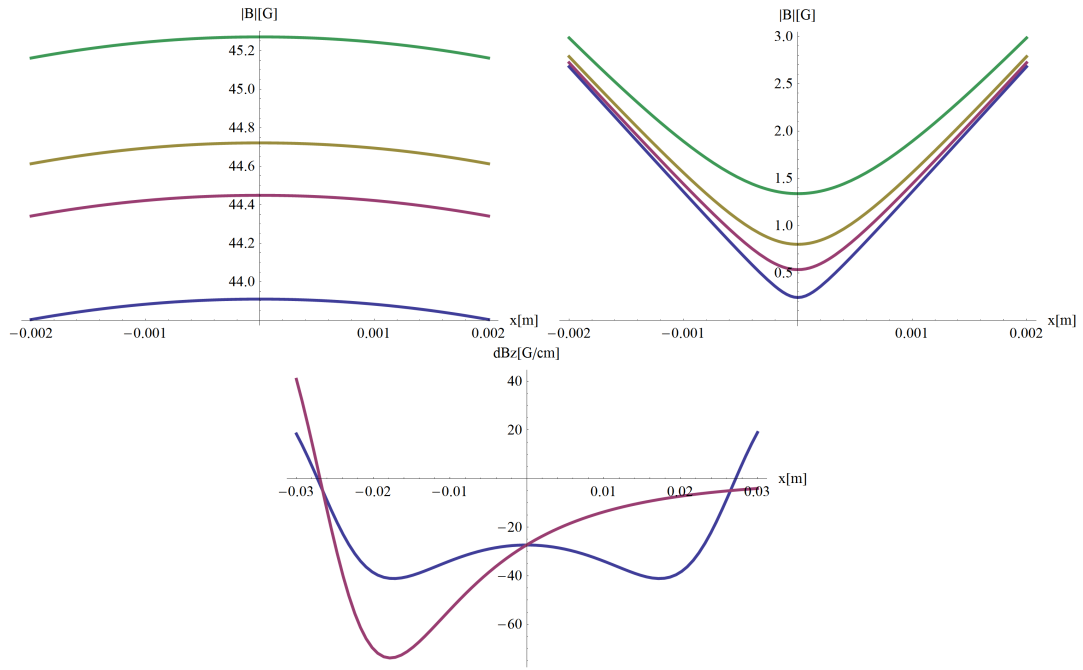


Figure 8.10.: Upper: magnetic field along x axis for z : blue: $-90\mu m$, purple: $-200\mu m$, brown: $-300\mu m$, green: $-500\mu m$ left: only one coil layer, right column: two coil layers. Lower: dB_z magnetic field gradient (dB_x , dB_y are the same for both cases) with blue being the two coil layers case and purple the one coil layer case.

9. Conclusion and outlook

We have shown improvements in the performance of quantum memories based on neutral atoms in blue detuned dipole traps over a previous experiment. While we could not achieve the desired storage time, we still have an increase compared to the red detuned dipole trap. We explained the observed oscillations in the retrieve efficiency using a semiclassical quantum-Monte Carlo method, which also explained the faster than anticipated decay. In the second part we reported on Bloch Oscillations on our optical lattice, in 1D and in 2D. In 2D we could not certainly distinguish if the observed transport phenomena are solely due to Bloch Oscillations. Furthermore we presented the steps which have been undertaken so far towards the Ring-Exchange experiment, the entanglement of 4 atoms in a GHZ state.

With the re-introduction of the high-resolution imaging system, fixing the position of the side-coils and using the motorized mounts for a more precise optimization of the lattice overlaps we should be able to obtain clearer results on the Bloch-Oscillations in 2D as well as starting the Ring-exchange experiment. The increased resolution should decrease the currently large errors on the center of mass measurements which would enable us to give a better answer on how long 2D Bloch Oscillation driven transport using Rubidium can be and the differences between individual current/magnetic field ramps should be separable.

One possibility to decrease the decoherence of the Bloch-Oscillations might be the already mentioned use of microwave/RF induced Feshbach resonances, e.g. described in [34, 43, 74]. In [34], figure 9a shows that the Feshbach resonance is quite narrow, and a useful region with decreased scattering length is about $< 10\text{mG}$ wide. It is clear that those Feshbach resonances would require very stable magnetic fields, and from the shown scale in [34] we can assume that it might be hard to reach values lower than $60a_0$, unless both magnetic field and frequency were extremely stable. Currently our magnetic field stabilization could not be locked to the required field strength in the 9G region either as it would require a very stable offset-current for the sensor as well. Further tests would then be required if this offset current would further degrade the currently achievable stability of 0.25mG which is likely due to increased crosstalk and offset-current noise.

For the Ring-exchange we anticipate to first qualitatively show the entanglement by selectively pumping atoms depending on their state and measuring the visibility as in [57]. A more sophisticated approach using an entanglement witness for this case of GHZ state still needs to be formulated in an experimentally feasible way. Because even though the proposed method is a good indication for entanglement in the system, it is only a necessary but not sufficient criterion.

A. AdWin two channel adder and lowpass filter

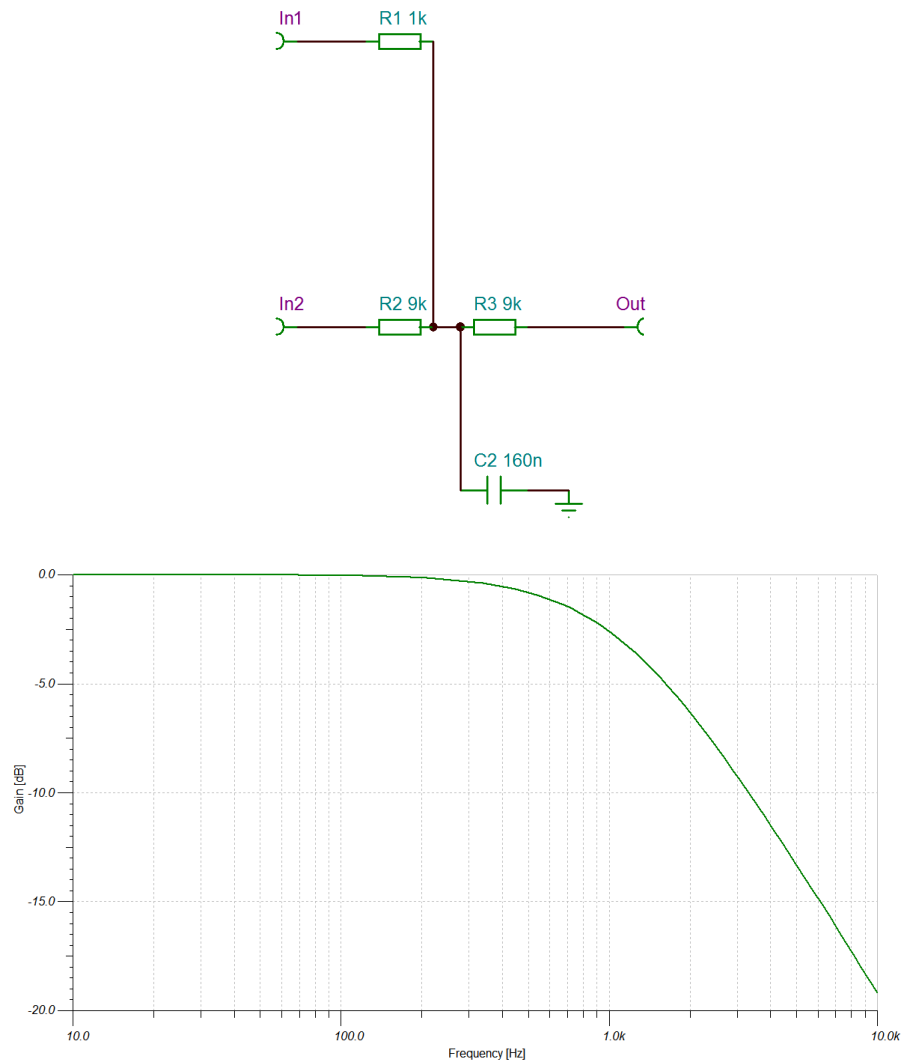


Figure A.1.: Circuit to add two channels where one is divided by roughly 10 (depends on tolerance of used resistors), including lowpass filter of 1kHz, frequency response simulated with TINA-TI.

C. New high resolution system mount

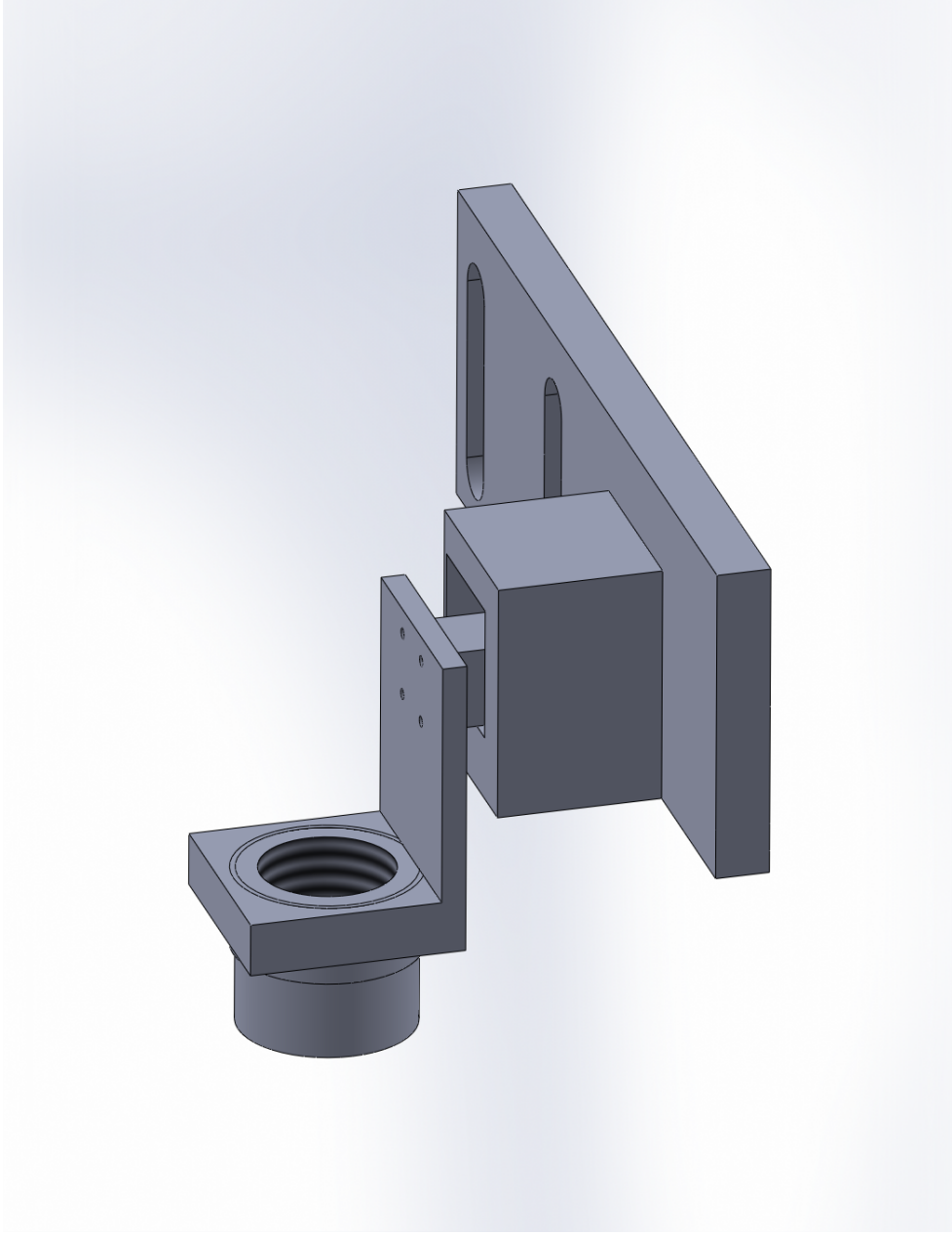
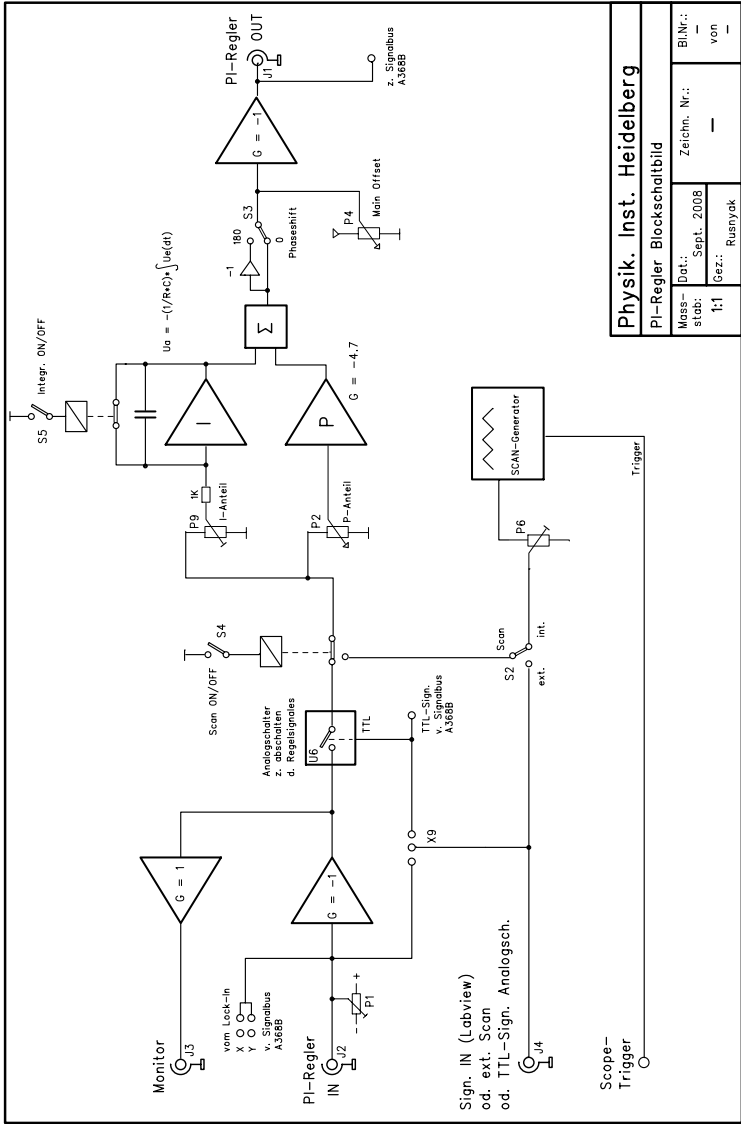


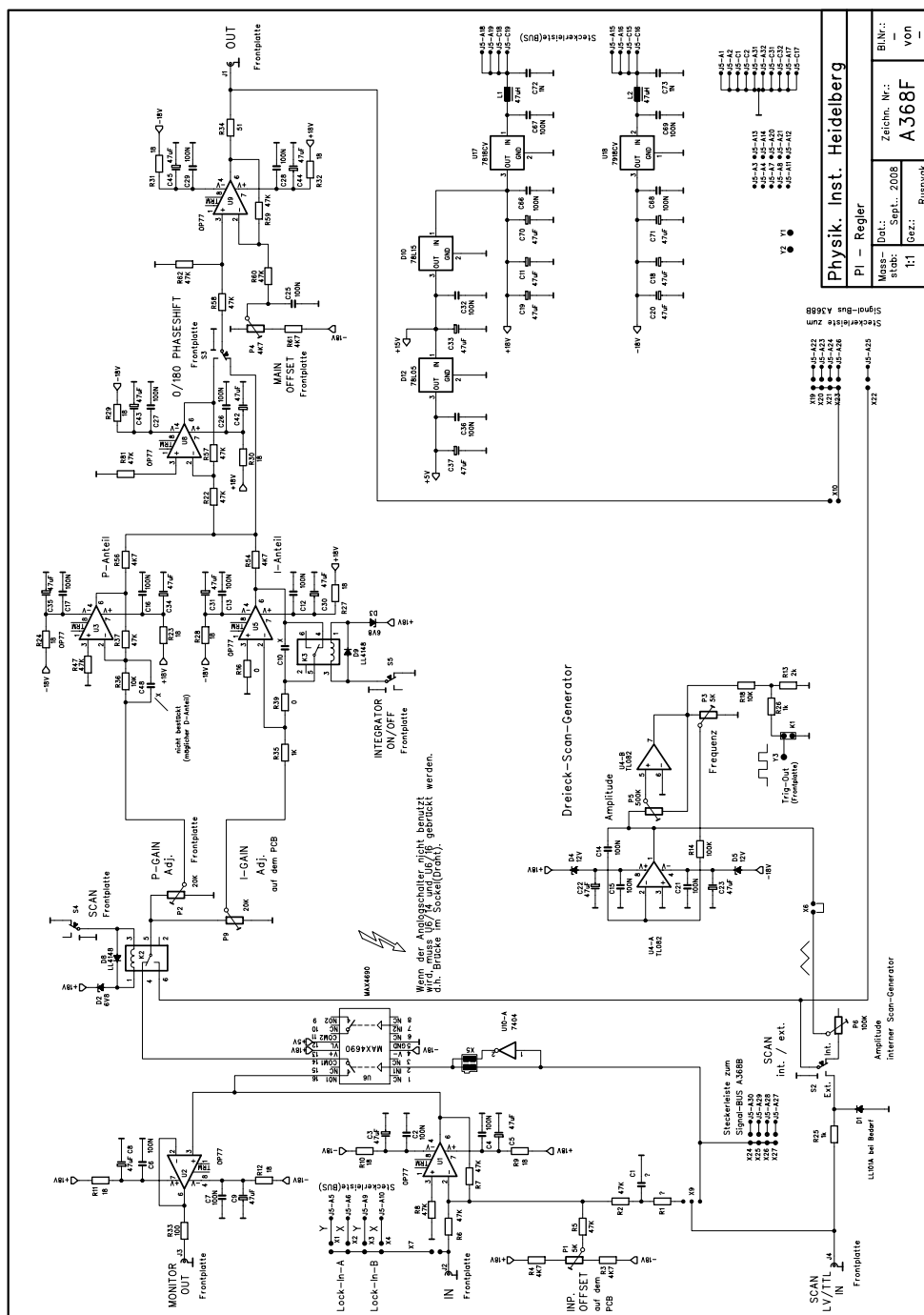
Figure C.1.: The new translation stage and mount of the high resolution imaging system.

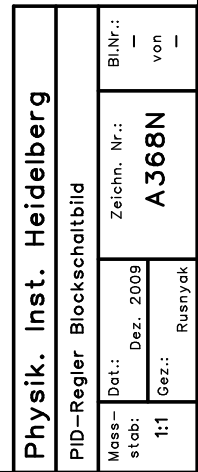
D. N368-E,F,G,N: FM, FO-locks and PID cards

Circuit drawings provided by the Elektronische Werkstatt des Physikalischen Instituts on behalf of Mr. Schumacher.

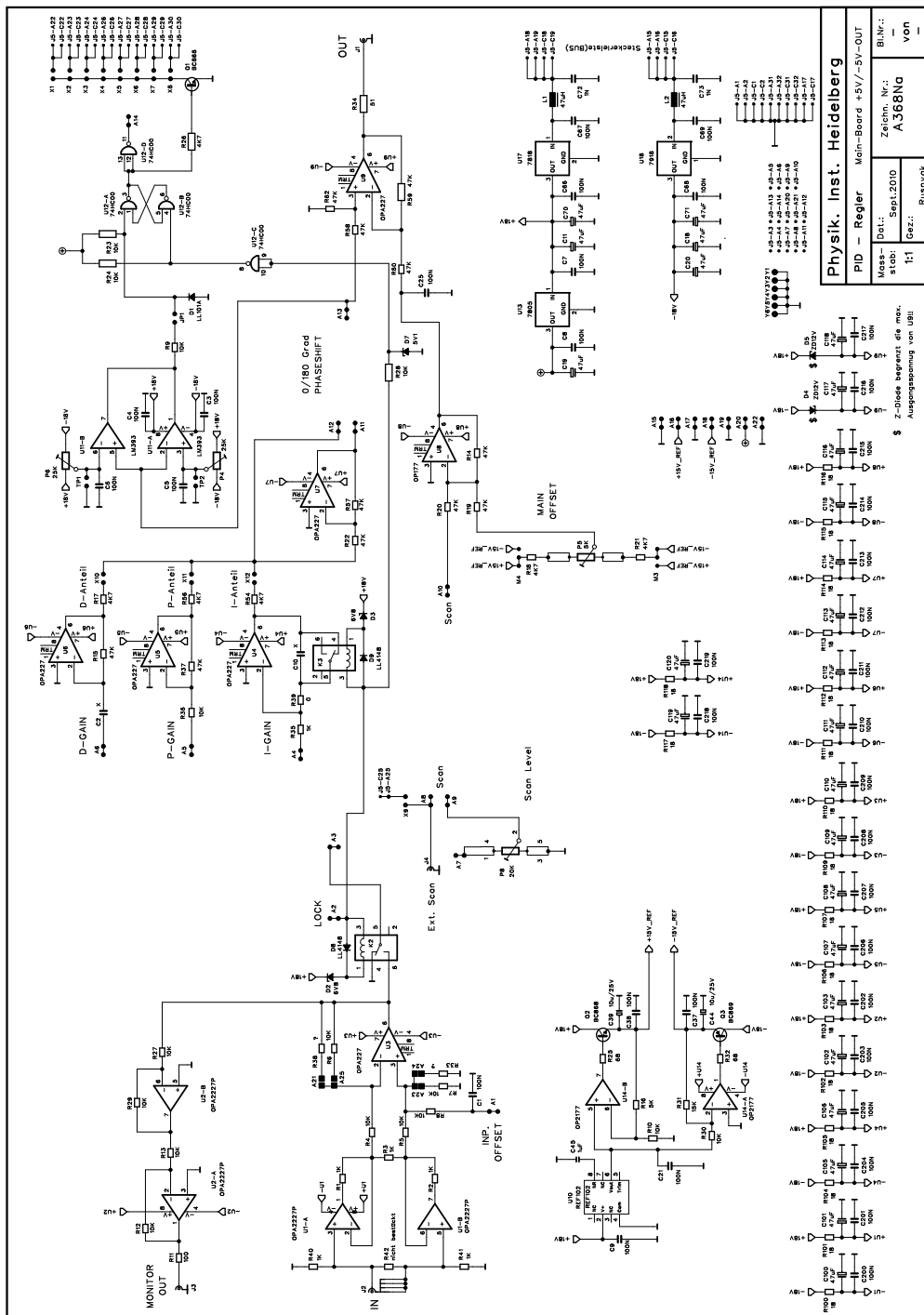


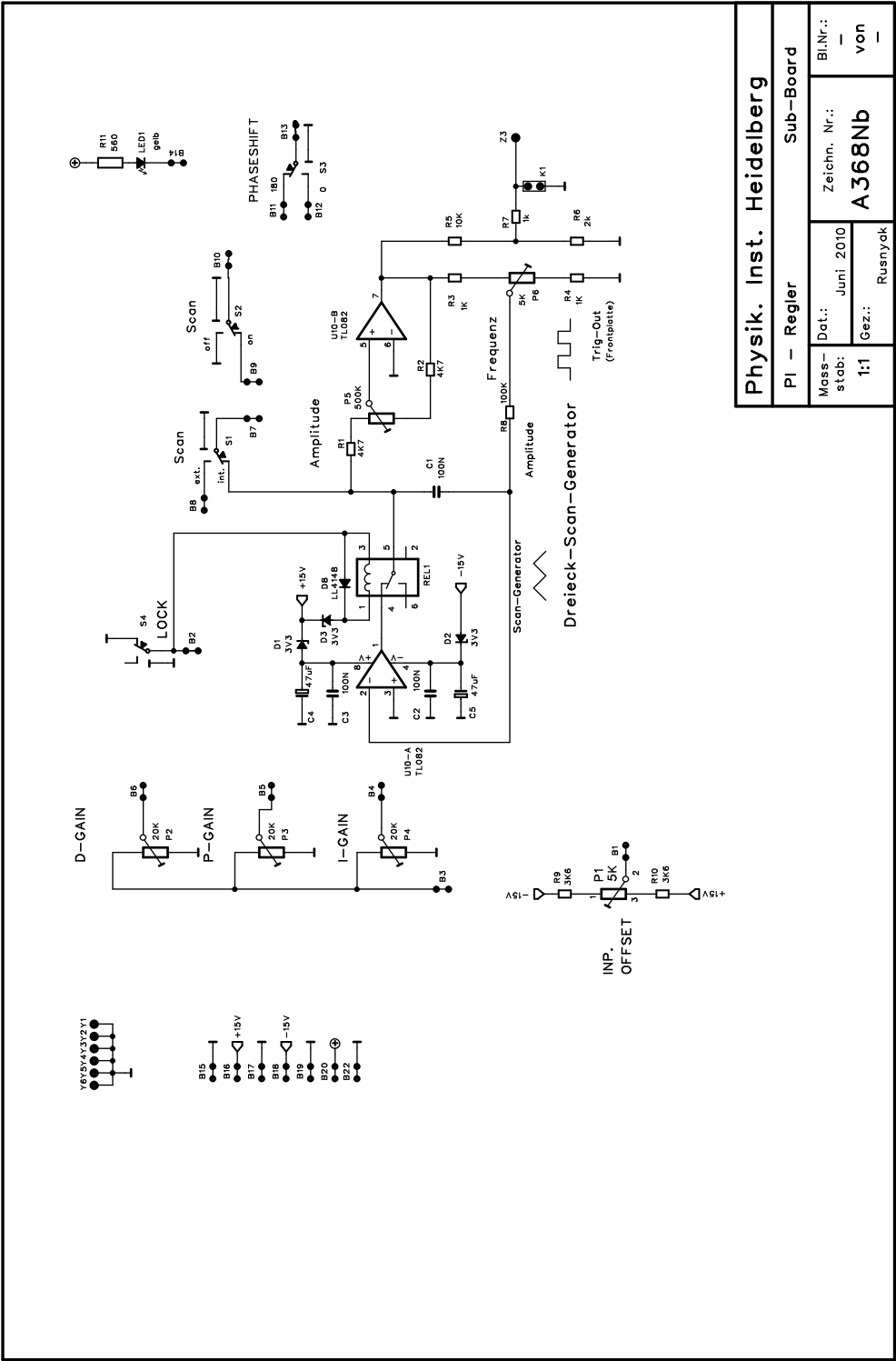
8.3. Gradient coils

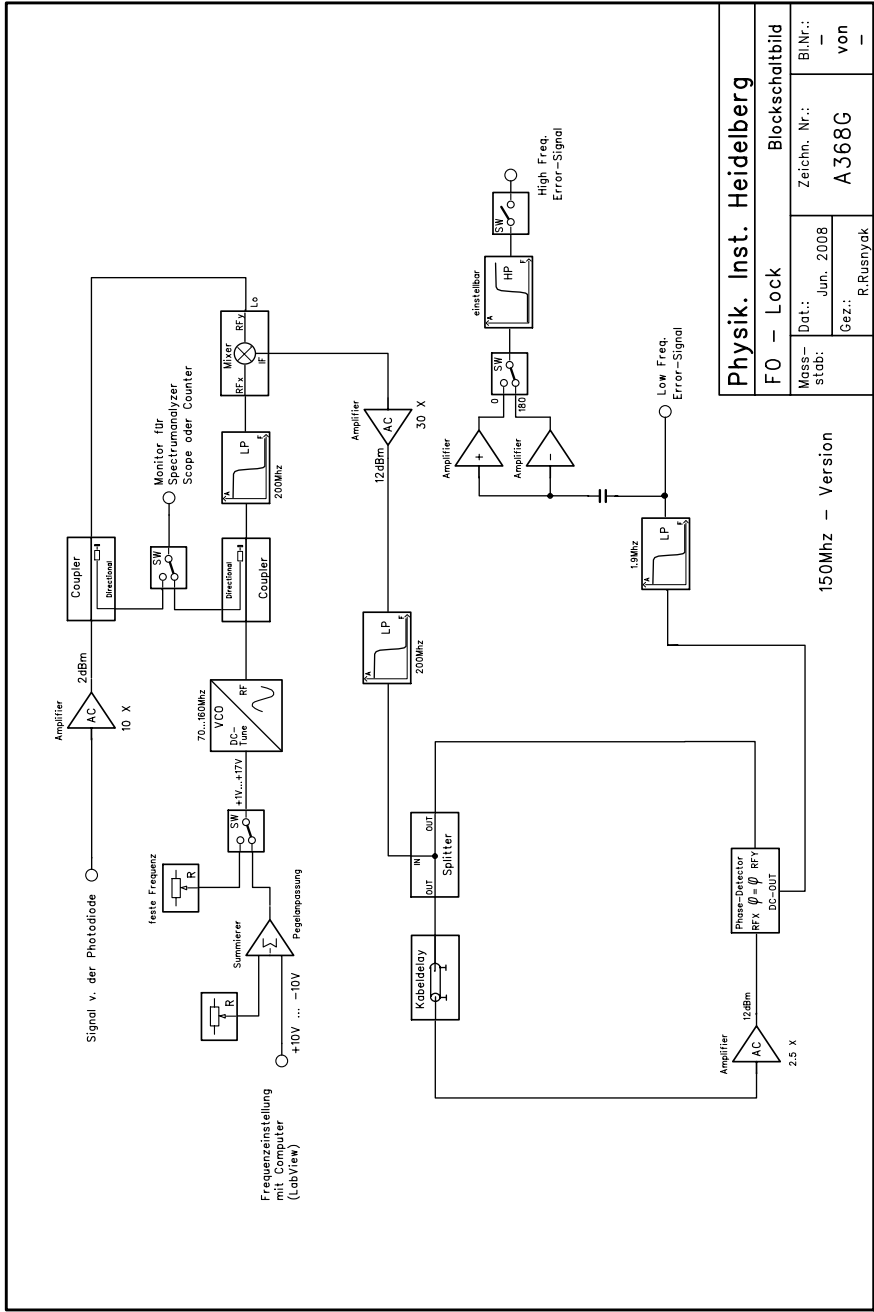




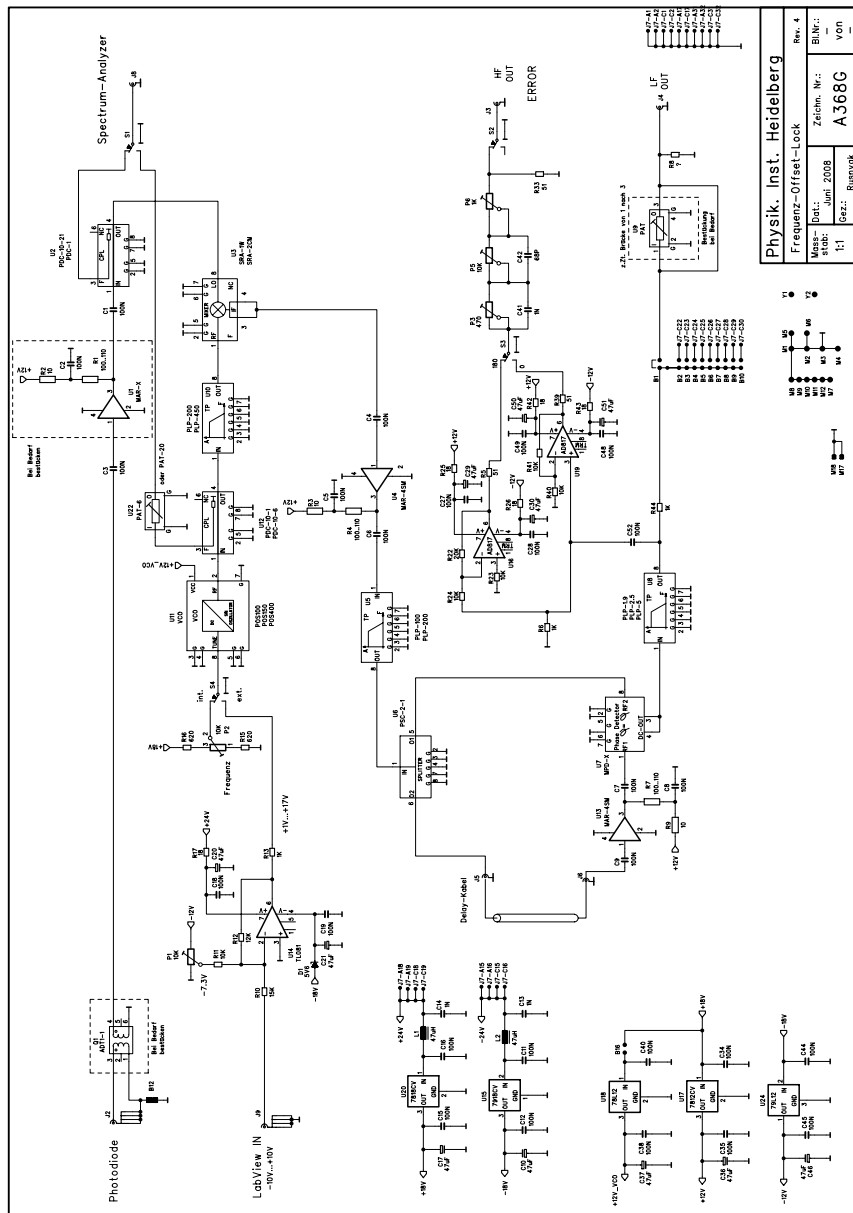
8.3. Gradient coils



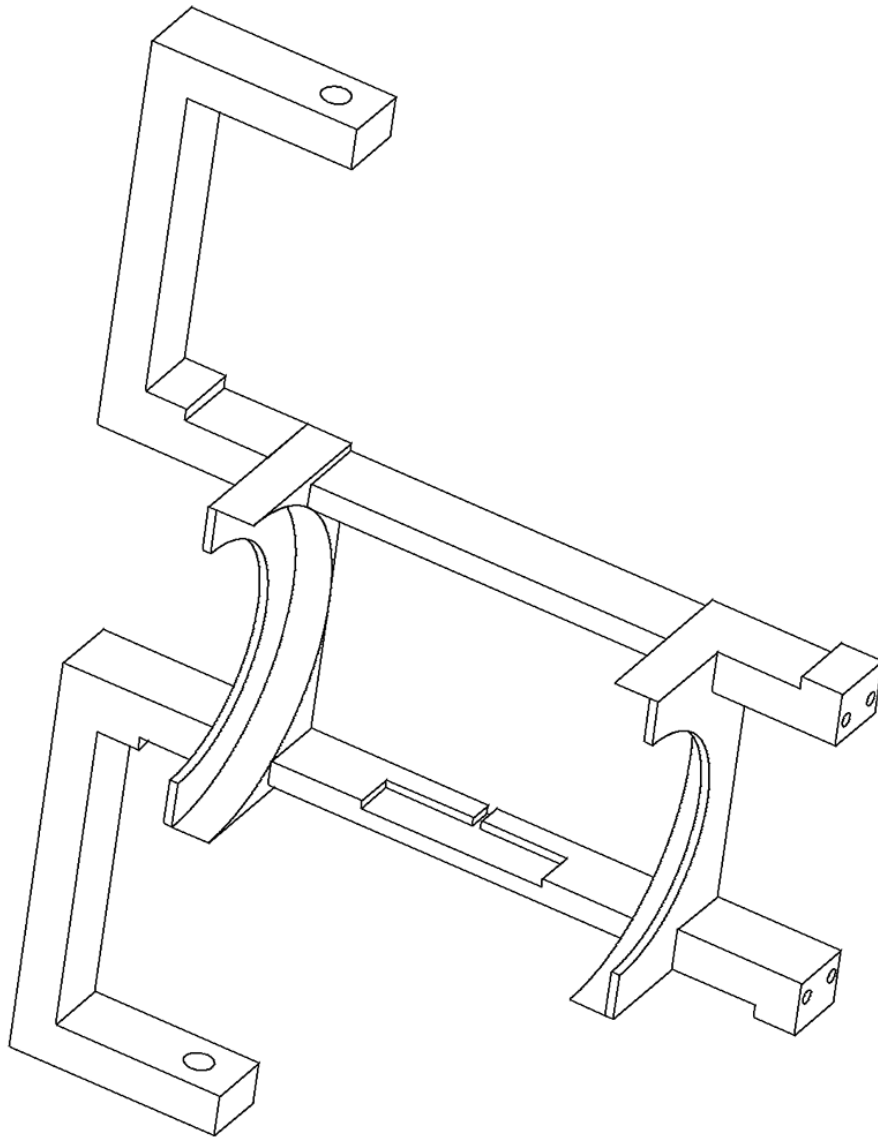




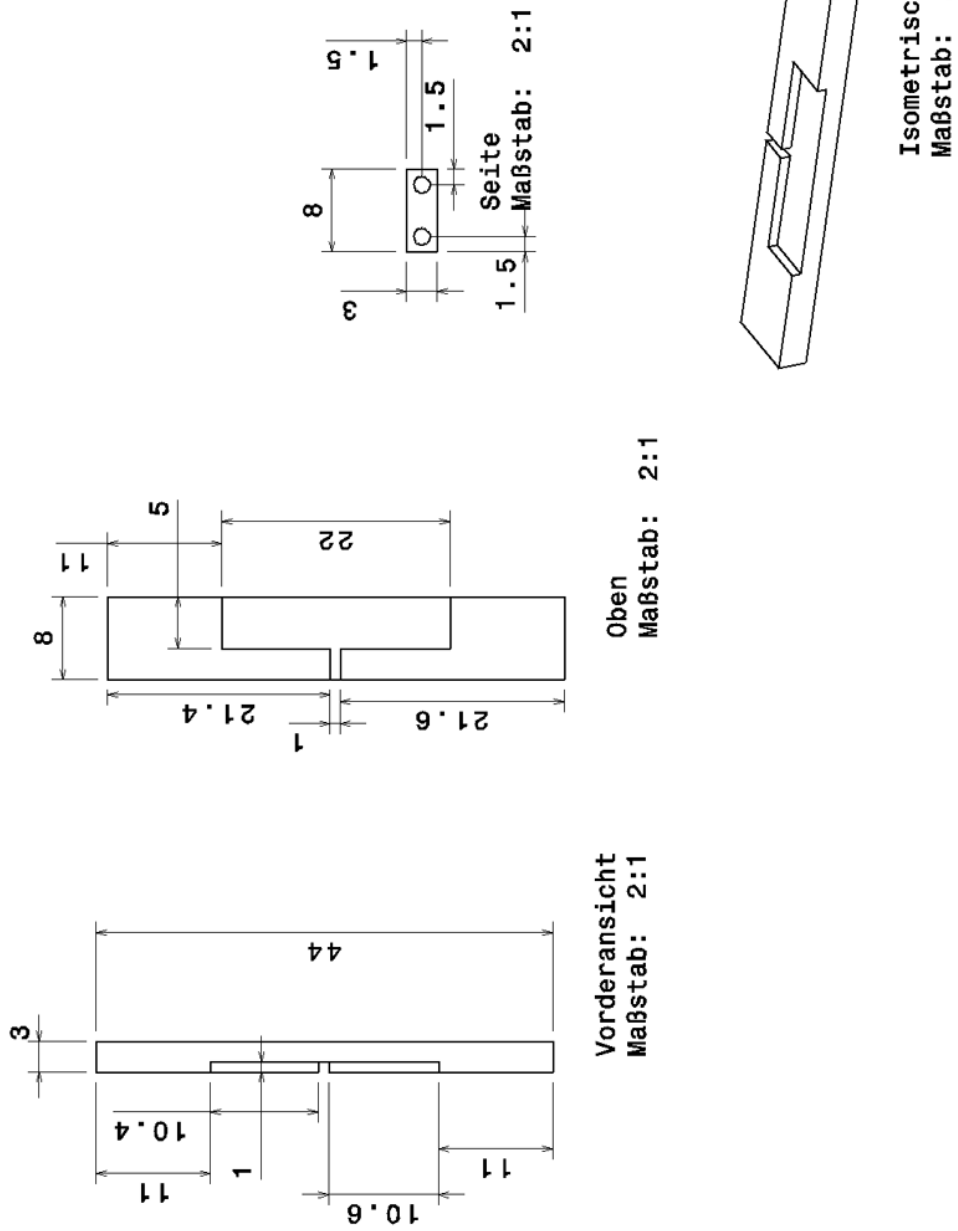
8.3. Gradient coils

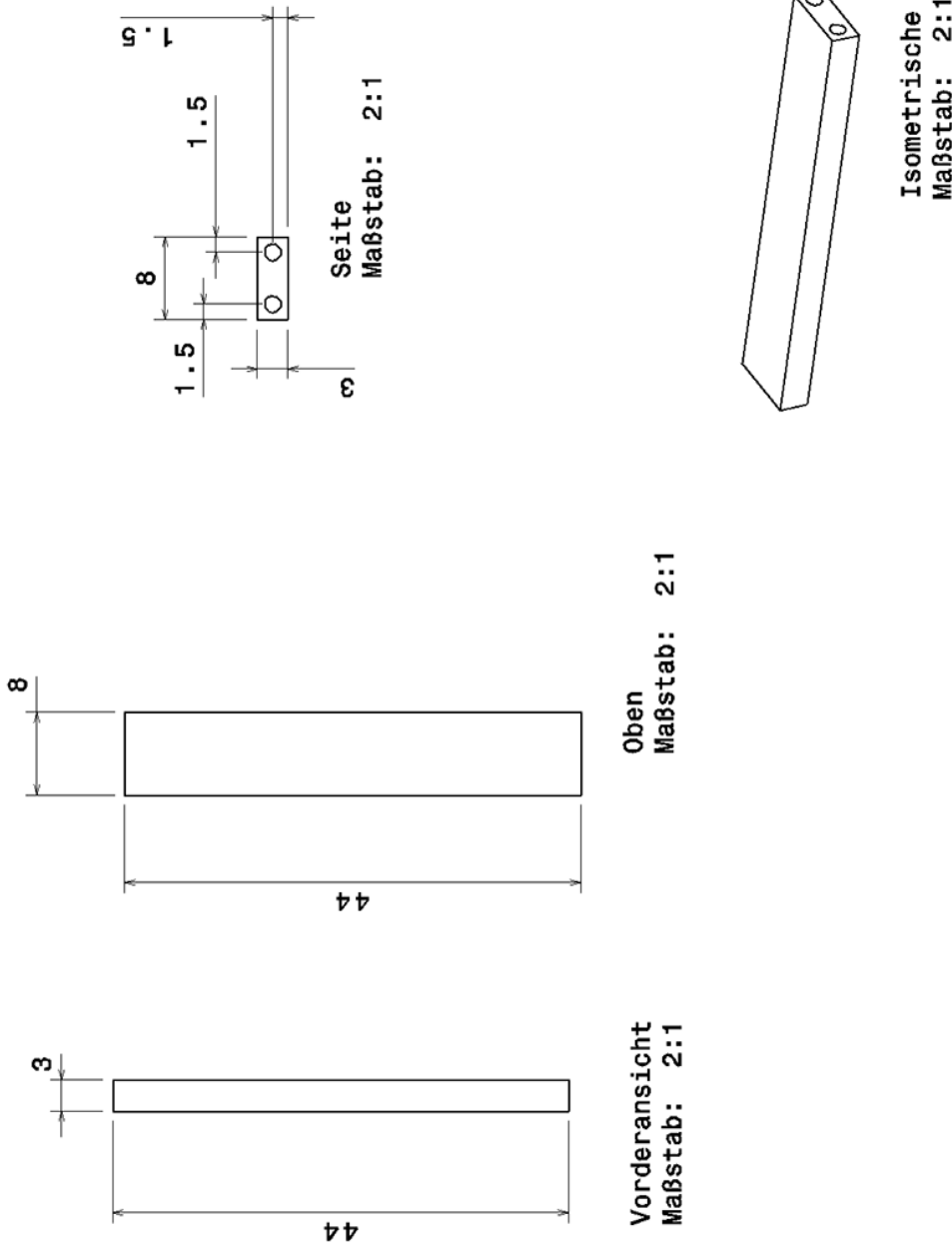


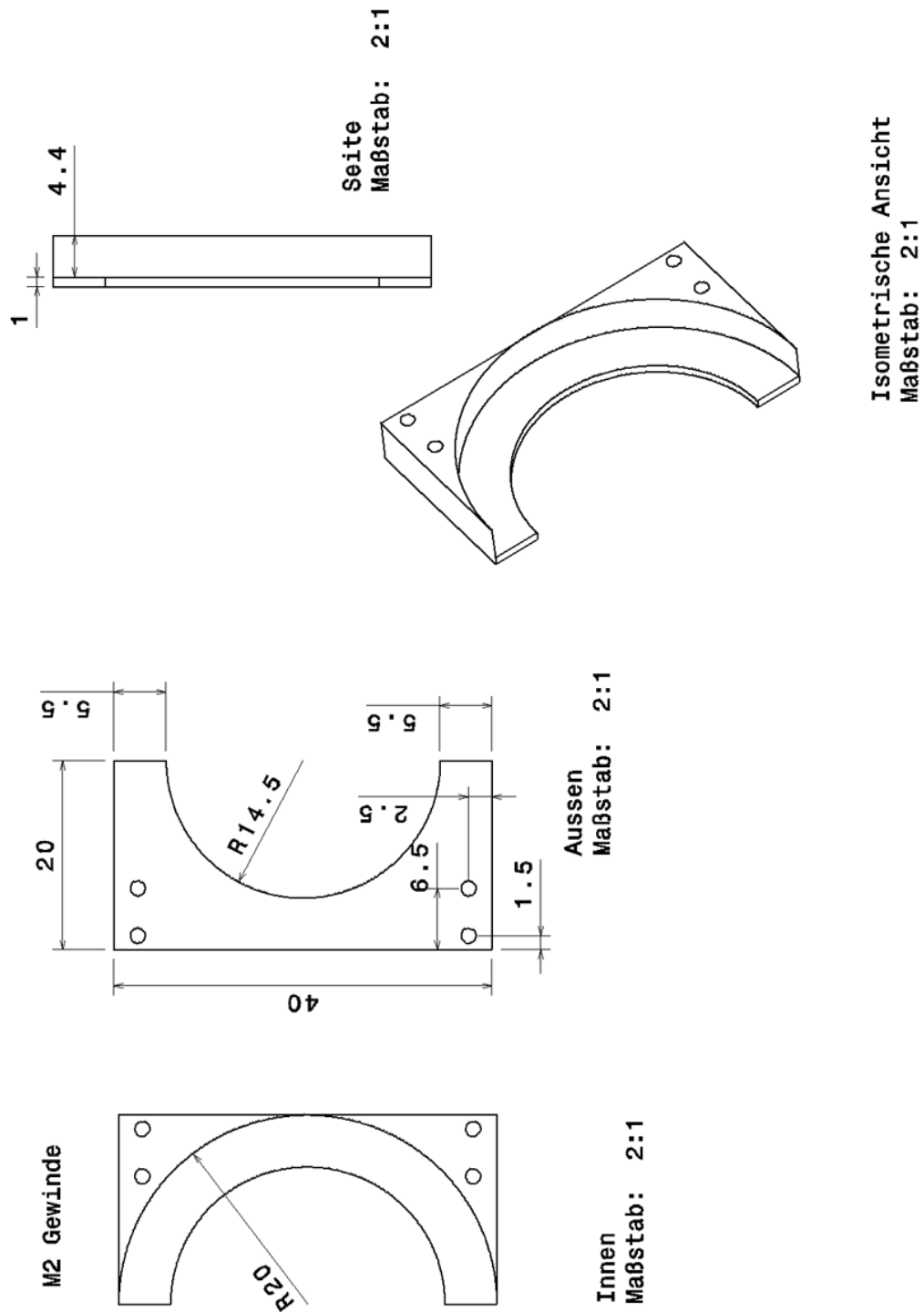
E. Side-coils holding frame

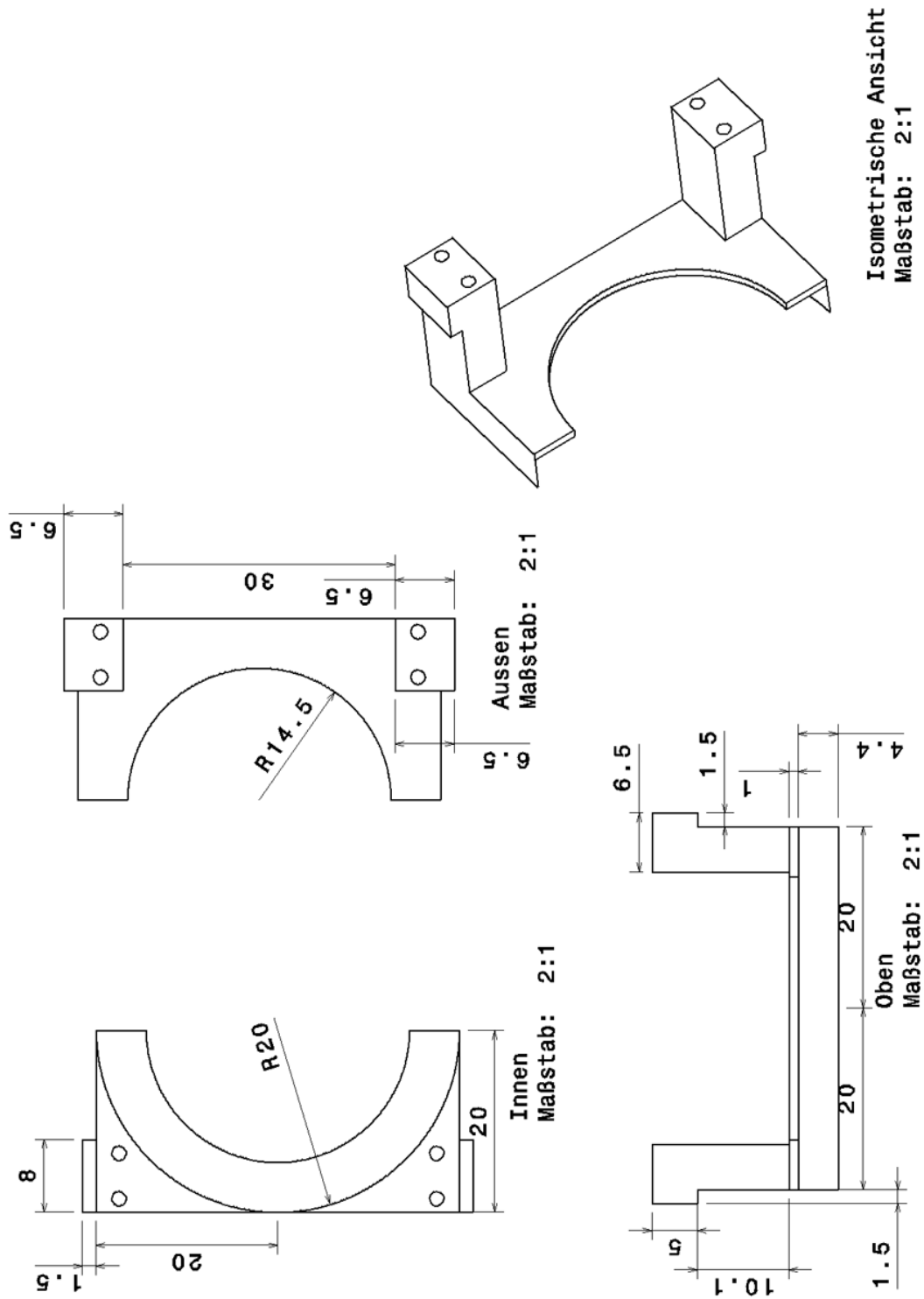


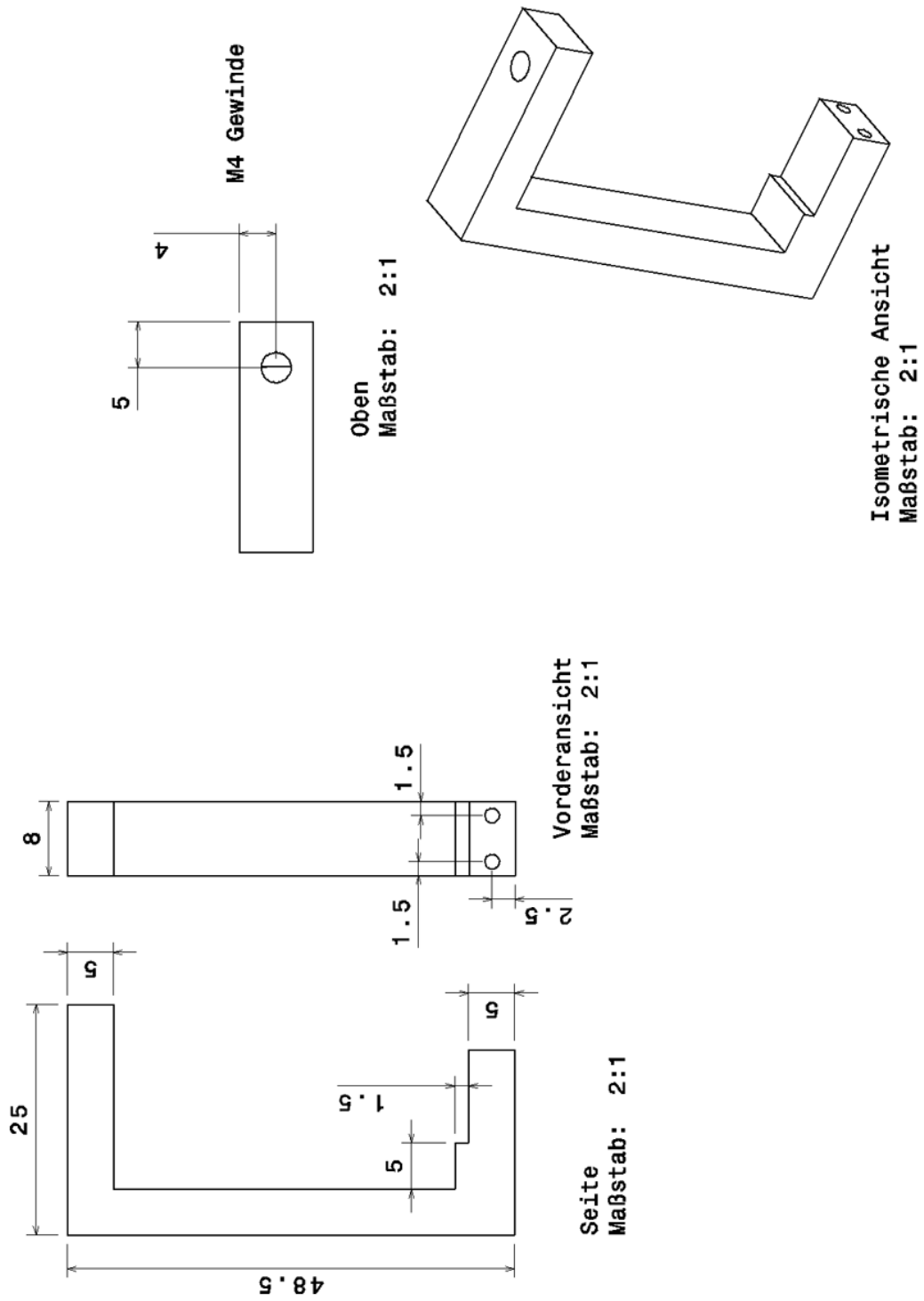
Isometrische Ansicht
Maßstab: 2:1

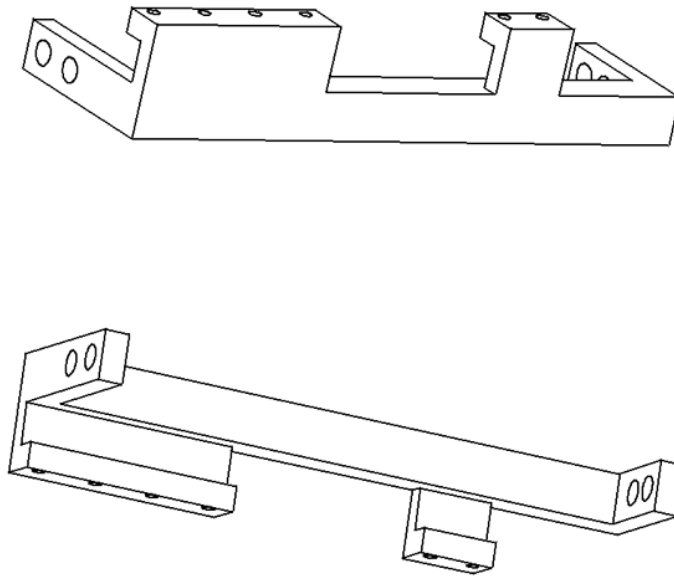
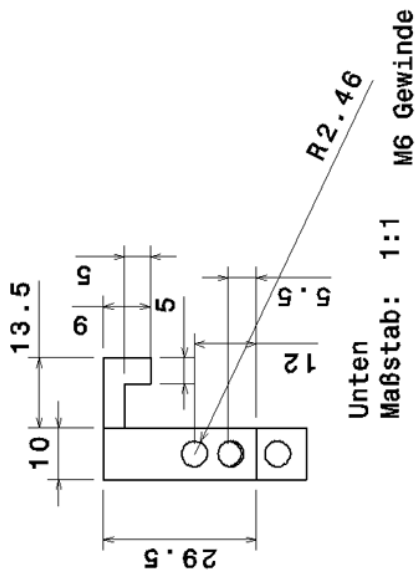






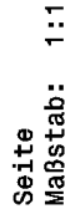






Isometrische Ansicht
Maßstab: 1:1

Isometrische Ansicht
Maßstab: 1:1



F. Acknowledgements

Prof. Dr. Jian-Wei Pan for supervising my thesis and enabling me to work in the interesting fields of quantum memories and ultracold atoms.

Prof. Dr. Zhensheng Yuan for supervising my thesis as well, planning, organizing and helping with our experiments, interesting discussions, all the support throughout the years and proofreading/suggestions to my thesis.

Prof. Dr. Selim Jochim for refereeing this thesis and interesting discussions.

Prof. Dr. Thomas Gasenzer and PD Dr. Jörg Evers for participating in my thesis defense.

My team members, Hanning Dai, Andreas Reingruber, Xiaofan Xu and Bing Yang; whereof I'd like to thank each of you for something in particular, even though I'll have to keep the list shorter than it deserves: Hanning for the help with many theoretical calculations and help in the lab, Andi for the excellent organization of the lab move, the new lab construction and proofreading this thesis, Xiaofan for his many optical/electrical setups and help with the system (even though the most funny thing probably was our disassembly of the racks) and Bing for the help with the magnetic compensation and high resolution imaging tests.

Our former team members Huan Nguyen and Christian Lutz for the great work on our setups.

The mechanical workshop, in particular Mr. Ziegler for the many realized designs and great help during the move of our institute, Ms. Riedinger and Mr. Rabenecker for the precisely produced coils, Mr. Haaf for the help with our accounting, Mr. Muley for our cooling plates.

The electronic workshop, in particular Mr. von Walter, Mr. Angelov and Esteban Rubio for the Logic Box and support thereof, Klaus Layer for our high current power supplies and associated repairs, tests and Mr. Schumacher for many repaired items as well as provided circuit drawings, Mr. Mallok and Steffen Brucker for ordered equipment and accounting.

Gerhard Zürn for the MOSFET switch system.

Shannon Whitlock for the fringe removal algorithm.

The Weidemüller groups for lending equipment (especially their nice magnetic field sensor!) and being able to use their electronical workshop.

The secretaries: Ms. Weidinger and Ms. Zeberer for help with ordering tools as well with accounting, Ms. Pachomowa for accounting and Ms. Schmidt and Wallenwein for organizational matters.

To my family and friends for support and all the fun throughout the years.

To my boyfriend Sascha for his love, support and great patience.

Bibliography

- [1] ABRAMOWITZ, AND STEGUN. *Handbook of Mathematical Functions*. 1972.
- [2] ALBERTI, A., IVANOV, V. V., TINO, G. M., AND FERRARI, G. Engineering the quantum transport of atomic wavefunctions over macroscopic distances. *Nature Physics* 5, 8 (June 2009), 547–550.
- [3] ANDERSON, P. W. The Resonating Valence Bond State in La₂CuO₄ and Superconductivity. *Science (New York, N.Y.)* 235, 4793 (Mar. 1987), 1196–8.
- [4] BAGNATO, V., PRITCHARD, D., AND KLEPPNER, D. Bose-Einstein condensation in an external potential. *Physical Review A* (1987).
- [5] BELANGER, P.-A., AND RIOUX, M. Ring pattern of a lens-axicon doublet illuminated by a Gaussian beam. *Appl Opt.* 17, 7 (1978), 1080–1086.
- [6] BELL, J. S. On the Einstein-Podolsky-Rosen paradox. *Physics* 1, 3 (1964), 195–200.
- [7] BENNETT, C. H., AND BRASSARD, G. Quantum Cryptography: Public key distribution and coin tossing. *IEEE International Conference on Computers, Systems and Signal Processing* (1984), 175.
- [8] BLOCH, F. Über die Quantenmechanik der Elektronen in Kristallgittern. *Zeitschrift für Physik* 52, 7-8 (1929), 555–600.
- [9] BOWMAN, R. W., WRIGHT, A. J., AND PADGETT, M. J. An SLM-based Shack-Hartmann wavefront sensor for aberration correction in optical tweezers. *J. Opt.* 12 (2010).
- [10] DAI, H.-N. *Quantum Information Processing with Cold Atoms*. PhD thesis, 2013.
- [11] DALFOVO, F., GIORGINI, S., PITAEVSKII, L., AND STRINGARI, S. Theory of Bose-Einstein condensation in trapped gases. *Reviews of Modern Physics* 71, 3 (1999), 463–512.
- [12] DAVIS, K. B., MEWES, M. O., ANDREWS, M. R., VAN DRUTEN, N. J., DURFEE, D. S., KURN, D. M., AND KETTERLE, W. Bose-Einstein Condensation in a Gas of Sodium Atoms. *Phys. Rev. Lett.* 75 (Nov 1995), 3969–3973.

- [13] DEKORSY, T., LEISCHING, P., WASCHKE, C., KÖHLER, K., LEO, K., ROSKOS, H. G., AND KURZ, H. Terahertz Bloch oscillations in semiconductor superlattices. *Semicond. Sci. Technol.* 9 (1994).
- [14] DEMTRÖDER, W. *Experimentelle Methoden der Atom und Molekülphysik*. 2009.
- [15] DONG, S., HAIST, T., OSTEN, W., RUPPEL, T., AND SAWODNY, O. Response analysis of holography-based modal wavefront sensor. *Appl. Opt.* 51 (2012), 1318–1327.
- [16] DUAN, L., CIRAC, J. I., AND ZOLLER, P. Three-dimensional theory for interaction between atomic ensembles and free-space light. *Phys. Rev. A* 66, 023818 (2002).
- [17] EARNSHAW, S. On the nature of the molecular forces which regulate the constitution of the luminiferous ether. *S. Trans. Camb. Phil. Soc.* 7 (1842), 97–112.
- [18] EINSTEIN, A. Quantentheorie des einatomigen idealen Gases. *Leiden University Einstein archive* (1924).
- [19] EINSTEIN, A. Quantentheorie des einatomigen idealen Gases - Zweite Abhandlung. *Sitzungsberichte der preussischen Akademie der Wissenschaften* (1925), 3–10.
- [20] EINSTEIN, A., PODOLSKY, B., AND ROSEN, N. Can Quantum-Mechanical Description of Physical Reality Be Considered Complete? *Phys. Rev.* 47 (May 1935), 777–780.
- [21] EKERT, A. K. Quantum Cryptography Based on Bell’s Theorem. *Phys. Rev. Lett.* 67, 6 (1991).
- [22] FISHER, M., WEICHMAN, P., GRINSTEIN, G., AND FISHER, D. Boson localization and the superfluid-insulator transition. *Physical Review B* 40, 1 (1989).
- [23] GADWAY, B., PERTOT, D., AND REIMANN, R. Analysis of Kapitza-Dirac diffraction patterns beyond the Raman-Nath regime. *arXiv:0907.3507 140401*, 2002 (2009).
- [24] GERBIER, F., WIDERA, A., FÖLLING, S., MANDEL, O., GERICKE, T., AND BLOCH, I. Phase Coherence of an Atomic Mott Insulator. *Physical Review Letters* 95, 5 (July 2005), 050404.
- [25] GIUSTINA, M., MECH, A., RAMELOW, S., WITTMANN, B., KOFLER, J., BEYER, J., LITA, A., CALKINS, B., GERRITS, T., NAM, S. W., URSIN, R., AND ZEILINGER, A. Bell violation using entangled photons without the fair-sampling assumption. *Nature Letter* 497 (2013), 227–230.
- [26] GREINER, M. Magnetischer Transfer von Atomen Ein Weg zur einfachen Bose-Einstein-Kondensation. *Master thesis, Physikalisches Institut Heidelberg*, April (2000).

- [27] GREINER, M. Ultracold quantum gases in three-dimensional optical lattice potentials. *PhD Thesis* (2003).
- [28] GRIMM, R., WEIDEMÜLLER, M., AND OVCHINNIKOV, Y. Optical dipole traps for neutral atoms. *arxiv:physics/9902072v1* (1999).
- [29] GROVER, L. K. A fast quantum mechanical algorithm for database search. In *Proceedings of the twenty-eighth annual ACM symposium on Theory of computing* (New York, NY, USA, 1996), STOC '96, ACM, pp. 212–219.
- [30] GUSTAVSSON, M., HALLER, E., AND MARK, M. Control of interaction-induced dephasing of Bloch oscillations. *Physical review . . .* (2008), 1–5.
- [31] HADZIBABIC, Z., AND DALIBARD, J. Two-dimensional Bose fluids: An atomic physics perspective. *Rivista del Nuovo Cimento* 34 (2011), 389–434.
- [32] HADZIBABIC, Z., AND KRÜGER, P. The trapped two-dimensional Bose gas: from Bose–Einstein condensation to Berezinskii–Kosterlitz–Thouless physics. *New Journal of Physics* 10, 045006 (2008).
- [33] HALLER, E., HART, R., MARK, M. J., DANZL, J. G., REICHSÖLLNER, L., AND NÄGERL, H.-C. Inducing Transport in a Dissipation-Free Lattice with Super Bloch Oscillations. *Physical Review Letters* 104, 20 (May 2010), 1–4.
- [34] HANNA, T. M., TIESINGA, E., AND JULIENNE, P. S. Creation and manipulation of Feshbach resonances with radiofrequency radiation. *New Journal of Physics* 12, 083031 (2010).
- [35] HOFFMANN, A. Bosonen im optischen Gitter. *PhD Thesis*, April (2007).
- [36] HOLZMANN, M., BAYM, G., BLAIZOT, J., AND LALOE, F. Superfluid transition of homogeneous and trapped two-dimensional Bose gases. *2007Proc. Natl Acad. Sci. USA*, 1476.
- [37] HONEYWELL. Set/Reset Function For Magnetic Sensors. *AN213, Application Note*.
- [38] HUCKANS, J., SPIELMAN, I., AND TOLRA, B. Quantum and Classical Dynamics of a BEC in a Large-Period Optical Lattice. *arXiv:0901.1386* (2009), 1–7.
- [39] HUNKLINGER, S. *Festkörperphysik*. Oldenbourg Wissenschaftsverlag, 2007.
- [40] JACKSON, J. D. *Klassische Elektrodynamik*. 2006.
- [41] JAUREGUI, R., POLI, N., ROATI, G., AND MONDUGNO, G. Anharmonic parametric excitation in optical lattices. *Phys. Rev. A* 64, 33403 (2001).
- [42] KAPITZA, P. L., AND DIRAC, P. A. M. The reflection of electrons from standing light waves. *Proc. Cambridge Phil. Soc* 29, 297 (1933).

- [43] KAUFMAN, A., ANDERSON, R., HANNA, T., TIESINGA, E., JULIENNE, P., AND HALL, D. Radio-frequency dressing of multiple Feshbach resonances. *Physical Review A* 80, 5 (Nov. 2009), 050701.
- [44] KETTERLE, W., DAVIS, K. B., JOFFE, M. A., MARTIN, A., AND PRITCHARD, D. E. Hight Densities of Cold Atoms in a Dark Spontaneous-Force Optical Trap. *Phys. Rev. Lett.* 70, 15 (1993).
- [45] KIVELSON, S. A., ROKHSAR, D. S., AND SETHNAT, J. P. Topology of the resonating valence bond state: Solitons and high-TC superconductivity. *Physical Review B* 35, 16 (1987), 8865–8868.
- [46] KOGUT, J. An introduction to lattice gauge theory and spin systems. *Reviews of Modern Physics*, 4 (1979).
- [47] KRAEMER, T., HERBIG, J., MARK, M., WEBER, T., CHIN, C., NÄGERL, H., AND GRIMM, R. Optimized production of a Cesium Bose-Einstein condensate. *Appl. Phys. B* 79 (2004), 1013–1019.
- [48] LAUGHLIN, R. Anomalous quantum Hall effect: an incompressible quantum fluid with fractionally charged excitations. *Physical Review Letters* 50, 6 (1983), 1395–1398.
- [49] LUNDBLAD, N., OBRECHT, J., SPIELMAN, I. B., AND PORTO, J. V. Optical Lattice-Based Addressing and Control of Long-Lived Neutral Atom Qubits. *Nature Physics* 5 (2009), 575–580.
- [50] LUTZ, C. Design and Implementation of a Magnetic Transfer System for Bose-Einstein Condensation. *Projektpraktikum, Physikalisches Institut Heidelberg* (2010).
- [51] LUTZ, C. Quantum Memory in a Closed Blue Detuned Dipole Trap. *Diplomarbeit, Physikalisches Institut Heidelberg*, June (2010).
- [52] MAJORANA, E. Atomi Orientati in Campo Magnetico Variabile. *Nuovo Cimento* 9 (1933), 43–50.
- [53] MANDEL, T. Towards Dipole Traps for Suppression of Dephasing in the Collective State in Quantum Memories. *Diplomarbeit, Physikalisches Institut Heidelberg*, April (2009).
- [54] MEINERT, F., MARK, M., AND KIRILOV, E. Interaction-induced quantum phase revivals in 1D atomic Bloch oscillations. *arXiv preprint arXiv: ...* (2013), 1–5.
- [55] M.H. ANDERSON, J. E. M. M. C. W., AND CORNELL, E. Observation of Bose-Einstein Condensation in a Dilute Atomic Vapor. *Science* 229, 5221 (1995), 198–201.
- [56] MORSCH, O., AND OBERTHALER, M. Dynamics of Bose-Einstein condensates in optical lattices. *Reviews of Modern Physics* 78, 1 (Feb. 2006), 179–215.

- [57] NASCIMBÈNE, S., CHEN, Y.-A., ATALA, M., AIDELSBURGER, M., TROTZKY, S., PAREDES, B., AND BLOCH, I. Experimental Realization of Plaquette Resonating Valence-Bond States with Ultracold Atoms in Optical Superlattices. *Physical Review Letters* 108, 20 (May 2012), 205301.
- [58] NGUYEN, H. Atomic Ensembles in a Hollow Beam Dipole Trap. *Master thesis, Physikalisches Institut Heidelberg* (2009).
- [59] NIELSEN, M. A., AND CHUANG, I. L. *Quantum Computation and Quantum Information*. 2000.
- [60] OCKELOEN, C., AND TAUSCHINSKY, A. Improved detection of small atom numbers through image processing. *arxiv:1007.2136* (2010), 1–4.
- [61] PAREDES, B., AND BLOCH, I. Minimum instances of topological matter in an optical plaquette. *Physical Review A* 77, 2 (Feb. 2008), 023603.
- [62] PAULING, L. Nature of the chemical bond. Application of results obtained from the quantum mechanics and from a theory of paramagnetic susceptibility to the structure of molecules. *Journal of the American Chemical Society* 455, 1927 (1931).
- [63] POLI, N., WANG, F.-Y., TARALLO, M. G., ALBERTI, A., PREVEDELLI, M., AND TINO, G. M. Precision Measurement of Gravity with Cold Atoms in an Optical Lattice and Comparison with a Classical Gravimeter. *Physical Review Letters* 106, 3 (Jan. 2011), 038501.
- [64] RAUSSENDORF, R., BROWNE, D. E., AND BRIEGEL, H. J. Measurement-based quantum computation on cluster states. *arXiv:quant-ph/0301052* (2008).
- [65] RAYMER, M., WALMSLEY, I., MOSTOWSKI, J., AND SOBOLEWSKA, B. Quantum theory of spatial and temporal coherence properties of stimulated Raman scattering. *Physical Review A* 32, 1 (1985), 332–344.
- [66] REY, A. M. Ultracold bosonic atoms in optical lattices. *PhD Thesis* (2004).
- [67] SHERSON, J. F., WEITENBERG, C., ENDRES, M., CHENEAU, M., BLOCH, I., AND KUHR, S. Single-atom-resolved fluorescence imaging of an atomic Mott insulator. *Nature* 467 (2010), 67–72.
- [68] SHOR, P. W. Polynomial-Time Algorithms for Prime Factorization and Discrete Logarithms on a Quantum Computer. *SIAM J. Comput.* 26, 5 (Oct. 1997), 1484–1509.
- [69] STECK, D. Rubidium 87 D line data. <http://www.steck.us/alkalidata/rubidium87numbers.pdf> (2001).
- [70] STRASSEL, T. Quantum Memory with Atomic Ensembles of Rubidium and Single Photons for Long Distance Quantum Communication. *PhD Thesis, Physikalisches Institut Heidelberg* (2008).

- [71] SZCZEPKOWSKI, J., GARTMAN, R., WITKOWSKI, M., TRACEWSKI, L., ZAWADA, M., AND GAWLIK, W. Analysis and calibration of absorptive images of Bose-Einstein condensate at nonzero temperatures. *The Review of scientific instruments* 80, 5 (May 2009), 053103.
- [72] TING, W.-C., HAN, D.-J., AND WU, S.-T. Manipulation of coherent atom waves using accelerated two-dimensional optical lattices. *New Journal of Physics* 12, 8 (Aug. 2010), 083059.
- [73] TROMPETER, H., KROLIKOWSKI, W., NESHEV, D., DESYATNIKOV, A., SUKHORUKOV, A., KIVSHAR, Y., PERTSCH, T., PESCHEL, U., AND LEDERER, F. Bloch Oscillations and Zener Tunneling in Two-Dimensional Photonic Lattices. *Physical Review Letters* 96, 5 (Feb. 2006), 10–13.
- [74] TSCHERBUL, T., CALARCO, T., AND LESANOVSKY, I. RF-field-induced Feshbach resonances. *Physical Review A* (2010), 1–10.
- [75] TSUI, D., STORMER, H., AND GOSSARD, A. Two-dimensional magnetotransport in the extreme quantum limit. *Physical Review Letters* 48, 22 (1982), 1559–1562.
- [76] VERNAM, G. Vernam cipher. *U.S. Patent 1,310,719* (1919).
- [77] WEBER, T., HERBIG, J., MARK, M., NÄGERL, H.-C., AND GRIMM, R. Bose-Einstein Condensation of Cesium. *Science* 229, 5604 (2002), 232–235.
- [78] XU, X. Quantum Information Processing with Atomic Ensembles and Ultracold Quantum Gases in 2D optical Lattices (in preparation). *PhD Thesis, Universität Heidelberg* (2014).
- [79] YANG, F., MANDEL, T., LUTZ, C., YUAN, Z.-S., AND PAN, J.-W. Transverse mode revival of a light-compensated quantum memory. *Phys. Rev. A* 83 (Jun 2011), 063420.
- [80] ZENER, C. A Theory of the Electrical Breakdown of Solid Dielectrics. *Proc. R. Soc. Lond.* 145 (1934), 523.
- [81] ZHANG, J., AND LIU, W. Directed coherent transport due to the Bloch oscillation in two dimensions. *Physical Review A* 82, 2 (Aug. 2010), 2–5.
- [82] ZHAO, B. Robust and Efficient Quantum Repeater with Atomic Ensembles and Linear Optics. *PhD Thesis, Universität Heidelberg* (2008).
- [83] ZHAO, B., CHEN, Y.-A., BAO, X.-H., STRASSEL, T., CHUU, C.-S., JIN, X.-M., YUAN, Z.-S., CHEN, S., AND PAN, J.-W. A millisecond quantum memory for scalable quantum networks. *Nat Phys* 5, 2 (2009), 95–99.
- [84] ZHAO, R., DUDIN, Y. O., JENKINS, S. D., CAMPBELL, C. J., MATSUKEVICH, D. N., KENNEDY, T. A. B., AND KUZMICH, A. Long-lived quantum memory. *Nat Phys* 5 (2009/02).

- [85] ZWERGER, W. Mott-Hubbard transition of cold atoms in optical lattices. *Journal of Optics B: Quantum and Semiclassical Optics* 5, 2 (2003).